UNIVERSIDAD DE SALAMANCA

DOCTORAL THESIS

Fabrication and characterization of Quantum Materials: Graphene heterostructures and Topological Insulators

---

Author:
Vito CLERICÒ

Supervisor:
Prof. Enrique DIEZ

UNIVERSIDAD DE SALAMANCA

Abstract

Fabrication and characterization of Quantum Materials: Graphene heterostructures and Topological Insulators

by Vito CLERICÒ

Starting from a detailed description of the Clean Room facilities, installed during this thesis work, we report the fabrication processes based on graphene and other 2D materials in detail. In hBN-encapsulated graphene the Quantum Hall Effect (QHE) at room temperature and high magnetic field was observed. We found different features in the QHE respect a previous work on lower mobility graphene on silicon oxide (Novoselov et al. Science 315 1379 2007). A detalied study of transport properties in graphene nanoconstrictions is also reported. In particular in encapsulated graphene we introduced a new cryo-etching method to obtain low roughness edges nanocostrictions, in which quantized conductance was observed. In the last part of the thesis we report transport measurements on InAs/GaSb double quantum wells with different bandgap configurations (inverted, normal or critical).

Acknowledgements

Tengo que agradecer muchas personas por todos estos años durante los que he realizado mi doctorado (y trabajo como técnico de sala blanca :-P) en Salamanca. Estos agradecimientos van a ser en español (a parte los agradecimientos para no hablantes de español), así que pido disculpa por eventuales errores.

Sin duda la primera persona a quien dar la gracias es mi supervisor de tesis, Enrique. Sin ti probablemente nunca hubiera empezado el doctorado, ya que tu apoyo y enseñanzas han sido fundamentales para revitalizar mi pasión por la "Ciencia" e introducirme en este fantástico mundo de los materiales 2D. Tu confianza en mi fue total, aunque no fue nada fácil especialmente en los años en que había que "arrancar" todo de cero, nada era simple, a nadie le interesaba la sala blanca, ni en general lo que hacía en el "idi" . Tu estuviste siempre presente o si no podías físicamente, te hiciste siempre sentir presente. Cuando pienso en todo lo que se ha hecho durante estos años bajo tu "ala protectora" , me parece realmente increíble. Un agradecimiento grande también a Yahya, siempre disponible para solucionar problemas en laboratorio. Contigo empecé mi actividad investigadora en Salamanca con las medidas en el TDS cuando todavía no había sala. Gracias a Mario, que en realidad es la persona que conozco desde mas tiempo. Sin ti, yo no estaría trabajado aquí en Salamanca y no hubiera podido vivir esta bonita experiencia. Gracias a Francisco y su grupo de investigación por todo el suporte teórico y por la gran experiencia investigadora, que ha sido fundamental para los artículos publicados en grafeno. Una de las primeras personas que ha apreciado mis calidades como técnico de sala blanca (con el imaging de sem) ha sido Mercedes. Gracias también por dejarme utilizar el Raman, que ha sido fundamental para esta tesis. Gracias a Enrique Velazquez por su amabilidad y claridad en decir las cosas por como realmente son. Gracias a José María

y Pilar por la gran consideración que me han hecho siempre sentir, siempre habéis sido una referencia de la Facultad de Física para mi. Gracias a Vittorio Bellani para los buenos momentos vividos (bajo tu supervisión) durante las interminables horas de medidas en las estancias de Nijmegen. Gracias a Susana y Loli para la confianza que habéis puesto en mi como técnico. Gracias también a Ignacio (Indy) por la consideración de mi trabajo y por intentar de organizar mejor el trabajo de los "técnicos" en este último año. Thank you also to Stephen, it was really a great pleasure to work (even if hard but never heavy :-)) under your supervision during my stay in Nijmegen and also to Prof. Otsuji Sensei and Prof. Yakov for their availabilty during my PhD stays in Japan and Brazil.

Y ahora vamos con los compañeros de trabajo...aunque hay que decir que muchos realmente se han convertido en grandes amigos en estos años. También aquí, no tengo duda sobre quien empezar. Mi gran compañero y hermano menor Juanan. Nunca olvidaré los momentos duros vividos juntos, cuando nada funcionaba y era muy fácil perder la paciencia. Cuando pienso a las horas echadas para acabar un dispositivo, una medida o para arreglar un equipo, me pregunto si fue humano. A día de hoy creo que si lo superamos es porque lo hicimos juntos. Pero no solo de estos momentos de los que quiero acordarme. Quiero recordar los momentos bonitos, que fueron muchísimos, de las risas y bromas que he vivido contigo también fuera del trabajo. Fuiste un gran amigo y el mejor compañero de trabajo posible. Mi esperanza (aunque difícil) para el futuro es que podamos volver a serlo. Otro gran compañero es Adrián, siempre extremamente disponible para cualquier ayuda, poniéndole siempre muchísima pasión en todo lo que hace (dentro y fuera del trabajo). Gracias por tu gran actitud. Gracias a David que has sido como un hermano mayor que siempre ha intentado de iluminar el camino que a veces se ha hecho oscuro y tortuoso. Manuel porque has sido un buen compañero y porque me has hecho recordar cual son las verdaderas cosas

importante y prioridades en la vida. Daniel, que, aunque muy joven, has siempre demostrado una gran madurez y amor en tu trabajo (aunque eres demasiado modesto!), Yoann por tu actitud siempre positiva en el trabajo, también cuando las cosas no iban bien o eran muy aburridas. Quiero también agradecer los últimos "llegados" . Juan porque se ve que vienes de Zamora (:-P) y que vas a ser un gran compañero, Jorge por tu gran y "contagiosa" :-) pasión para tu investigación. Un gracias también a mis primeros compañeros aquí en Salamanca. Cayetano para introducirme en el ambiente salmantino y Sergio para ayudarme muchísimo en todos los ámbitos (laboral y extra-laboral). Por terminar este grupo, las personas que considero el alma del idi, Pedro, Mamadou, Aurora, Juanma, Vanessa y Teresa. Este edificio hubiera sido mucho mas triste sin vosotros.

Un gracias también a mis amigos y familiares que han estado a mi lado durante estos años. La primera persona es seguramente la persona más especial que he conocido en Salamanca, mi mujer Yan. Tu apoyo fue inmenso en estos años, especialmente en los momentos mas duros, cuando no había nada bonito que pudiera darme la motivación de ir adelante. Fuiste (y eres) la razón de mi vida. 夏艳，我的老婆, 我爱你。.

Gracias a María, mi mejor amiga aquí en Salamanca, siempre capaz de entenderme con una sola mirada (y no solo para bailar). Gracias a Pilar, Vitor y Dalia por los momentos bonitos pasados juntos. Es raro agradecer un lugar...pero hay un lugar en Salamanca, la Nómada, que para mi ha siempre tenido un significado: desconnexión total para pasarlo pipa (cit.). Allí he empezado a bailar tango, que se ha convertido en adicción y me ha permitido conocer personas fantásticas como Martín, Lola, Bea, Ana, Borja, Andreas, Vanessa, Judith, Mar y todos los tangueros de Salamanca o los que han pasado por Salamanca. Un Gracias a Alberto, para las "quedada" juntos y para ser siempre muy amable en ayudarme con el mundo salmantino. Gracias también a mi querida profesora de chino, Potseng. Gracias a mis

primeras compañeras de piso (Cristina y Margot) y Geo, Alice para los buenos momentos pasados juntos.

In questi anni mi è mancata molto mia sorella Santina, che insieme a suo marito Daniele mi hanno regalato tanta felicità con il recente arrivo del mio nipotino Alessandro. Infine, però sicuramente non per importanza, i miei genitori Giuseppe e Rosetta, che mi hanno sempre supportato nelle mie scelte e ai quali questa tesi è dedicata. Gli ultimi tempi mi hanno fatto capire ancora di più il forte sentimento che mi lega a voi, che può essere riassunto in due sole parole: incommensurabile Amore.

Contents

Acknowledgements **v**

1 Introduction: Graphene and Topological Insulators **1**

2 Equipment and experimental setup measurements **5**

2.1 Clean Room facilities 5

2.1.1 FE-SEM and Raith nanolithography system 9

SEM-resolution 10

FE-SEM 10

2.1.2 Raith (Elphy Plus) nanolithography system 14

2.1.3 Working principles 14

2.1.4 Raith (Elphy Plus) nanolithography controller 14

2.1.5 ICP-RIE 16

Principles 16

PlasmaPro 100 Estrelas system 18

2.1.6 Mask aligner MJB4 20

Working principle of the optical lithography 20

MJB4 mask aligner 20

2.1.7 Fume Cupboards for lithography and for chemical processes 21

2.1.8 E-beam evaporator 22

Working principles 22

Tecnovac E-beam evaporator with Telemark e-beam gun emitter 22

2.1.9 RTP As-One100 24
2.1.10 DM8000 Optical Microscope Leica, DektakXT Bruker Profilometer and Harrick Plasma cleaner 26
Leica DM8000 Optical Microscope 27
DektakXT Bruker Profilometer 27
Harrick Plasma cleaner 28
2.2 2D-Transfer setup 28
2.3 Equipment for preliminary characterization: MicroRaman, Probe station and Time Domain Spectroscopy (TDS) 30
2.3.1 LabRAM HR Evolution MicroRaman 30
Principles 31
MicroRaman 32
2.3.2 Probe stations 4-probes:Cascade Summit 1100B Station and TPT BH10 Wire Bonder 33
2.4 Facilities for Magnetotransport measurements 34
Pulse tube technique 34
2.4.1 AC-V12 (3 K) cryostat 35
2.4.2 Triton (50 mK) cryostat and superconducting magnet . 36
2.4.3 High Field Magnet Laboratory (HFML) 38
2.4.4 Other optical characterization: Terahertz - Time Domain Spectroscopy (THz-TDS) 39
2.5 Setup Mesurements: Lock-in Amplifier and Sourcemeter 40
2.5.1 Principles of the lock in technique 40
Setup 42

3 Devices: Fabrication and preliminary characterization 45
3.1 Exfoliated graphene-based devices 46

3.1.1 Graphene Hall Bars on SiO_2 (with and without HMDS treatment) and Graphene nanoconstrictions on HMDS 47
Graphene Nanoconstrictions with HMDS 50
3.1.2 Hall Bar with graphene on hBN 51
3.1.3 Hall Bar with hBN-encapsulated graphene (with option of the graphite backgate) and Nanoconstrictions with encapsulated graphene 56
Nanoconstrictions fabricated by cryo-ething in encapsulated graphene 64
3.1.4 FETs detectors based on encapsulated graphene 66
3.2 Epitaxial graphene and CVD graphene devices 67
3.2.1 Hall bar with epitaxial graphene with the option of gate voltage 68
Definition of gate voltage on epitaxial graphene 70
3.2.2 CVD graphene devices 72
3.3 $MoSe_2$ and $MoTe_2$ devices 73
3.3.1 $MoSe_2$ devices 74
3.3.2 $MoTe_2$ devices 75

4 Quantum Hall Effect at high temperatures 79
4.1 Quantum Hall Effect up room temperature in graphene 79
High Temperature and density carrier dependence . . 80
4.1.1 Mobility and random strain fluctuations 83
4.1.2 QHE at room temperature 85
4.1.3 Activation gap in encapsulated graphene 88
4.1.4 Zero-Landau level 90
4.2 Fractional Quantum Hall effect in encapsulated graphene . . . 91
4.3 Conclusion 93

5 Ballistic Transport in graphene Nanoconstrictions 95

5.1 Tight-Binding model 97

5.2 Transport measurements on Graphene Nanoconstrictions (GNCs) with Hexamethyldisilazane (HMDS) treatment 98

5.3 Transport measurements on Graphene Nanoconstrictions (GNCs) fabricated by cryo-etching in encapsulated graphene 103

5.3.1 Graphene constriction defined with Orion Nanofab Helium Ion Microscope 111

5.4 Conclusion 113

6 Magnetotransport Measurement on InAs/GaSb double quantum wells (DQWs) 115

6.1 8-Band $\mathbf{K} \cdot \mathrm{P}$ Calculation of InAs/GaSb Double Quantum Wells 117

6.2 Anomalously large resistance at the charge neutrality point in a zero-gap InAs/GaSb bilayer 120

6.2.1 Temperature Dependence 122

6.2.2 Perpendicular and parallel magnetic fields dependence 124

Perpendicular Magnetic Field 124

Parallel magnetic Field 125

Phenomenological method 126

6.3 Critical sample 128

6.4 Inverted sample (d=13nm) 130

6.5 Discussion 133

7 Conclusion and future perspectives 137

A Resumen 141

B Conclusiones y Perspectivas 143

C List of publications 147

D Conference Proceedings and Oral Contribution **149**

E Funding received **151**

Bibliography **153**

Ai miei genitori Giuseppe e Rosetta, per il loro incommensurabile Amore....

Chapter 1

Introduction: Graphene and Topological Insulators

In the last ten years two Nobel prices in Physics were given to Andrey Geim and Kostantin Novoselov in 2010 (Graphene, the perfect atomic lattice) and to David J. Thouless, F. Duncan M. Haldane and J. Michael Kosterlitz in 2016 (for theoretical discoveries of topological phase transitions and topological phases of matter). Thanks to their extraordinary properties in the quantum physics world, graphene and topological insulators (TIs) have shown new exotic phases of the matter and they represent plausible revolutionary candidates for future applications in material science and electronics.

One major reason why graphene and TI attracted a large interest of the scientific community lies in their mathematical description as "Dirac materials"[1][2], since they can be described by Dirac equation rather than non-relativistic Schrödinger equation. Dirac equation typically describes the behavior of particles with a velocity closed to the speed of light, so it is typically used in the field of the high energy physics rather than the matter physics world. As well as massless neutrinos and their antiparticles (antineutrinos), the relativistic electrons possess their antiparticles ("holes"), that are positively charged particles (absence of electrons). Graphene and TI represent electrically tunable system in which the charge density can be set to zero. The band structure close to the Fermi level of these materials, is characterized

by the well-known linear energy-momentum relation of relativistic massless particles, hence the name of Dirac cones [3]. Electronic excitations in the vicinity of the Fermi level of a number of advanced materials resemble massless Dirac fermions. From the standpoint of applications, Dirac materials are envisioned to be of outstanding importance due to their universal behavior and the robustness of their properties [1].

Novel quantum phenomena and many possible applications have been found in graphene (room temperature quantum hall effect[4] and quantum spin hall effect[5], quantized conductance in graphene nanoconstrictions [6], use for field effect transistors (FET) [7] or in spintronics [8] and recently superconductivity [9]) as well in TI (quantum spin hall effect [10], quantum anomalous hall effect).

From an application point of view, replacing the silicon in electronic devices with graphene, other 2D materials and/or topological insulator materials are expected to be revolutionary for electronics, improving the devices performances in an incommensurable way. In the last years the Moore's law [11], that predicted the improvement of the devices performances according their miniaturization, have saturated due to physical effects, increasing leakage and overheating at the nanoscale related with the miniaturization itself.

In this panorama, graphene and TIs could be the new materials to overcome this limitation, thanks to the high electron transmission and coherent transport for short distance typical of these systems in which linearly dispersing bands prevent any possible scattering.

This thesis is structured in the following way:

- In Chapter 2 we report all the facilities and measurements setup. Among all, it is necessary to point out the Clean room facilities that have been started and completed during this thesis work. All the results on graphene and other 2D materials described in this thesis, come from devices that have been fabricated for the first time in the Clean Room of Salamanca.

- One of the most important goal of this thesis was the fabrication of Van de Walls heterostructures, in particular of graphene and the realization of graphene heterostructures devices. In Chapter 3 all the fabrication methods for the 2D materials devices are fully described, from the exfoliation and transfer methods of 2D materials (to stack them), to the optical and electron lithography, evaporation, etching techniques.

- In Chapter 4 we present a study of Quantum Hall Effect (QHE) in graphene at room temperature. QHE is a first example of topological transport, since one-dimensional conduction occurs without any scattering at the edge of the sample. Graphene is nowadays the unique material in which QHE appears at room temperature and high magnetic field [4], but the physical mechanisms are not still fully understood.

- In Chapter 5 we report the study of graphene nanoconstrictions with hexamethylsilazane (HMDS) treatment and with encapsulation in Hexagonal Boron Nitride (hBN). Nanoconstrictions in graphene as well as quantum point contact [12][13] are systems in which ballistic behaviour can be easily reached thanks to the high mobility. Through the conversion of a 2D system into a 1D one [14][15], they represent systems in which coherent transport can be achieved for the quasi-lack of scattering. In the encapsulated graphene constrictions we found a ballistic transport close to the ideal one and conductance quantization thanks to a cryoetching method applied for the first time to graphene devices.

- At the beginning of this thesis, one of the intriguing aim consisted in comparing the topological state of InAs/GaSb quantum wells [16] with graphene nanostructures[17]. This initial purpose was affected by the lack of InAs/GaSb samples, since we cannot grow this material in Salamanca. In this Chapter 6 measurements on InAs/GaSb quantum wells, fabricated in Sandia National Laboratories, were carried with different

configuration (insulator, critical and inverted (topological)). The possible formation of an excitonic insulator gap in an critical InAs/GaSb quantum-well system at low temperatures has been discussed.

Chapter 2

Equipment and experimental setup measurements

In this Chapter we describe the equipment and experimental setup that have been used during this thesis work. The Clean Room (CR) has a special role in my PhD studies, since I started my activity in Salamanca as technician, heading and checking under the supervision of my thesis director the building of the CR and the installation of all the equipment. The first two years of my PhD were characterized mainly by technical work and it has partially occupied me for the rest of the years, extending the time for the conclusion of this thesis because of the double work as "PhD Student "and "Clean Room Technician "at the same time.

Here we start with the description of the Clean room facilities for the fabrication of graphene and other 2D materials devices, then the experimental setup for characterization.

2.1 Clean Room facilities

The Clean Room and the Grey area of the Nanotechnology group of the University of Salamanca are formed by three different rooms. The schematic view is shown in Figure 2.1(a), where the limited pink area is the classified Clean room area, meanwhile the green lines delimit the grey area.

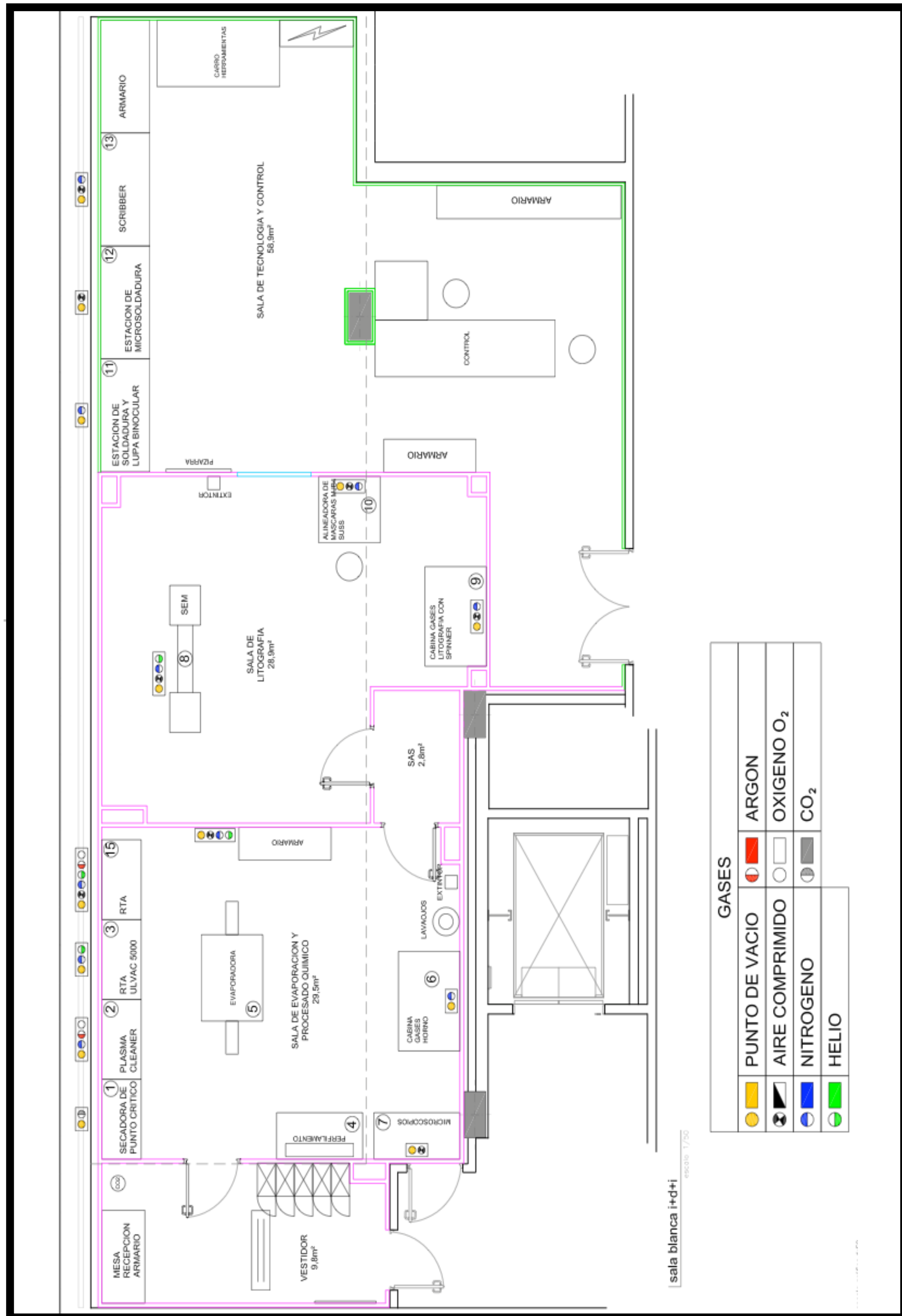

FIGURE 2.1: (a) Clean room drawing. In pink the Clean room area, the green line delimits the technical area (grey area).

ISO CLASS	$\geq 0.1\mu m$	$\geq 0.2\mu m$	$\geq 0.3\mu m$	$\geq 0.5\mu m$	$\geq 1\mu m$	$\geq 5\mu m$
ISO1	10	2	-	-	-	-
ISO2	100	24	10	4	-	-
ISO3	1000	237	102	35	8	-
ISO4	10000	2370	1020	352	83	-
ISO5	100000	23700	10200	3520	832	29
ISO6	1000000	237000	102000	35200	8320	293
ISO7				352000	83200	2930
ISO8				3520000	832000	29300
ISO9				35200000	8320000	293000

TABLE 2.1: ISO class conditions from class ISO 1 to class ISO 9 for maximum concentration limits (particles/m^3 of air)

The Clean Room is a special facility in which the environment (humidity, temperature, airflow, number of particles) is strictly controlled according a standard classification and in particular it depends on the cleanliness of the air inside them. Thus, air and water (18.2 MΩ/cm) are filtered to reduce the number of particles and to avoid contamination. In addition, pressure inside the clean room is set to be positive with respect to the outside, so particles are not allowed to penetrate. In our Clean Room an unidirectional, air flow system directs filtered air downward in a constant stream through the use of High-Efficiency Particle Air (HEPA) filters.

Cleanrooms are classified by the level of air cleanliness. The typical classification is the ISO146444-1, the classes can change from ISO1 to ISO9. ISO1 is the cleanest class, and conversely the ISO9 is the dirtiest class. A clean environment is fundamental for the fabrication of nano and micro-devices.

In the Clean room of the University of Salamanca the class is ISO6 for the "lithography room" where it is necessary a major control of the air and ISO7 for the "evaporation "room. The maximum concentration limits (particles/m^3 of air) of ISO6 and ISO7 for different size of particles are reported in table 2.1.

The initial building of the Clean Room started in 2014 and the installation of all the equipment was concluded in July 2016, with "latecomers"ICP-RIE

and microRaman, that have been fundamental for this thesis work. Two photos in Figure 2.2 show the"evaporator room"(a) and the "lithography room"(b) before the installation of the equipment.

FIGURE 2.2: (a) Photo of the "Evaporation"room without equipment in September 2014 (b) Photo of the "Lithography"room in the same period.

The light in the "lithography room"is filtered for the use of low-visible-wavelenght sensitive light resists.

Figure 2.3 shows the actual situation in the Clean Room, for both, the "lithography room"and the "evaporation room".

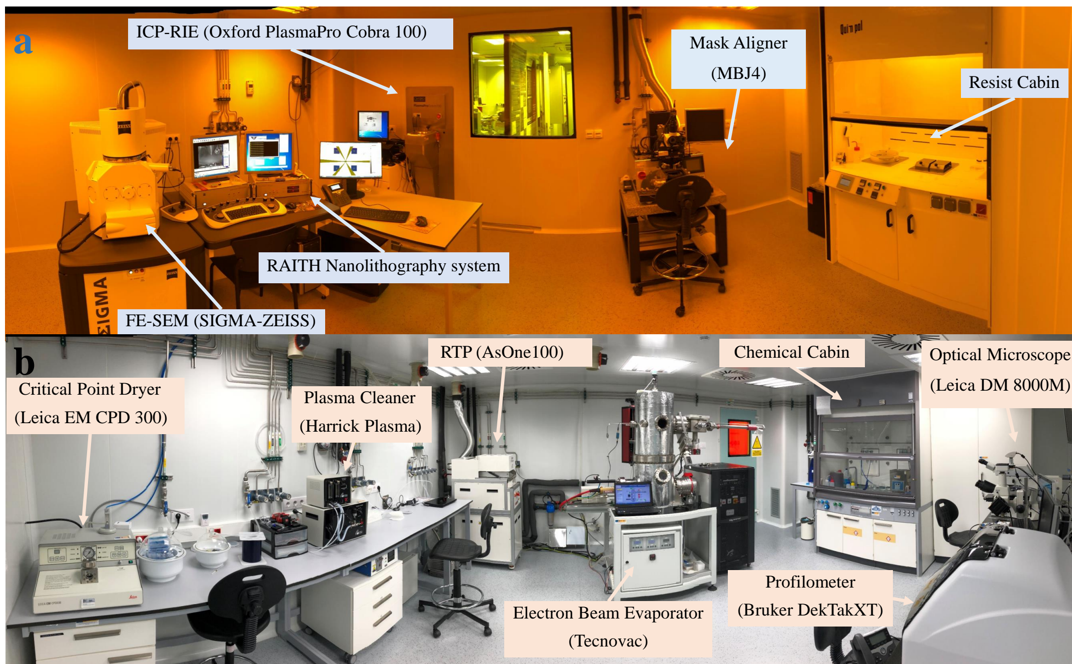

FIGURE 2.3: Clean room Facilities : (a) "lithography room"(b) "evaporation room"

The **lithography room** (from the left to the right) have:

- FE-SEM (SIGMA-ZEISS)
- Raith Nanolithography system
- ICP-RIE (Oxford PlasmaPro Cobra 100)
- Mask Aligner (MBJ4)
- Fume cupboard for lithography

The equipment (from the left to the right) in the "**evaporation room**"are formed by:

- Crytical Point Dryer (Leica EM CPD 300)
- Plasma Cleaner (Harrick Plasma)
- Rapid Thermal Annealing RTP (AsOne100)
- Electron Beam Evaporator (Tecnovac)
- Fume cupboard for chemical solutions
- Optical Microscope (Leica DM 8000M)
- Profilometer (Bruker DekTakXT)

Below are shown and detailed the equipment used during this thesis.

2.1.1 FE-SEM and Raith nanolithography system

Electron beam imaging and lithography processes were performed using a Field Emission (FE) Scanning Electron Microscope (SEM), FE-SEM SIGMA Zeiss with Gemini column and SmartSEM 5.6 software (Figure 2.3a).

SEM-resolution

Electron microscope uses very high energetic electrons as source. Since the resolution in an optical microscope is limited by diffraction and depends on the wavelenght of the light itself, thus in an electron microscope with the shorter electron wavelenght a higher resolution is allowed. The wavelenght λ is related to the momentum according the formula:

$$\lambda = \frac{h}{p} \tag{2.1}$$

where h is the Planck constant ($h = 6.626X10^{-34} J \cdot s$) and p is the momentum of the electrons. Using the relativistic equations, we can express the electron wavelenght λ as function of the accelerated voltage V [18]:

$$\lambda = \sqrt{\frac{1.5}{V(1+10^{-6}V)}} nm$$

where for a typical value of the accelerated voltage ($5kV$), a nominal resolution of 0.017 nm can be achieved.

FE-SEM

The Gemini column is the area of the FE-SEM, where electrons are emitted, accelerated, bundled, focused and deflected. It has the unique integrated beam booster technology, to keep the beam at high potential in the full length of the column, independent from the landing energy [19].

A schematic view of our FE-SEM with Gemini column is shown in Figure 2.3(b). Anode (5) and vacuum tube (6) are isolated from the column ground. The vacuum tube is necessary to separate condenser lens (7) from the vacuum space. Multiple apertures (8) are mounted in the vacuum tube. For imaging processes the standard aperture used is 30 microns, but especially for electron beam lithography different apertures (7.5, 10, 20, 30, 60 and 120

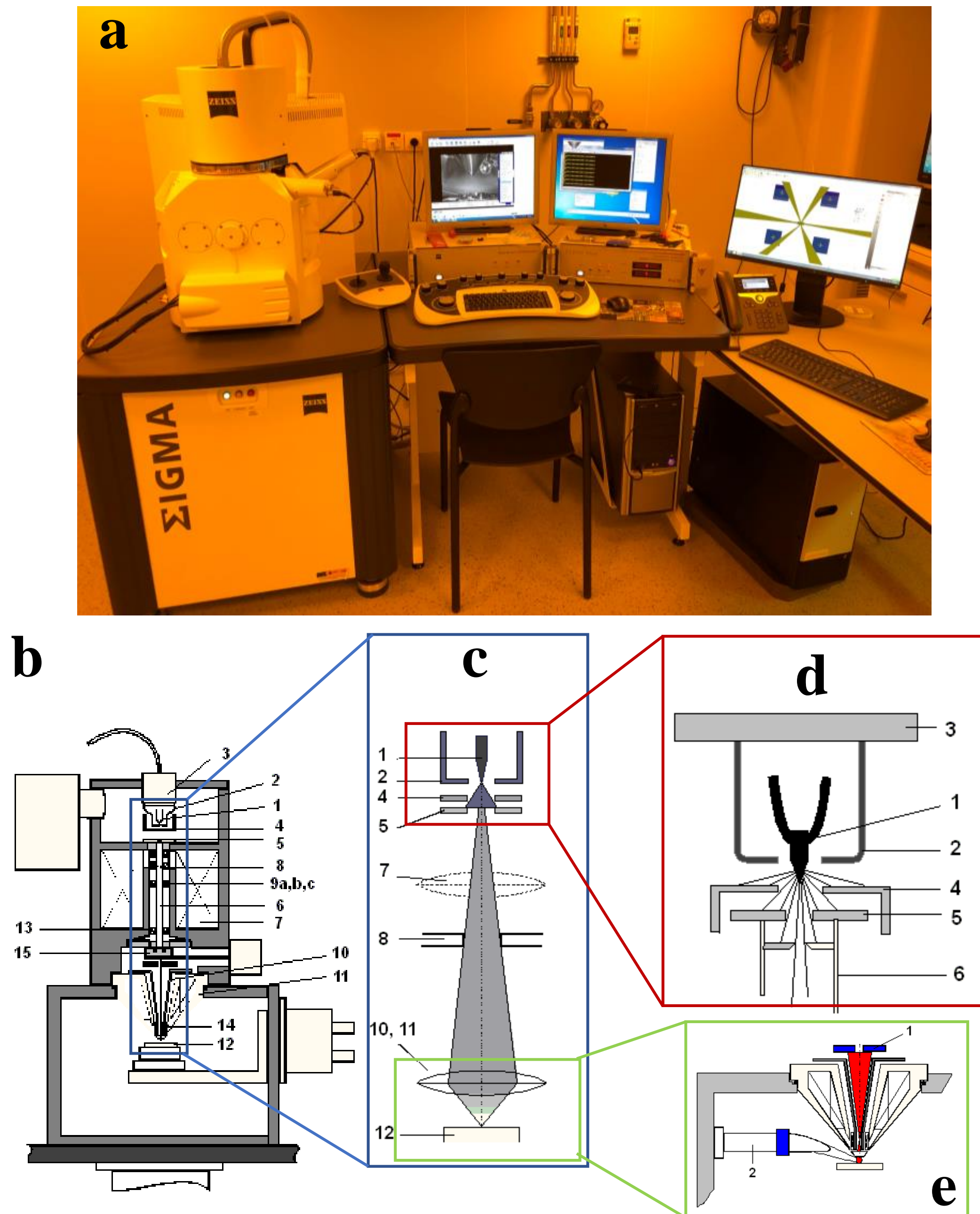

FIGURE 2.4: (a) Photo of the FE-SEM and the Raith nanolithography system. (b) Schematic views of FE-SEM, (c) electron beam path. (d) field emission gun, (e) position of InLens and SE detector respect the specimen and the column. All the schematic views are taken from the SmartSEM 5.6 software.

microns) could be electromagnetically selected through software to achieve a good compromise between resolution and exposition time. A column chamber valve (15) separates the gun from the specimen chamber. With an ion getter pump (IGP) the typical pressure values are in the range of 10^{-10} mbar for the gun area. The vacuum in the specimen chamber is guaranteed thanks to turbo pump and a typical pressure range is 10^{-6} mbar.

The electron beam path is shown in figure 2.3(c). The electrons are generated in The Schottky field emission filament (1), controlled by the suppressor electrode (2) and collected by the extractor (4). Finally the electrons are accelerated to the anode. So the electron beam passes through the borehole of anode and the condenser (7), before be collimated by the aperture.

A zoomed scheme of the field emission gun is shown in Figure2.3(d). Respect to a conventional SEM, a FE-SEM has a field emission gun that permits the use of high focused and low-energy electron beam. This characteristic comports an improved spatial resolution and the possibility to work at very low potentials (0.01–5 kV). The use of low potentials minimises the charging effect and reduces damages to electron beam sensitive samples, as graphene devices. A Schottky Field Emission cathode is made of finely etched tungsten tip which has been spot-weided on a filament (1) coming from tungsten wire. The shaft of the cathode tip has a coating of ZrO_2. When a current goes throught filament, a ZrO coating diffuses on the cathode tip and the oxygen is released, and thus the work function of the tungsten is reduced from 4.6 eV to 2.6 eV. A constant source emission is guaranteed thanks to the cathode temperature and the field applied to the cathode tip by the extractor electrode (4). The reduction of the work function and the high field present at the cathode tip, are the reason why the Schottky Filed Emission source emits also at very low temperatures.

After its generation, the electron beam interacts with the specimen giving useful information about the sample (its surface features, size and shape

of the features etc.). After the interaction with the sample the electrons in our system can be collected by two different detectors, an In-Lens detector and a Everhart-Thornley detector (SE2) (Figure 2.3(e)). Both work detecting secondary electrons. When the incident electrons come close enough to the specimen, they will partially give part of their energy to the specimen electrons. In this way part of the incident electrons will change their path and will ionize the electrons close to the surface (10 nm) in the specimen atoms. The ionized electrons that escape from the atoms are called secondary electrons. They are characterized by low energy (less than 50 eV). All electrons with energy higher than 50 eV are known as backscattered electrons (BSEs). There are three different kind of secondary electrons:

- SE1 secondary electrons: They are generated and leave the surface of the specimen directly at the same position in which the incident electron beam hit the specimen.
- SE2 secondary electrons: They are generated after multiple scattering inside the specimen and leave the sample at a certain distance from the impact point of the incident beam
- SE3 secondary electrons: They are generated by backscattered electrons colliding with the chamber walls or the lens system.

Our system is able to detect the SE1 and SE2 electrons. The In-Lens detector (1 in figure 2.3(e)) is located inside the electron column of the microscope and it collects the Secondary electrons (SE1) that are emitted from the sample surface (typically 10 nm from the top side of the surface) by initial interaction with the sample. Therefore, this detector provides surface details at low energy. Everhart-Thornley detector (SE2) is located in a lateral position (2 in figure 2.3(e)). In this detector, secondary electrons are emitted after interacting with the upper layer of the sample. This detector is designed to work at working distances between 5-12 mm.

The maximum extractor voltage is 20 kV in our system. The instrument includes 3-axis (x, y, z) fully motorized rotary stage with tilted option to rotate along z-axis from 0° to 90°. Samples of size as large as 4-inch are allowed.

2.1.2 Raith (Elphy Plus) nanolithography system

The nanolithography processes were made through Raith nanolithography system.

2.1.3 Working principles

The typical electron beam lithography is schematically shown in Figure 2.5. An electron beam incises in desired areas of the resist (sensitive to electrons). In this way the chemical bindings in the exposed area of the resist become more or less weaker (it depends on the type of resist: negative or positive). After the developing process, the weaker chemical bindings are removed and the exposed resist (depending on the tone) remains or leaves the substrate. The resist mask on the sample can be used for different purposes [20]. It can be used as mask in etching processes, to protect the covered regions and thus the areas without resist are etched (see subsection 2.1.5). Another possibility is related with the evaporation of metals, where the metals are deposited everywhere on the sample, but after the well-known lift-off process, only the metals attached on the sample remain and conversely the metal deposited on the resist is removed with the resist itself (see subsection 2.1.8).

2.1.4 Raith (Elphy Plus) nanolithography controller

Elphy Plus is a system which makes possible to produce micro and nano structures by means of electron beam writing in connection with FE-SEM. The hardware assembly is built into a 19″ rack consisting of a digital control unit and a separate thermocontrolled analog electronics box. It has a X-Y

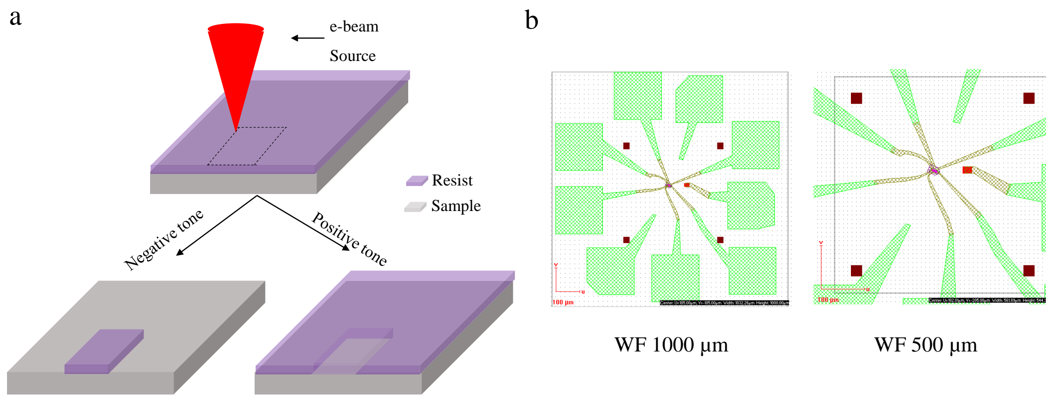

FIGURE 2.5: (a) Schematic representation of an electron beam lithography process (b) The same CAD designed with ELPHY software in which we selected two different writing field (WF): 1000 μm (left) and 500 μm (right).

beam shift inputs and a video out to a monitor (BAS out). The electronics units is completely remote controlled by PC data system via an integrated SCSI interface.

Apart of the ELPHY Plus rack, our nanolithography system presents a Beam blancked controlled by the electronic beam blancked controlled unit. The beam blancked hardware is installed on the SEM column. It consists in two parallel plates, one is grounded and the other is connected to the high voltage. When voltage is zero, the electrons are allowed to pass through a spray aperture and so they can reach the sample. Conversely when a non-zero voltage is applied, electrons are deflected and the aperture does not permit the electrons to reach the specimen. The Beam Blancker control unit is a high voltage power supply, accepting a TTL voltage from the ELPHY Plus rack.

The ELPHY Plus software includes all the features needed to expose micro and nano structures (writing fields, doses etc.) and it is integrated with a GDSII based editor. Figure 2.5(b) shows the same CAD (Hall bar) but selecting two different writing field (WF). On the left side a WF of 1000 μm, typically used for pads definition (green layer in the Figure 2.5 b) and on the right a WF of 500 μm typically used to define the contacts of the sample

(brown layer in the Figure 2.5 (b)).

2.1.5 ICP-RIE

All the dry-etching processes on our samples were carried out with the PlasmaPro 100 Estrelas system.

Principles

There are different dry-etching technique; Reactive Ion Etch (RIE), Inductively Coupled Plasma Etch (ICP Etch), Planar Etch (PE), or Deep Reactive Ion Etch (DRIE Etch). Despite the above techniques need a plasma source, the main difference lies on the configuration of the electrodes for the plasma generation. A plasma is defined as a medium of positive and negative particles. It is formed when a gas becomes ionized due to radio frequency (RF) energy, microwave radiation, electromagnetic (EM) fields, with an energy higher than the binding energy of an electron of the gas atom/molecule. This ionization energy depends on the atom/molecule; for example for our gases it changes from 11.6 eV in Cl_2 to 15.7eV in Ar. Using plasma is a way of performing high temperature chemistry at low temperatures. The variations of different parameters (i.e. gas mixture, temperature, pressure or plasma power) anisotropic or isotropic profile of the etched sample can be obtained. As we mentioned on section 2.1.3, covering the sample with a polymer (i.e. resist) or metal, can play the role of mask, previously defined by a lithographic process, where only those areas of the sample uncovered by the mask are etched and the other areas are protected by the mask, that normally is removed after etching process (see Figure 2.6(a)).

In our system, it is possible to carry out RIE or ICP-RIE processes, so we restrict the discussion on these two techniques. In a RIE process, a plasma

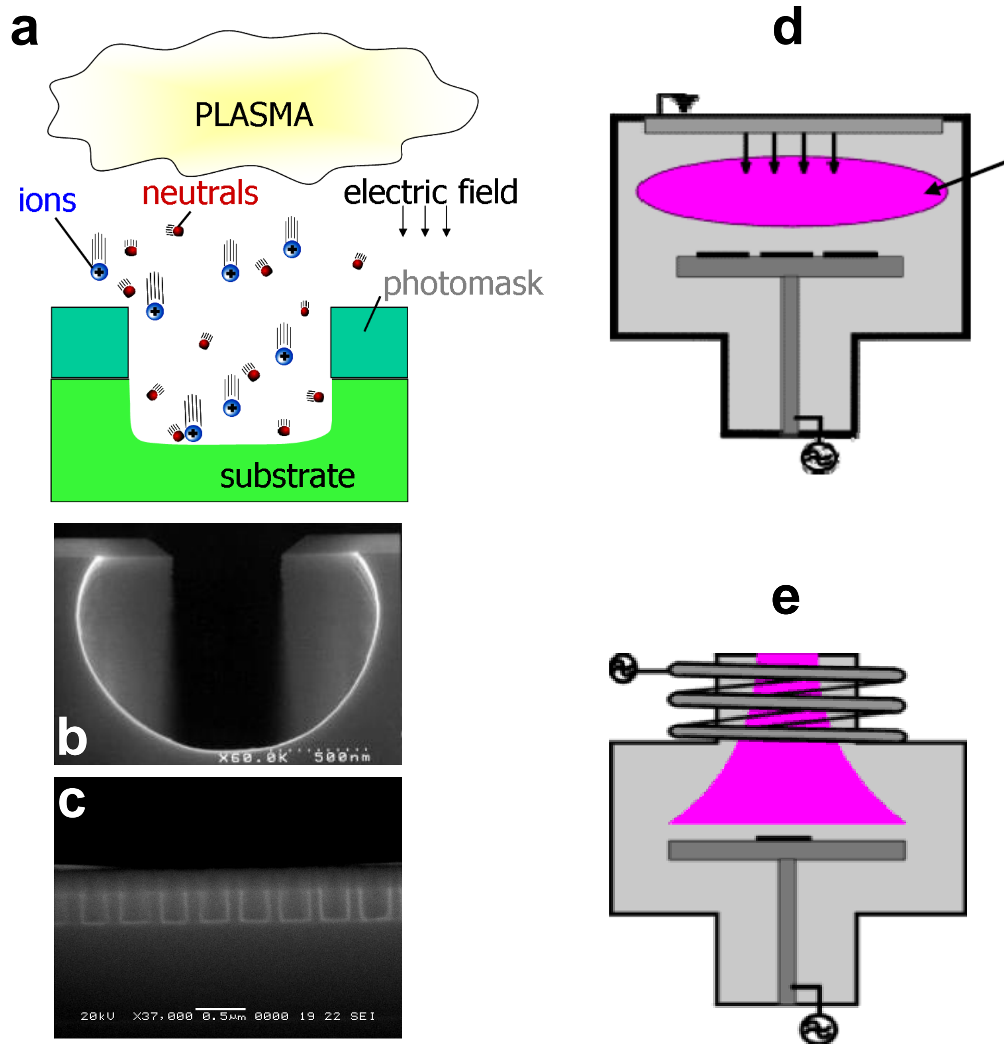

FIGURE 2.6: (a) Typical plasma etching process. (b) Etching of silicon with fluorine and chlorine gases (c)(images from Oxford Instrument). (d) working principle of RIE process. (e) Working principle of ICP-RIE process.

is created in the system at low pressure by applying a strong RF. Once ionization has begun in the gas by the application of energy, the free electrons strike neutral gas molecules generating more electrons and ions. The interaction of these electrons with the gas molecules could be different; ionization, dissociation of gas molecules leading to radical formation and electron impact excitation. The ions (and electrons) created in this process are accelerated by applying an electric field, which can be obtained through two asymmetric parallel plates in which a voltage is applied. Plasma can interact with the surface of the sample during the etching in different ways, ion

bombardment (sputtering), radical chemical reaction and ion assisted chemical reaction. Usually the etching processes can be isotropic or anisotropic. The processes with a pure chemical etching (similar to the wet eching) do not need ion bombardment for reaction and in this case there is no directionality on the etching (see Figure 2.6(b)). For anisotropic etching (normally the desired one), the process needs ion bombardment, so the reaction can take place and the obtained etching has a vertical profile (see Figure 2.6(c)). In a RIE, as well ICP-RIE process, chemical and physical reactions take place. The most important difference between ICP-RIE and RIE is shown in Figures 2.6(d)(e). Respect to RIE, in a ICP-RIE there is a physical separation between the plasma generation (it is created through inductive coil) and the ions acceleration. This gives to an ICP-RIE a higher control on the etching process respect to the standard RIE, in particular a higher confinement and higher ion flux uniformity with a more intense plasma and thus deeper etching.

PlasmaPro 100 Estrelas system

PlasmaPro 100 Estrelas system (Figure 2.7) allows Inductively Coupled Plasma and Reactive Ion Etching, where the plasma is created at a frequency of 13.56 MHz. Different materials (dielectric, metals, semiconductors, organic materials etc.) can be etched due to the use of a different gases and thus, different plasma. Up to 4-inch diameter wafers can be loaded in this system. Apart of N_2 and He used for venting and controlling or monitoring the stability of the wafer, in our system different gas line are available (O_2, Ar, H_2, CH_4, SF_6, C_4F_8, CHF_3, Cl_2, BCl_3). Their use depends on the material to be etched (and the used mask). In our system, a valuable information on the process in real time can be obtained thanks to the DC bias parameter. It is defined as the average direct current (DC) offset of the wafer electrode from zero (earth potential). DC bias is due to the faster electrons originated in the process ($\approx$2000 times faster that ions), charging a blocking capacitor, giving a

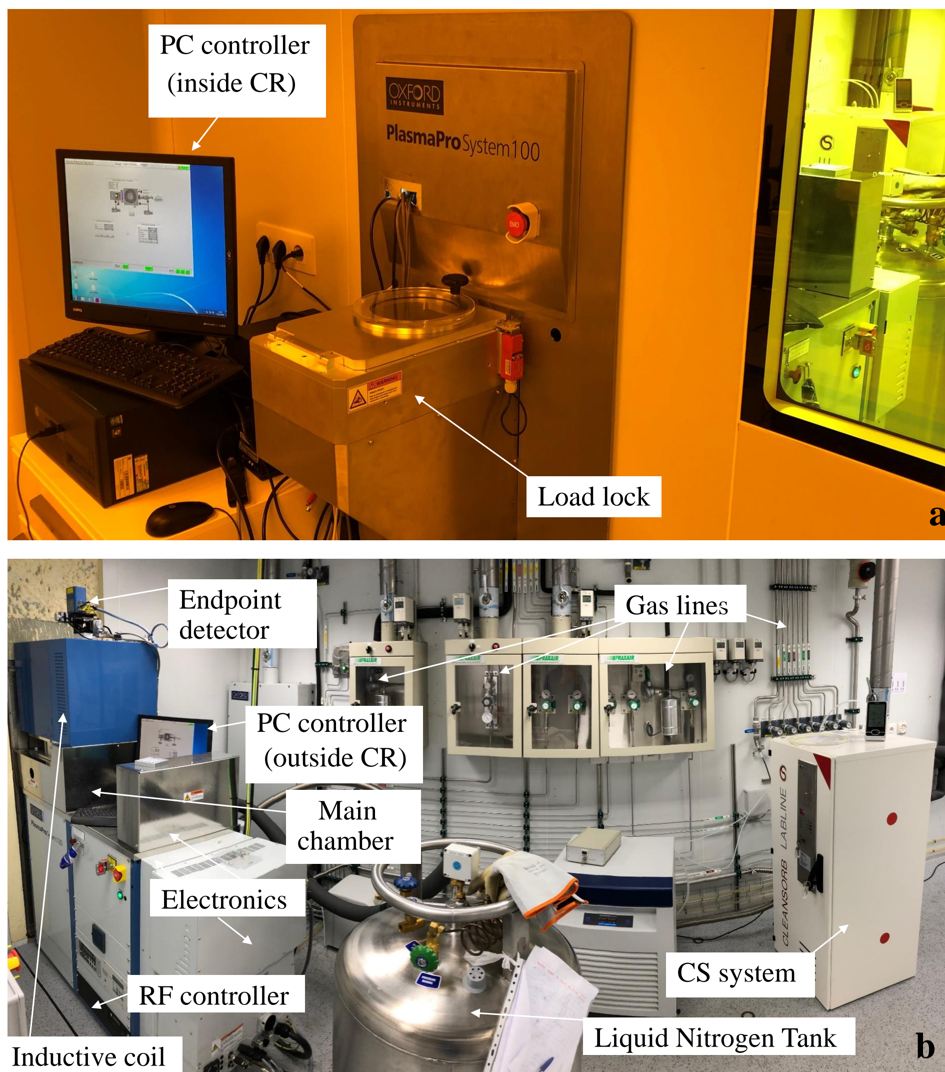

FIGURE 2.7: (a) ICP-RIE load lock and PC controller inside the clean room. (b) Rest of the equipment installation in the technical room.

rapid response to electric fields varying at RF frequencies. Our system is equipped with a cryogenic module allowing to work down -120° to perform cryo-etching. This option had a crucial role in the fabrication of graphene nanoconstrictions (see Chapter 5). Moreover, it has an interferometer system (endpoint detector) that allows a full control in the etching during the process. As shown in Figure 2.7(a) only the load lock (for load and unload the samples) and one of the two controller PCs are inside the clean room. The main body of the equipment (gas line, pumps, nitrogen tank, Clean Solution (CS) system for toxic gases waste) are disposed in the technical room (Figure

2.7(b)).

2.1.6 Mask aligner MJB4

Optical lithography were carried out through MJB4 mask aligner.

Working principle of the optical lithography

The working principle of the optical lithography is schematically shown in Figure 2.8(a). The light of a source (lamp) is collected through optical elements (lens and mirrors) to the sample. An optical mask with a metal pattern (see for example our mask in Figure 2.8(b)) is interposed between the source and the sample (very close to the latter) to expose only those parts of the resist unconvered by the metal pattern of the optical mask. After exposition, the chemical bindings are weaker or stronger (it depends on the tone of the resist, positive or negative), similar to the e-beam resist (see section 2.1.3), in the exposed area of the sample. Then the weaker parts are removed through a developing process. At the end of the optical lithography process, only a part of the resist with the pattern remains on the sample. The resist mask on the sample can be used for etching or depositions of metals/dielectric in the same way as we mentioned on the subsection 2.1.3.

MJB4 mask aligner

Figures 2.8 (c), (d) show the front and side views of the MJB4. Through the optical microscope and the micrometic screws (x,y) with a resolution of 0.1 μm and a maximum rotation of $\pm 4^{\circ}$, it is possible to align the sample with the mask. The sample is fixed to the chuck with a vacuum line; vacuum is also used to fix the optical mask to the mask holder. Through a coarse level and micrometric fine screw is possible to bring in contact the optical mask and the sample before exposition. MJB4 works with different exposure modes:

soft, hard, vacuum, soft vacuum contact and gap exposure (10-50 μm). The wavelenght range of the optical lamp varies between 240 nm (deep UV), 320 nm (UV) and 450 nm (visible light). Mask size up to a square of 5 inches can be used, but the maximum sample size permitted is a circle of 4 inches.

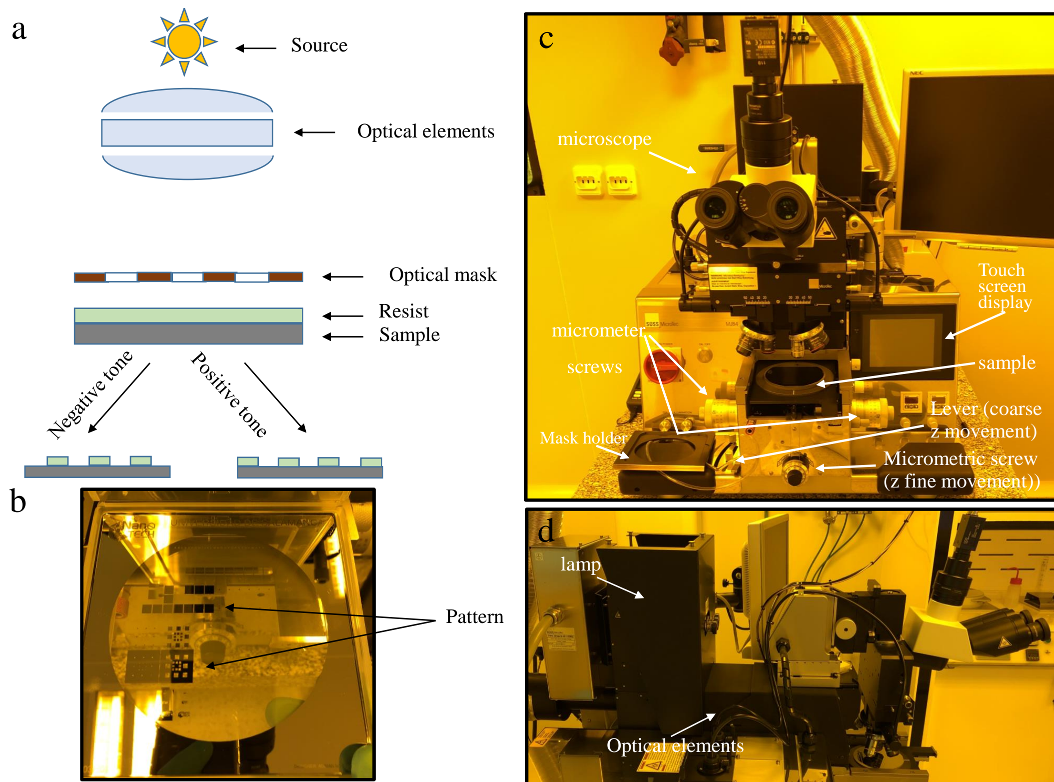

FIGURE 2.8: (a) Working principle of optical lithography. (b) Optical mask lithography. (c) Front and (d) side views of the MJB4 mask aligner.

2.1.7 Fume Cupboards for lithography and for chemical processes

In the Clean room we have two different fume hoods; a hood for the use of resist in the litography room and a second one for chemical uses in the evaporation room. Both fume hoods have an independent extraction system (carbon free) that guarantees the extraction of the toxic gases and they are made of materials that permits the use of very corrosive liquids. The residual gases are purified thanks to a chemical scrubber in the roof of the I+D+i

building before the release in the external environment. In the resist cabin there are a spin coater SÜSS MicroTec (maximum speed of 8000 rpm) and two hotplates. In a spin coating process, the resist (usually for optical or electron beam lithography) is deposited by using the spinner on a substrate with a uniform thickness of hundreds nanometers. Finally the resist is baked on the hot plate. In the chemical cabin there are an ultrasonic cleaner and a magnetic hotplate, usually employed for cleaning, lift-off and wet etching processes.

2.1.8 E-beam evaporator

The evaporation of metallic contacts in our devices was performed using an e-beam evaporator.

Working principles

A beam of electron, that is generated with an e-beam gun, is accelerated and focused to the evaporation material through a permanent magnet and/or electromagnets. Focusing the e-beam into the material, the electrons will lose their energy and this will be converted into other forms of energy through interactions with the material. The thermal energy, that is produced by the electrons, heats up the evaporation material causing it to melt or sublimate. Finally, when a suitable evaporation conditions have been reached, the material starts to evaporate from the melted material or will sublimate from the solid material.

Tecnovac E-beam evaporator with Telemark e-beam gun emitter

Our e-beam prototype was designed with the help of Tecnovac and it has two independent chambers. They can be isolated or connected using a manual guillotine (Figure 2.9 (a)). The larger main chamber is usually under high-

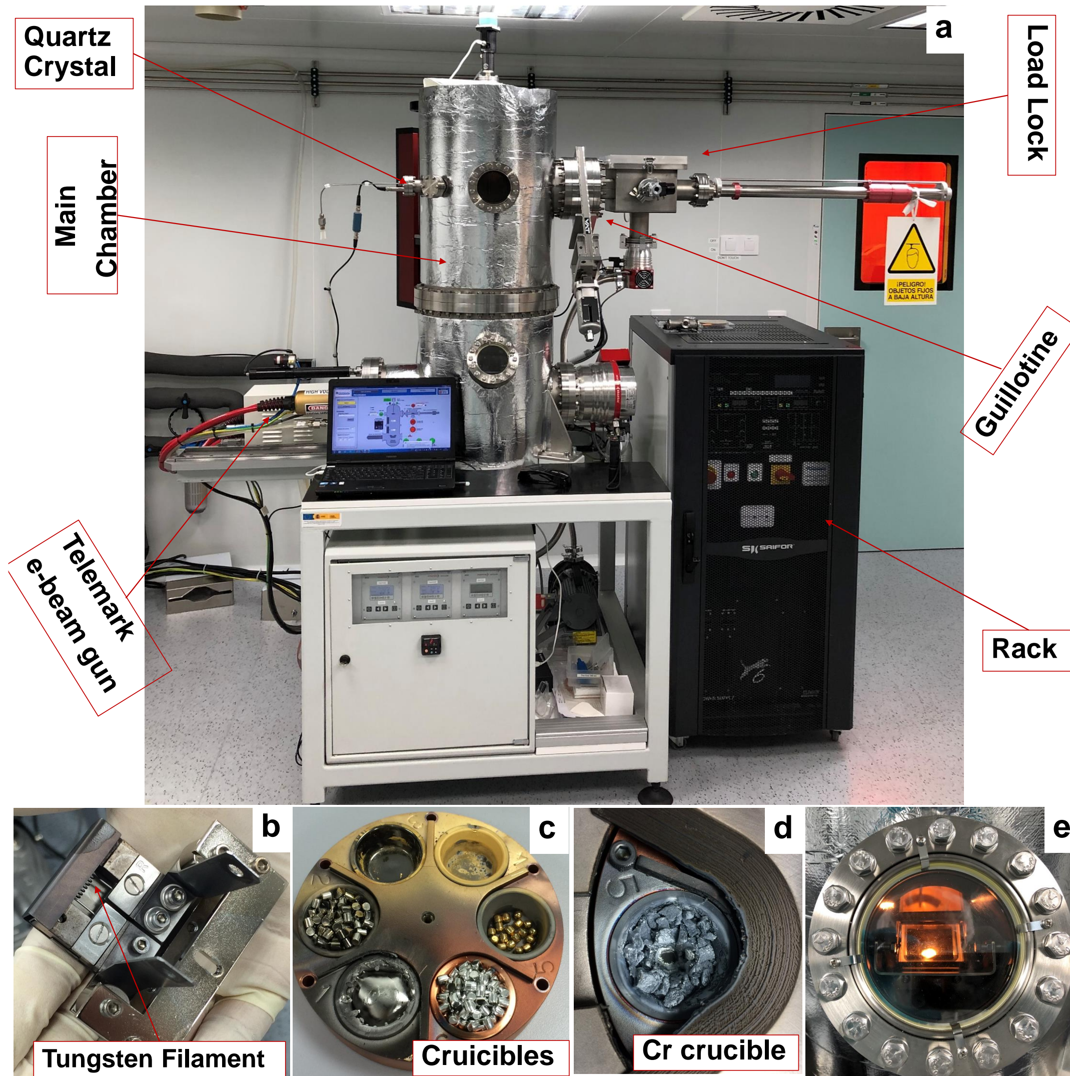

FIGURE 2.9: (a) E-beam evaporator designed by Tecnovac, with Telemark e-beam gun. (b) E-beam source model 244. (c) Crucible pocket and (d) detailed Cr-crucible. (e) Photo during an evaporation (view from an external window thanks to an internal periscope).

vacuum (10^{-9} mbar or lower). The smaller secondary chamber or load-lock chamber (Figure 2.9(a)) is used for load and unload the sample when the chamber achieves an adequate pressure range (lower than 10-5 mbar in less than 60 minutes). The samples are loaded (or unloaded) into (or from) the main chamber through a mechanical arm while keeping the main chamber under high-vacuum. The long distance between the material and the sample (almost 1 m) and the operation at very low pressures, ensure a high control on the evaporation rate (less than 1 Å/s) creating high homogeneity thin

films on the samples but with a high consumption of metals. The evaporation rate, as well as the evaporated metal thickness, is measured by a quartz crystal controlled by a TTL controller. The system is equipped with an e-beam gun from Telemark with a e-beam source model 244, in which electrons are generated by a tungsten filament (see photo 2.9(b)). The emitter assembly is located outside the evaporation zone to avoid becoming contaminated by evaporant. The control of the equipment takes place through an external rack. Electrons source is obtained by applying a small emission current to the filament, when the filament becomes enough hot, it begins to emit electrons. In our system, electrons are by applying a high voltage (8 kV) and can be leaded by the magnetic field to the center of the pocket with crucibles filled with different metals (target). These metals can be initially shaped like ingots or rods (Figure 2.9(c)(d)). Through the "XY Sweeping", the e-beam is loaded and sweeped on the entire crucible by the magnetic fields, so that all material is homogeneously evaporated. Thin film coating can be evaporated and deposited on the sample. Several materials can be evaporated in our system using the e-beam evaporator (Au, Cr, Ti, Al, Ni, Co, Pt) as well as some dielectrics (SiO2, Al_2O3, HfO_2). The use of the machine is actually limited to metals to avoid any contamination with dielectrics, because the main purpose is the evaporation of ohmic contacts. A typical evaporation process, in which the metal is heated up as the emission current is increased until its conversion to a gaseous state, is shown in Figure 2.9(e).

2.1.9 RTP As-One100

Annealing processes were performed with the system Rapid Thermal Processing (RTP) As-One 100 (Figure 2.10 (a)). In our processes, an annealing was performed for cleaning the substrate and removing the bubbles off the graphene heterostructures.

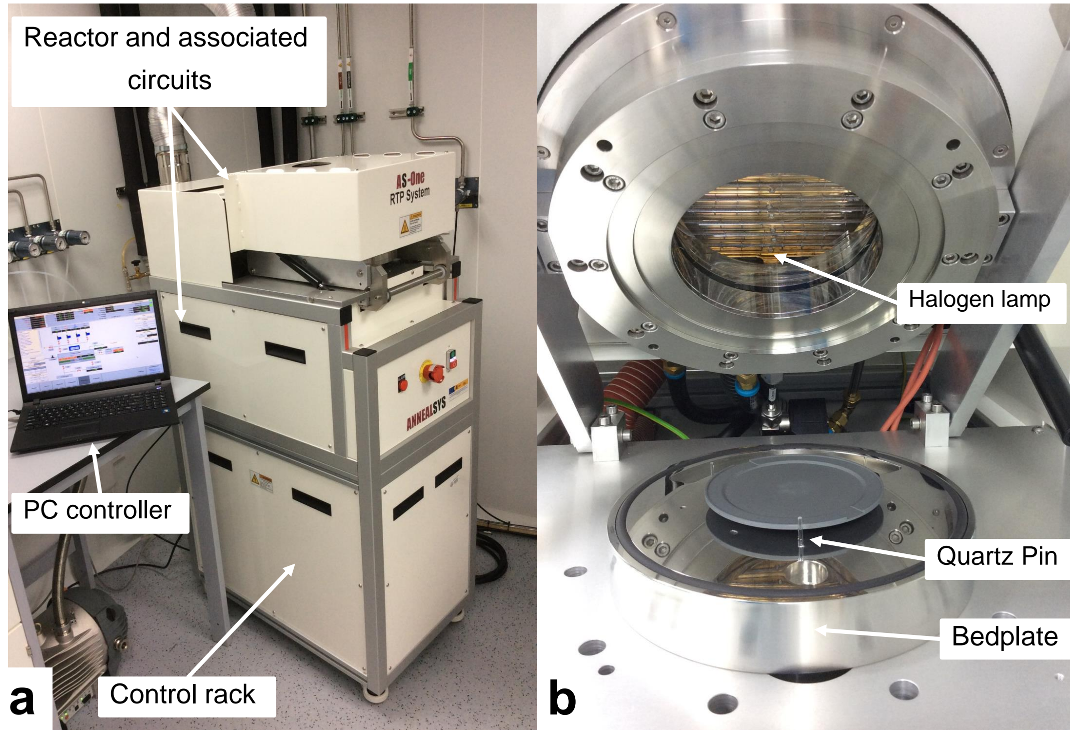

FIGURE 2.10: (a) RTP As-One100. (b) Internal chamber with the lamp furnace.

The system is divided in two parts; in the upper part, there is the reactor and the associated circuits (process chamber, lamp furnace, cooling circuit, gas lines, vacuum line and turbo pump). In the lower part the control rack (temperature controller, board for the mass flow controller, transformers, power block) is located. The full annealing process can be monitored and controlled by PC. Two pyrometers, located in the bedplate (Figure 2.10), permit the temperature control. The process can be performed from vacuum (10^{-5} mbar) to atmospheric pressure. Three quartz pins (designed to reduce the thermal transfer with the substrate) hold the substrates. A halogen tubular lamp furnace heats the substrate through the quartz window. The tubular halogen infrared lamps are installed in a stainless steel water-cooled and polished reflector. The hot air is evacuated on the backside of the furnace.

The system allows recipes with a temperature range from room temperature up to 1500 °C with an accuracy of 2 °C/s, a maximum ramp of 200 °C/s and cooling rates up to -100 °C/s. The lower temperature pyrometer control

monitorizes the temperature from 150 °C to 1000 °C, the higher temperature pyrometer control from 400 °C to 1500°C. Nevertheless, the maximum process duration is limited at high temperatures due to the cooling capacity of the machine (i.e. at 950 °C the maximum duration process is limited to 3 hours meanwhile at 1500 °C the maximum duration is reduced to 30 seconds). In the system, the annealing process can be performed with the use of different atmospheres through 4 different gases or mixtures of them (Ar, O_2, He, N_2).

2.1.10 DM8000 Optical Microscope Leica, DektakXT Bruker Profilometer and Harrick Plasma cleaner

We used a Leica DM8000 Optical Microscope Leica, a DektakXT Bruker Profilometer and a Harrick Plasma cleaner (Figure 2.11) for a preliminar characterization of 2D flakes, heterostructures or samples.

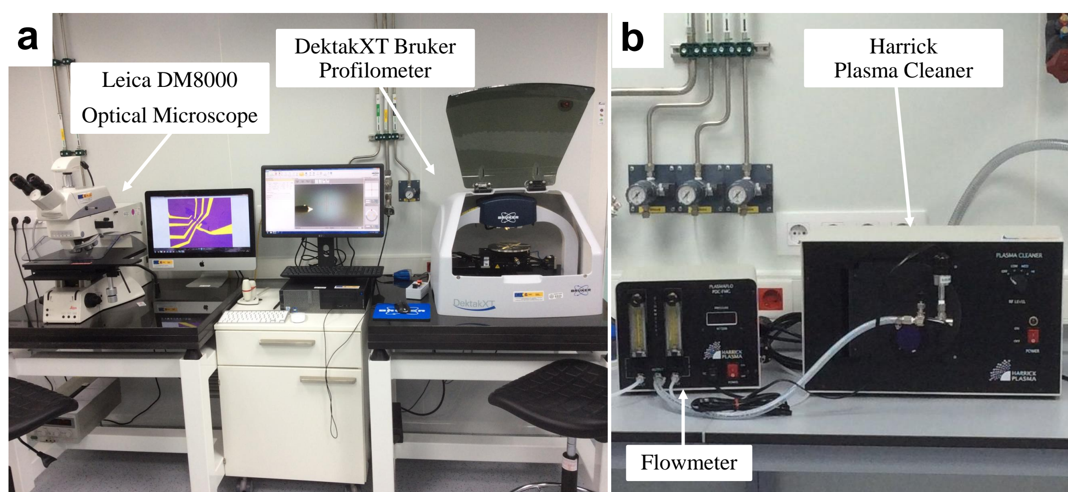

FIGURE 2.11: (a)Leica DM8000 Optical Microscope and DektakXT Bruker Profilometer (b) Harrick Plasma cleaner.

Leica DM8000 Optical Microscope

The Optical Microscope (Figure 2.11(a) left side) was used for a optical identification of graphene and hexagonal Boron Nitride (hBN) flakes and in general for a qualitatively control of the samples/devices. It has six objectives with different magnification and working distance (5X, 10X, 20X, 50X (short and long working distance), 100X). A LED illumination is integrated within the microscope, as well a motorized aperture diaphragm, filters and different contrast modes: Bright Field (BF), Dark Field (DF). It is coupled to a camera and with the Leica LAS software. In this way the optical images can be treated.

DektakXT Bruker Profilometer

The DektakXT system (Figure 2.11(a) right side) is an advanced equipment to perform thin (down to few nm) and thick (up to hundreds of μm) film step height measurement. For this thesis work, it was used to measure the thicknesses of the 2D-flakes, metal deposition, chemical or dry etching. The system is able to measure roughness in the nanometer range, in addition to profiling surface topography and waviness. It has automatic X-Y-theta stages and provides a step-height nanometer resolution. Apart of two-dimensional surface profile measurements, the DektakXT system can perform three- dimensional measurements creating 3D Maps with micrometer resolution in the (x,y) plane. A diamond-tipped stylus is electromechanical controlled over the sample surface according to a desired scan length, line speed and stylus force (from 3 to 15 mg). The stylus is connected to a Linear Variable Differential Transformer (LDVT), which produces a feedback signal (processes electrical signals). This signal corresponds to surface variations of the sample. The surface information is converted to digital format and so they are stored for display and analysis. For this scope, we use the Vision64

software, which is able to calculate and display the results of user-selectable analytical functions for measuring surface texture and other parameters to characterize the profile data.

Harrick Plasma cleaner

The plasma cleaner (Figure 2.11(b)) was largely used for cleaning of the substrate (removing organic contamination from surface) and/or functionalisation of the surface (modification of the physical and chemical characteristics of surface). In our case we used silicon and silicon oxide substrates or glass slides). The basic principle of this equipment is similar to a RIE, but less complex. At low pressure, when a gas is subjected to a high frequency electromagnetic field, its atoms and molecules are ionized creating a plasma. Once the sample is placed in the plasma cleaner chamber, the plasma is created at a pressure between 800-1200 mtorr with a glass flux of 5-10 SCFH of process gas (typical O_2 or Ar) and applying a radio frequency (8-10 MHz) generated through a 29.6W power source with RF coil at room temperature.

2.2 2D-Transfer setup

One of the first and more important work during my PhD studies consisted in designing and calibrating our homemade 2D-Transfer setup. The system was conceived by my supervisor and me, inspiring by the the 2D-Transfer setup of HQ Graphene, where in May 2015 I received a first preliminary training on the transfer of 2D materials by Paul Zomer and Niko Tombros. For assembling and testing the system, it is necessary to highlight the fundamental contribution of my colleagues, Juan Antonio Delgado Notario and Adrián Martín Ramos.

The transfer system (in Figure 2.12) is equipped with an optical microscope (Nikon microscope) with large focal distance optical objectives (Magnification x10, Numerical Aperture 0.30, Working Distance 16 mm and Magnification x20 optical, Numerical Aperture 0.40, Working Distance 11 mm) . The microscope is connected to a camera, so the transfer process can be

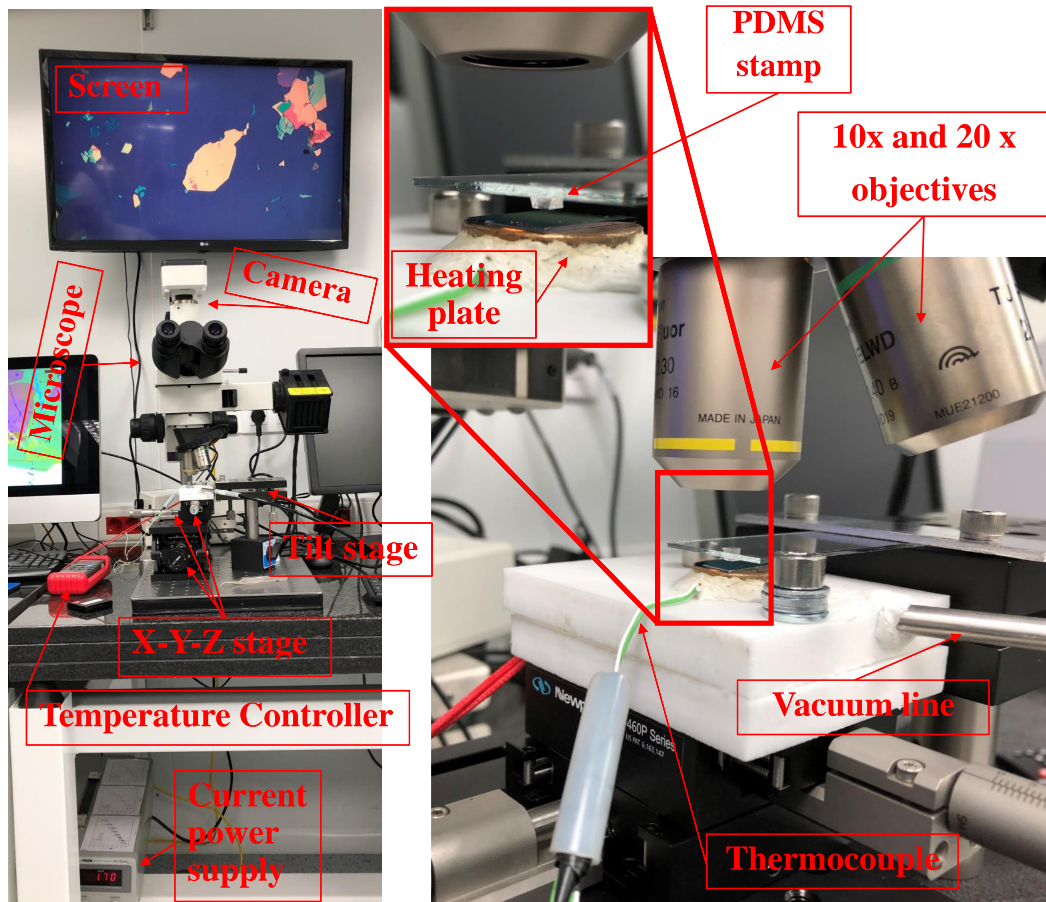

FIGURE 2.12: Transfer setup: Optical microscope, X-Y-Z- micrometer and tilt stages, Camera (and screen), Heating plate and current power supply, PDMS stamp.

visualized on an external screen. The system was used to fabricate different kind of heterostructures with bidimensional materials (hBN/graphene, hBN/graphene/hBN, hBN/graphene/graphite heterostructure as well as the transfer of other 2D materials). During the transfer, the alignment was made with a XYZ micrometer stages, that includes an homemade heating plate, where the samples are located. The flakes are transferred by a stamp, attached to a tilting micromanipulator, that ensures a high degree of freedom

in the alignment of the 2D crystal flakes. The homemade stamp consists in a pyramidal piece of PDMS (Polydimethylsiloxane), obtained by a mixture (10:1) of SYLGARD 184 silicone elastomer base and curing agent, baked in a Petri dish at 75 C° for three hours. The stamp is attached on a microscope glass slide and a polycarbonate (PC) film or Polypropilene carbonate (PPC) film is deposited on the PDMS stamp. The transparency of the stamp guarantees the visibility of the substrate through it and thus permits the alignment. The substrate is fixed with vacuum and heated during the transfer process. For the control of the temperature, we used an heating element for soldering, assembled and thermically coupled to a pure copper cylinder. The temperature is monitored by a thermocouple temperature sensor coupled with the same copper cylinder.

2D- transfer setup had a fundamental role for this thesis work, since one of the most important result was the fabrication of devices based on 2D materials heterostructures. The processes through the use of the 2D- transfer setup will be thoroughly described in Chapter 3.

2.3 Equipment for preliminary characterization: MicroRaman, Probe station and Time Domain Spectroscopy (TDS)

2.3.1 LabRAM HR Evolution MicroRaman

The MicroRaman is located in the technical room (so outside the clean area). Its use is fundamental for the characterization of hBN, graphene and other 2D materials, as well as for the quality check of stacked heterostructures.

Principles

An electromagnetic wave (typically UV, visible, IR light) can interact with a material in different ways, it can be absorbed or it can be scatterated. The last process can be divided in (see Figure 2.13(b)):

Rayleigh elastic scattering: photons have the same frequency (same energy and wavelenght) of the incident light.

Raman inelastic scattering (Stokes): photons have a lower frequency (lower energy and higher wavelenght) of the incident photons.

Raman inelastic scattering (Anti-Stokes): photons have a higher frequency (higher energy, lower wavelenght) of the incident photons.

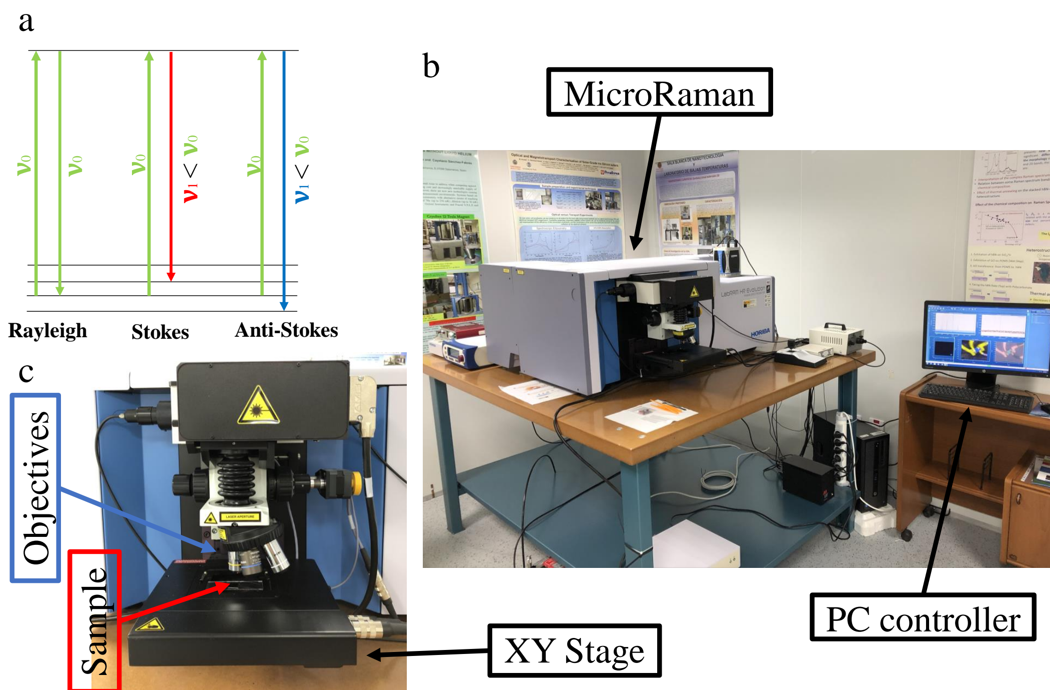

FIGURE 2.13: (a) Rayleigh, Stokes and Anti-Stokes processes. (b) LabRam HR Evolution MicroRaman. (c) Front view of the equipment.

The Raman effect, based on the inelastic scattering of photons, is used by Raman spectroscopy to study vibrational, rotational and other low-energy excitations of a chemical/physical system. The probability of the inelastic

scattering process respect a Rayleigh process is very low (only 1 out of 10^5-10^8 photon have a Raman scattering process). For this reason, Raman spectroscopy needs an intense and monochromatic laser source. A Raman spectra gives the information due to the intensity of light scattered by a sample (i.e. number of scattered photons) as a function of the frequency shift with respect to the exciting incident light. Typically in a Raman spectra, the frequency is replaced by wavenumber ($\Delta w = \frac{1}{\lambda_0} - \frac{1}{\lambda_1}$). Different kind of information about the sample can be obtained from a Raman spectra according the number, position, height and width of peaks and bands in the spectra.

MicroRaman

The Micro Raman Spectrometer – LabRAM HR Evolution (Figure 2.13(b)(c)) was used to carry Raman measurements. As light source the equipment disposes three different lasers:

- Ventus Solo laser at 532 nm with an output power of 100 mW
- He-Ne laser at 633 nm with an output power of 17 mW
- Diode laser at 770-795 nm with an output power > 200 mW

The LabRAM HR system offers the possibility to obtain micro and macro measurements, through confocal imaging capabilities in 2D and 3D. It is equipped with three different objectives, 10x and 50x with long working distance and 100x for very high resolution but very low working distance. Thanks to the flat nature of used substrates and samples (very low thickness 2D materials) in this thesis work, all the spectra are taken with the maximum resolution (100x), obtaining a spot of injection of almost 1μm. Filters can be attenuate the incident light till values of 0.01 % of the output power. The range of the Raman spectra can have a frequency shift from a relatively low wavenumber (cut-off of 50 cm^{-1}) and with an accurate step below of 2 cm^{-1}.

With a XY motorized stage (Figure 2.13(c)) a step of 0.05 μm can be achieved. The scattered light is collected in confocal configuration and analized with two different diffraction gratings (1800 grooves/mm or 600 grooves/mm). Raman spectrums are obtained with the use of a 256x1.024 pixels Synapse CCD detector (spectral range of 200-1.050 nm).

2.3.2 Probe stations 4-probes:Cascade Summit 1100B Station and TPT BH10 Wire Bonder

A first characterization of the samples was made in the 4-probes Cascade Station (2.14(a)), that is located in the terahertz laboratory. It has a (x,y,z θ) stage (1 μm resolution) and 4 tungsten tips of 38 μm of diameter to contact with the pads of a sample. In particular this equipment was used to check the ohmic behaviour of the contacts at room temperature. For a full charac-

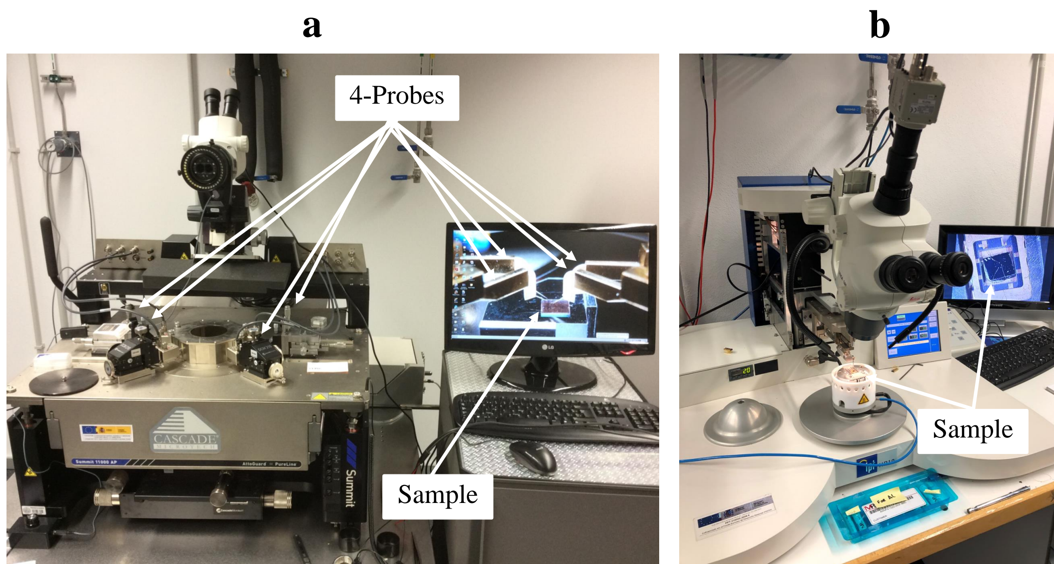

FIGURE 2.14: (a) 4-probes Cascade Summit 1100B Station. (b) TPT BH10 Wire Bonder.

terization of the samples it was necessary to bond them to a standard Double In Line (DIL) holder (8 pins or 20 pins). In this way nano/micrometer samples can be easily managed. The TPT BH10 Wire Bonder was used for this aim (see Figure 2.14(b)). The connection was obtained bonding a 50 μm gold

wire to the samples using wedge bonding. Our machine has a automatic bond height adjustment and a touch panel, in which the parameters (force, ultrasonic power for the wire cut, time) can be accurately chosen.

2.4 Facilities for Magnetotransport measurements

During this thesis work, different transport measurements were carried. The major part of the measurements were carried in Salamanca with different cryostats (Optistat AC-V12 3K cryostat, Triton 50 mK system), meanwhile the measurements in the Chapter 4 were performed in the High Magnetic Field Laboratory (HFML) during my stay in Nijmegen (Holland). Every equipment has different characteristic and they were used according our convenience/necessity (range of temperature, magnetic field range etc.). In Optistat cryostat and Triton system the samples are kept in vacuum conditions (less than 10^5 bar). These two systems are also equipped with pulse tube to achieve 3K.

Pulse tube technique

Since the measurements in this thesis ranging from 50 mK to room temperature, there was a real need of an alternative solution to systems based on the refill of liquid Helium at each use. In fact the cost of the liquid Helium increased a lot in the last decades, first of all due to its shortage of supply. The pulse tube technique, based on thermodynamic cycles of compression and expansion of Helium gas, achieves temperatures around 3K at the (only) price of electric power consumption. Our low temperature laboratory was pioneer of this technology, since one of the first system in Spain was installed more than ten years ago in Salamanca.

In this thesis I used two cryostats based on this technology: the Optistat cryostat for temperatures up to 3 K and the Triton system for temperatures up to 50 mK.

The working principle is the following; At the initial temperature T_i, the initial pressure of the Helium is minimum, so opening the rotatory valve, the helium gas flows to the Pulse Tube (PT) keeping its temperature. The heat taken from the gas during this compression phase is removed by a heat exchanger, so reaching the pulse tube, the gas is adiabatically compressed. In this moment it achieves the maximum temperature (T_M) and the maximum pressure (P_H). Then, the gas flows through an small orifice onto a reservoir of large volume with small pressure oscillations, giving off heat to the surroundings. Then a reversed cycle starts (the expansion phase). The orifice is closed and the rotatory valve starts an expansion cycle of the gas cooling down the helium as it approaches the regenerator. Finally, a small hole is opened, letting the gas flows at constant pressure and a lower temperature ($T_f < T_i$) to the PT plate, absorbing the heat from the PT plate and cooling it down. The same cycle is repeated many times achieving a minimum temperature around 3 K.

2.4.1 AC-V12 (3 K) cryostat

Once the samples were bonded, for a temperature characterization, the faster way was through the Optistat AC-V12 cryostat (Figure2.15), which is cooled by a closed cycle refrigerator as explained previously. The system achieves helium temperatures without the use of cryogenic liquids. The samples, bonded on 8 (DIL) pins holder, are placed on this system are kept in vacuum and cooled by a Pulse Tube refrigerator as described previously. A temperature controller is used to control heating and temperature of the sample from 3K up to 325K with a temperature stability of $\pm$0.3K.

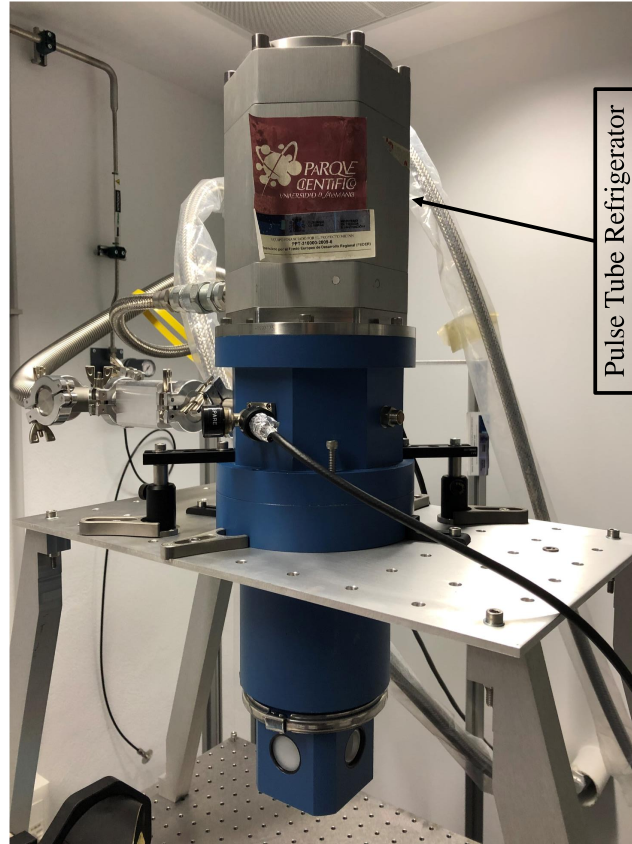

FIGURE 2.15: Optistat AC-V12 (3K) cryostat.

2.4.2 Triton (50 mK) cryostat and superconducting magnet

The transport measurements at very low temperature (50 mK) and quite high magnetic field (12 T) were carried out in the Triton system and superconducting magnet, located in the low temperature laboratory. Triton and the magnet are physically and thermally decoupled, which allows us to have a high magnetic field from very low temperature until room temperature.

The superconducting magnet in Figure 2.16 consists in a Ni_3Sn coil and an access bore diameter of 55 mm. It works with a high current ($\approx$ 100 A), that flows with no dissipation when the system is cooled with the pulse tube technique. The main advantages of a superconducting magnet are the low consumption of energy power, high stability and low vibration. The main disadvantage is the critical field of the superconducting phase (in our system 12T).

The Triton system, shown in Figure 2.16 allows to work a very low temperature (more than 1 order of magnitude) respect the AC-V12 cryostat. It is a dilution cryostat, since a mixture of ^{3}He and ^{4}He is used. ^{4}He pre-cooling cycle is obtained by the PT tube. The cycle results in cooling of the PT-plate down to ≈3 K. Nevertheless, when the PT-plate reach a temperature 30 K, the complementary ^{3}He circuit is activated. The mixing chamber of the Triton can be cooled down to ≈ 10 mK, but the sample holder (a 8-pins holder) achieves around 50 mK. One of the main advantages of this cryostat is represented by the possibility of maintaining the cooling of the sample independently from the cooling of the superconducting coil. This allows to perform magnetotransport measurements while the sample is kept at temperatures higher then the critical temperature of the superconducting phase of the coil's material.

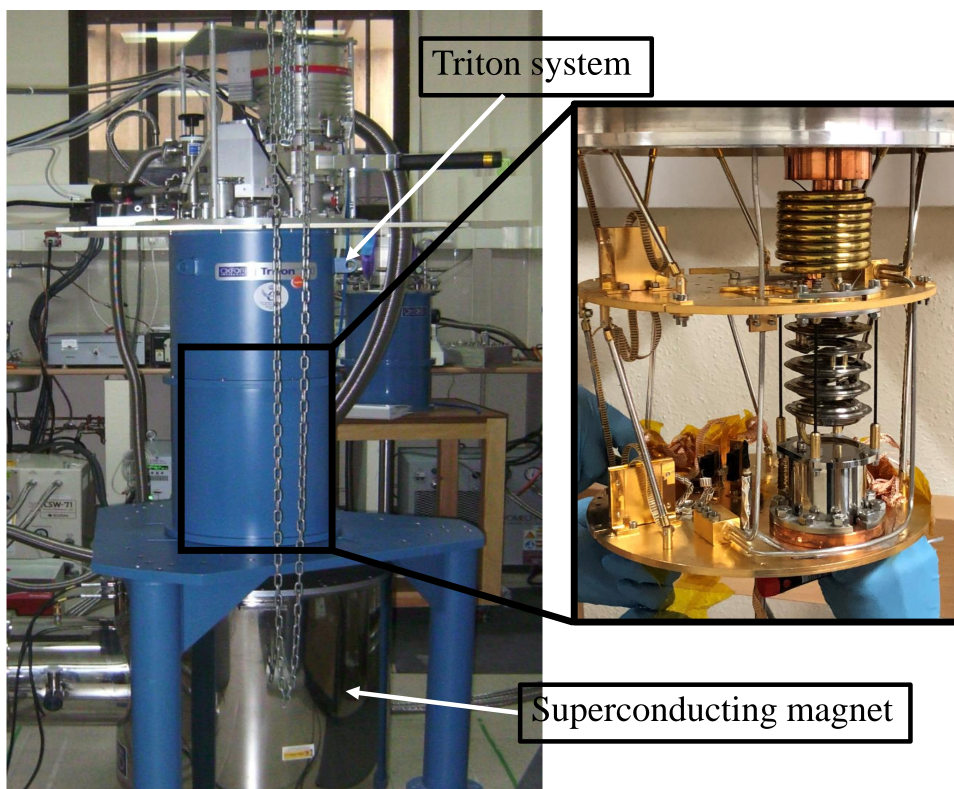

FIGURE 2.16: Triton system (left) and superconducting magnet (right).

2.4.3 High Field Magnet Laboratory (HFML)

The High Field Magnet Laboratory (HFML) (Figure 2.17(a)) is one of the few facilities with continuous high magnetic fields worldwide, since it disposes of 6 cells with Magnet with a field higher than 30T (Figure 2.17(b)) and various cryogenic systems. During my doctoral stays I used continuous-flow cryostats for the temperature range from 1.2 K to 300 K coupled with a Magnet up to 32T. Standard equipment for electrical transport measurements (voltage source, lock in amplifiers (Figure 2.17(c))) was also available. The samples were mounted in a 20-pins holder located in a homemade bar (Figure 2.17(d)). Though a continuous-flow cryostat, samples are cooled from room temperature to 4 K in 2 h, a recovering line permits to recover the major part of the used He as it escapes from the cryostat, although this technology is also costly to operate. The access to the HFML facilities is achieved after the acceptation of a proposal that can be submitted with a periodicity of 6 months. The work at HFML is organized in slots of 8 h per day (8-16, 16-00, 00-8).

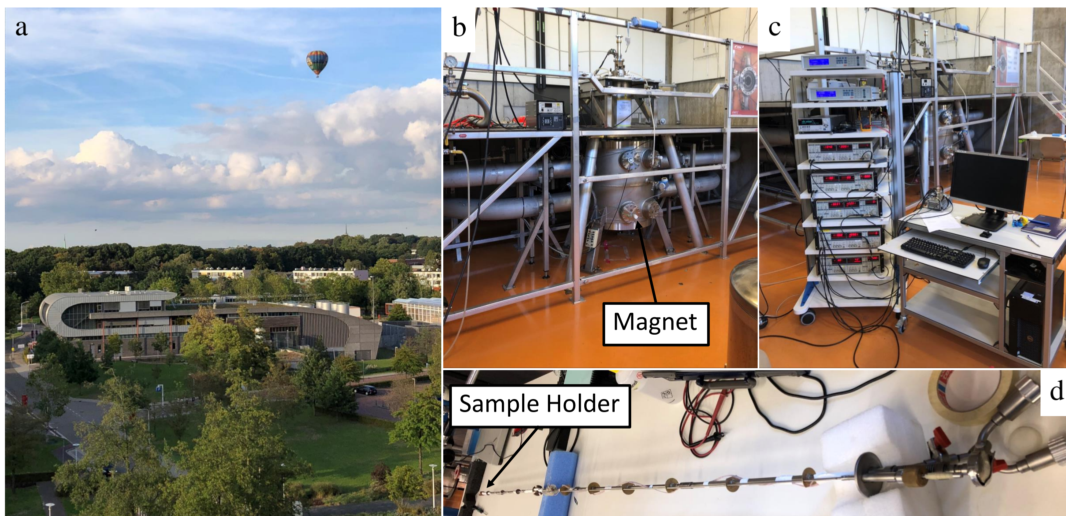

FIGURE 2.17: (a) HFML Facilities. (b) Magnet. (c) Setup for Measurements. (d) Homemade column with sample holder.

2.4.4 Other optical characterization: Terahertz - Time Domain Spectroscopy (THz-TDS)

Another technique for characterization of graphene is the Time Domain Spectroscopy (TDS), a technique in which different physical parameters could be extracted (conductivity, mobility, permittivity...) [21][22]. Many materials are transparent to terahertz waves and so they dispose of their fingerprint within this range. This allows non-destructive inspection and characterization within this range of different material like graphene. The possibility to obtain a THz-imaging of a big flake and mapping local conductivity has been recently demonstrated [23] which could extend the use of TDS-THz technique for quality control of large graphene flake made with different methods. In Figure 2.18 the setup of our THz-TDS as well as the schematic setup

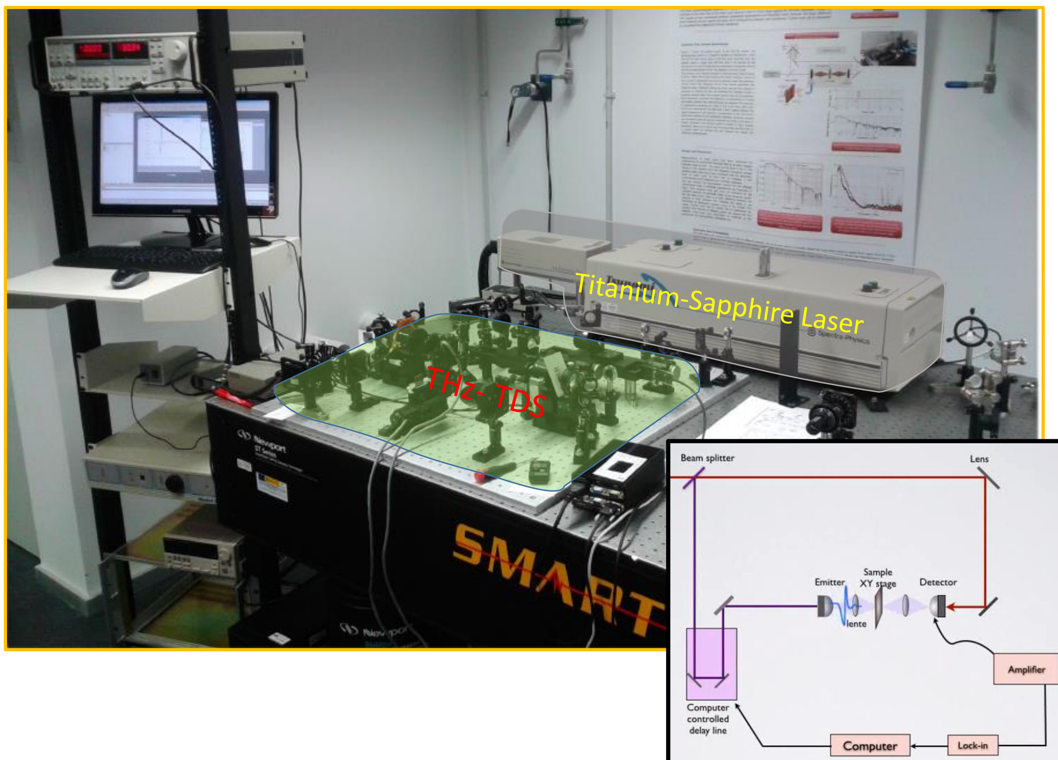

FIGURE 2.18: Photo of TDS setup. In the inset the schematic setup.

are shown. In this system two photoconductor antennas, illuminated by ultrashort laser pulses, are used for THz radiation and detection. The pumping

laser should provide the pulses of 760-840 nm wavelength, 50-150 fs pulse duration and 50-150 mW output power at approx 80 MHz pulse repetition rate. The optical beam is coupled to the system through a complex system of lens and mirror as shown in the Figure 2.18, obtaining a collimated beam of 3 mm-diameter. The signal from the THz detector is detected by a Lock-in amplifier SR-810. THz detector output is proportional to the instantaneous electrical field strength of THz pulse during ultrashort pumping pulse (which should be in 50-150 fs range for best results). By scanning with an optical delay line a 10-20 fs window steps can be achieved and the waveform of electrical field of THz radiation is build. The Fourier transform of waveform gives the spectral content of THz radiation. A comparison of the spectra with and without sample inserted into THz beam path gives the absorption or transmission spectra of the sample under investigation.

2.5 Setup Mesurements: Lock-in Amplifier and Sourcemeter

The measurements presented in this thesis work, were carried out in different laboratories using different equipments, but in all cases we used a standard setup with DC lock-in technique (Stanford research SR830) and sourcemeter (double channel Keithley 2412 source-meter) for all the transport measurements. The technique guarantees the control and detection of very small signals (nA of current and μV of voltage) and big increase of the ratio Signal/Noise (S/N).

2.5.1 Principles of the lock in technique

Basically in a lock-in amplifier an AC signal (current or voltage) is detected by the input channels and filtered by the amplifier. All the signals with a

frequency different from the reference are filtered, so only the signal with a component (phase-locked) with the same frequency of the reference signal is detected. In our case the reference signal is given by the AC frequency of the injection current (that is generated by the lock in itself). This method is known as phase-sensitive detection (PSD). The working principle is explained in the following.

If we consider a reference signal

$$V_R \approx sin(\omega_R t + \theta_R)$$

and a measured signal

$$V_S \approx sin(\omega_S t + \theta_S)$$

the lock in multiplies the signals, obtaining the output signal:

$$\frac{1}{2} V_S V_R cos((\omega_S - \omega_R)t + \theta_S - \theta_R) - \frac{1}{2} V_S V_R cos((\omega_S + \omega_R)t + \theta_S + \theta_R)$$

The result consists of two sinusoidal signals, with the difference of the two input frequencies ($\omega_S \ \ \omega_R$), and with the sum of these frequencies ($\omega_S + \omega_R$).

When the input signal has the same frequency than the reference signal (ω_S = ω_R), the difference signal becomes a DC value. So when the output signal is passed through a low pass filter, the sum of the frequencies (ω_S + ω_R) is filtered out and the resulting signal is:

$$\frac{1}{2} V_S V_R cos(\theta_S - \theta_R)$$

In this way the intensity of the resulting DC signal is proportional to the input signal (V_S) if $\theta_r = \theta_s$. All the components at frequencies other than the

one of the reference are filtered out. Typical reference frequencies are fixed between 3 and 15 Hz.

Setup

A typical setup in our measurements is shown in Figure 2.19(a).

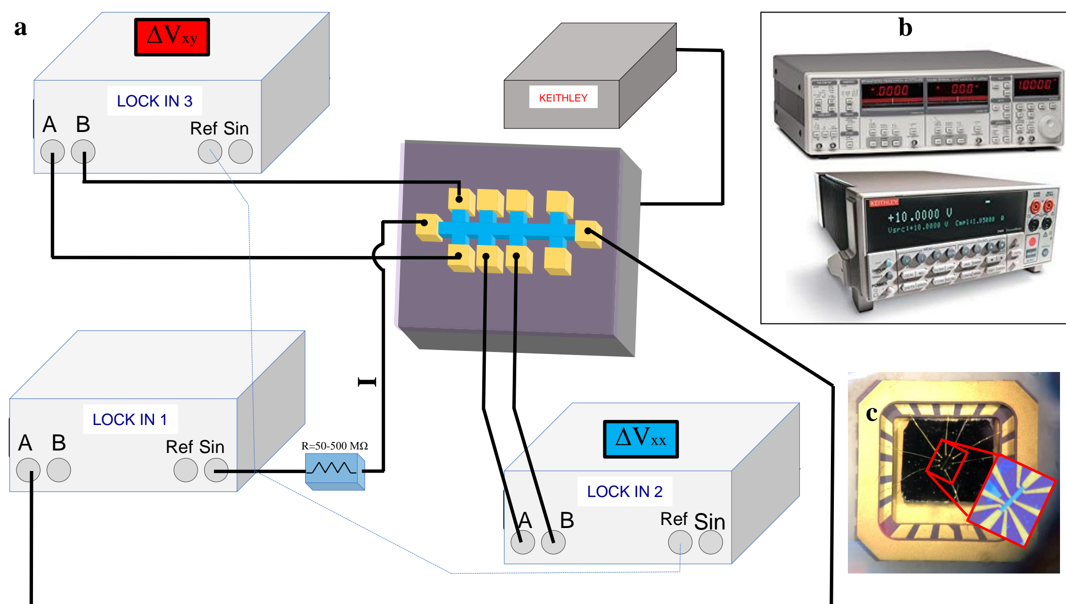

FIGURE 2.19: (a) Schematic view of a typical setup for the transport measurements with the lock in technique. (b) Lock-in amplifier SR830 (up) and Keithley sourcemeter 2612A (down). (c) 20-LCC pin holder in which we bounded one of our graphene Hall Bar. In the inset the Optical image of the same Hall bar of encapsulated graphene.

The reference signal is given by the lock in itself, using a high resistance (typically between 50-500 MΩ), located in series with the sample. The lock in technique works when the resistance of the sample (for example a graphene Hall bar as in the Figure 2.19 (c)) is much lower than the resistance in series, and the current value after the higher resistance is very closed to the current read in the lock in (I in the Figure 2.19(a)). The typical injection current was between 1-10 nA with a frequency between 11-13 Hz. The other lock in can be used for local or no local measurement, for example in the Figure 2.19(a) the longitudinal (ΔV_{xx}) and transversal voltage (ΔV_{xy}) of the sample

are measured. The lock in used for voltage detection are locked with the same frequency of the injection current (used as reference).

The Keithley sourcemeter was typically connected to the backgate voltage for the control of the charge carriers density.

Figure 2.19(c) shows a Leadless Chip Carrier (LCC) of 20 pins in which we bonded one of our sample (during this thesis we used also 8 pins DIL holder). In the inset an optical image of a Hall Bar, measured during the thesis with lock in technique, is shown.

Chapter 3

Devices: Fabrication and preliminary characterization

The fabrication processes and a preliminary characterization of devices based on graphene and other 2D materials are described in this chapter. The description was splitted according the material and the kind of the devices in the following way:

- Exfoliated graphene-based devices:

  - Hall Bar with graphene on SiO_2 with and without HMDS treatment and graphene nanoconstrictions on Hexamethilsilidazane.

  - Hall Bar with graphene on hBN.

  - Hall Bar with hBN-encapsulated graphene (with the option of the graphite backgate) and nanoconstrictions with encapsulated graphene.

  - FETs with encapsulated graphene.

- Epitaxial and CVD graphene-based devices:

  - Hall bar with epitaxial graphene.

  Hall bar with hBN encapsulated epitaxial graphene and top gate.

  - CVD graphene.

- Other 2D materials devices:

- $MoSe_2$ and $MoTe_2$ devices.

3.1 Exfoliated graphene-based devices

All the devices described in this section have in common the use of exfoliated graphene. Graphene is obtained by bulk graphite through exfoliation (as well as hBN, $MoSe_2$,$MoSe_2$ and other 2D materials can be exfoliated by the bulk material). Exfoliation is the starting step for a device fabrication with a 2D material. The mechanical exfoliation process, also known as Scotch^{TM} tape method [24] was firstly developed by Novoselov and Geim [25]. It basically consists in a peeling force applied to a piece of graphite (as well as other 2D materials) by an adhesive tape and the peeled sheet is detached during the peeling process on a substrate. The substrate is typically silicon oxide on silicon approximately cleaved in piece of 1 cm x 1 cm. In our process the thickness of the the silicon oxide was 90 or 290 nm, in this way flakes that would be completely transparent in other substrates, can be identified by optical contrast. Even if the mechanical exfoliation is a well-know process, many tricks and experience were achieved to obtain good quality flakes from different material. Placing or sandwiching a flake of graphene on/into hBN flakes improves the properties of the graphene flake [26], because hexagonal boron nitride is an ideal substrate and it is ideally suited for graphene to maintain its geometrical and electrical properties.

Here we present two different techniques to obtain graphene-based heterostructures. Both were implemented in Salamanca and used according to the convenience. In the first method we used a Polycarbonate (PC) film to stack all the flakes of the heterostructure. In the second method, a Polypropilene Carbonate (PPC) film was employed, but we typically used a different film for every step of the transfer process. Through the PC method [27], it

is possible to obtain some naked part of the graphene flake, in which planar contacts were used and the correspondent devices are more suitable as graphene-based current-injection devices [28]. In the other technique (PPC method), similar to [29], typically the graphene flake is completely encapsulated, so "side"or "edge"contacts are necessary and the fabricated devices result more stable over time, because of the low influence from the external environment. The probability of success of the first method, due the use of the same film in the whole process, is relatively low, but it is the best choice when it is necessary to obtain graphene on hBN without a top hBN flake. Regarding the preparation of the film for the transfer process, PC film preparation of the first method is more complex (and less controllable) than the preparation of PPC film (for the second transfer method). In this section we present the most common geometrical configuration used for transport measurements: Hall bar configuration with exfoliated graphene with different treatments (i.e. Hexamethylsilidazane (HMDS)) and/or use of hBN flakes. We will present magnetotransport measurements of these devices in Chapter 4. The nanofabrication process for graphene nanocostrictions is also described in this section and the correspondent measurements are presented in the Chapter 5. In the last part of this section we will discuss about the fabrication process of Graphene Field Effect Transistors (GFET) for detection of Terahertz (THz) radiation as well as the fabrication processes and preliminary characterization with other 2D materials ($MoSe_2$ and $MoTe_2$).

3.1.1 Graphene Hall Bars on SiO_2 (with and without HMDS treatment) and Graphene nanoconstrictions on HMDS

SiO_2 is the most common graphene substrate, but on its surface there are usually impurities, which can cause scattering of charge or act as charge traps. It is well known that graphene deposited on a hydrophobic substrate due

to hexamethyldisilazane (HMDS) treatment has better transport properties respect to the standard exfoliation of graphene on SiO_2 [30]. In particular, samples fabricated with HMDS treatment show higher carrier mobility and Dirac peaks closer to zero due to the low interaction of graphene with the substrate [31][32]. The use of HMDS modifies the first part of the fabrication process. The differences between the two exfoliation methods are:

- *No hydrophobic treatment*: During a standard exfoliation of graphene on SiO_2, the substrate was cleaned with acetone (ultrasonic bath for 3 minutes) then isopropanol (or ethanol) for 30 seconds and finally annealed in our RTP (see section 2.1.9) for 15 minutes at 400 °C in vacuum. For exfoliation we previously put thick natural graphite piece on a Scotch® Magic™Tape where they were folded onto itself. We transferred the thinner graphite pieces into another adhesive tape with lower force adhesion (Tape P/N 1009R-60 US (Ultron systems): Tape B). In the last step we transferred different graphene and graphite layers on the Si/SiO_2 substrate through the peeling process. The use of Ultron tape (instead of the direct use of Magic tape) guarantees a minor contamination of the graphene flake and of the substrate.

- *Hydrophobic treatment*: After the same cleaning and annealing of the no hydrophobic treatment, the substrates are immersed in a solution (1:1) of acetone and HMDS for at least 18h, before a fast cleaning in acetone (1-3 s) and isopropanol (10 s). A similar peeling process takes place obtaining graphene and graphite flakes on a thin film of HMDS on SiO_2 substrate. The exfoliation in this case is very hard as well as it is necessary a particular attention during the whole fabrication process considering the low adhesion of the flakes with the substrate.

After exfoliation a first characterization with the optical microscope by means of optical contrast can be done [33]. Mono, bi and tri-layer graphene

flakes (Figure 3.1(a)) have a pink and violet colour, because of the substrate transparency decreases with the thickness. Moreover, different colours from graphite flakes (dark blue, light blue or yellow by increasing the thickness) can be observed in Figure 3.1(b).

Then a graphene flake was chosen and Raman measurements were carried out. Raman spectra gives us a first estimation of the quality of the graphene flake, the number of layers, as well as the presence of the HMDS, in case of its treatment. Figure 3.1(c) shows the normalized Raman spectra of two different graphene flakes. The black and red lines show the Raman spectra of a monolayer graphene on Si/SiO_2 substrate without and with HMDS treatment, respectively. The intensity is normalized to unity, in this way it is clear the difference of ratio between the 2D-peak and the G-peak. The shift between G and 2D peaks (Figure 3.1(c)) depends on the doping level [34]. The enhancement of the ratio on graphene with the HMDS treatment (larger than a factor 3) is an indication of the improvement of the crystalline quality of the sample [35].

After Raman characterization, firstly, the device geometry was adapted to the geometry of the layer, measuring the distances between the flake and the closer alignment marker (the periodicity of gold markers on the Si/SiO_2 substrate was 400 μm). After a coating of PMMA (diluited in chlorobenzene at 4%, spinned at 4000 rpm and 1000 rpm/s for 60 s, baked at 160 °C for 10 minutes) we defined ohmic contacts and Pads through electron beam lithography (EBL) at 15 kV (aperture 10 μm and dose of 230 $\mu C/cm^2$, writing field (WF) of 500 μm for ohmic contacts, aperture of 60 μm, dose of 400 $\mu C/cm^2$ and WF of 1000 μm for pads). The graphene flake was completely contacted after a subsequent evaporation of titanium (5 nm) and gold (40 nm) with our e-beam evaporator (for details of electron beam lithography and e-beam evaporator see sections 2.1.3 and 2.1.8) and lift-off in acetone.

For the Hall Bar configuration, through a second step of EBL (aperture

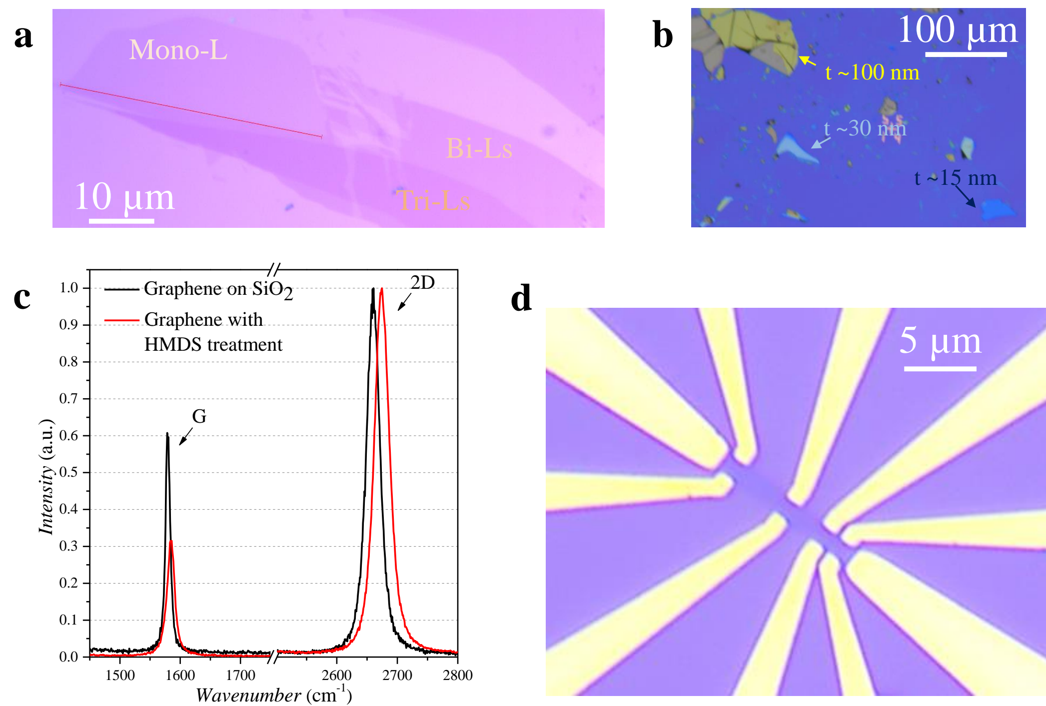

FIGURE 3.1: (a) Optical image of mono-bi-tri layer graphene flake. (b) Optical image of graphite with different thickness. (c) Normalized Raman spectra of two flakes of graphene. The black line shows the Raman spectra of a monolayer graphene on Si/SiO_2 substrate and the red line corresponds to a monolayer graphene on Si/SiO_2 substrate with HMDS treatment. (d) Optical image of mono-layer graphene on SiO_2 with Hall Bar configuration.

10 μm and dose of 230 μC/cm^2) we defined a PMMA Hall bar mask for the etching process by reactive ion etching (see section 2.1.5). We used an O_2/ Ar atmosphere (10:30 sccm) at T=20 °C and P=60 mtorr, with a power of 40 W to define the Hall Bar. The devices were then suitable for transport measurements. These devices with HMDS treatment need a second immersion in HMDS solution to improves more the quality of the devices for at least 24 h. A typical device, after the fabrication process, is shown in Figure 3.1(d).

Graphene Nanoconstrictions with HMDS

For the graphene constrictions with HMDS treatment, the fabrication process needs an additional fabrication step.

After the definition of the bar, the definition of the nanoconstrictions (NCs)

was made with a new EBL process and new etching through ICP-RIE[1] in Ar/O_2 atmosphere (same parameters as described in the previous section). For this last EBL process we used PMMA with lower concentration (2%) in chlorobenzene (resist thickness 70 nm). A smaller aperture (7.5 μm with a dose of 175 $\mu C/cm^2$) and a writing field of 100 μm (using closer markers with a separation of 70 μm previously defined in the first EBL) guarantee a higher nominal resolution of 2 nm (for a writing field of 500 μm and aperture of 10 μm, the nominal resolution was 7.8 nm). The final real resolution was so improved because of the EBL parameters and also thanks to the use of a thinner PMMA coating.

In Chapter 5 we will show the device and results of NCs with HMDS treatment.

3.1.2 Hall Bar with graphene on hBN

Firstly, graphene flakes were obtained and characterized as described in the previous sections. HBN flakes had to be subsequently obtained for the fabrication of graphene-hBN based heterostructures.

A Ultra-pure bulk of hBN crystal used for exfoliation was bought from HQ Graphene or obtained by a collaboration with the Reasearch Institute of Electrical Communication (RIEC) at Tohoku University of Sendai (Japan). The exfoliation process was similar to graphene, but for hBN we use only Ultron tape and the peeling occurs on a hot plate at 100 °C after heating the substrate for 1 minute. In this way relative big flakes with a minimum lateral size of 30 μm and a thickness between 10 and 40 μm were obtained with less tape contaminant. The residual contaminant of the tape was definitively removed after a standard cleaning process (acetone and isopropanol) and an annealing at 350 °C in Ar atmosphere.

[1]Before the installation of ICP-RIE we used a plasma cleaner process in Ar and O_2 atmosphere for the etching process. Unfortunately the maximum resolution was around 500 nm, so it was enough for Hall Bar definition but not for NCs definition.

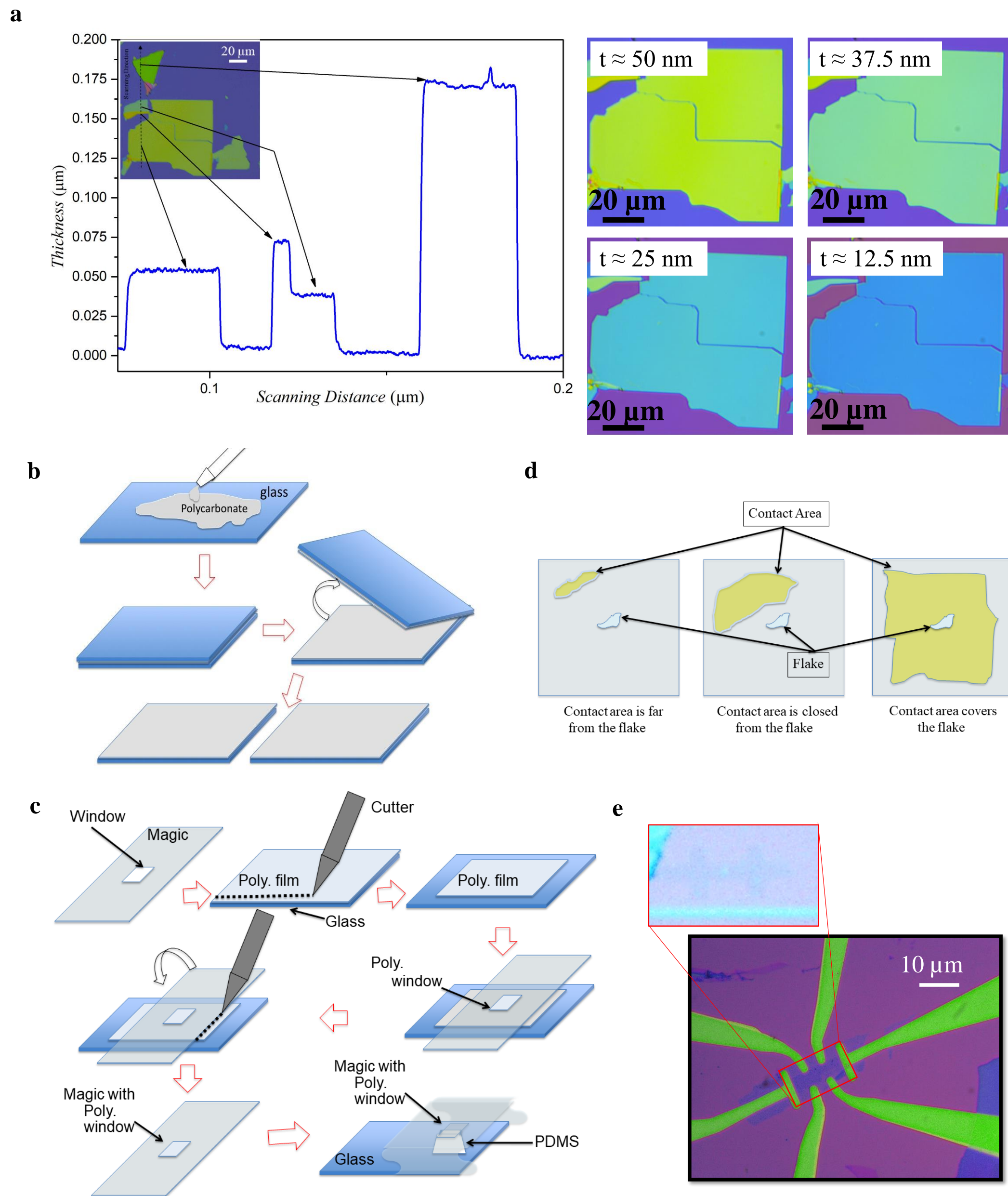

FIGURE 3.2: (a) Left: Profilometer measurement of h-BN flakes with different thickness (Optical Image with the scanning line in the inset). Right: Optical image of a flake of hBN that was etched with ICP-RIE in various steps. The contrast (colour) of the flake changes with the thickness (b) Preparation of the Polycarbonate film. (c) Preparation of PC film on a Magic tape windows and PDMS stamp. (d) Three different possible situations of the contact area during the transfer process. (e) Typical Hall bar of graphene on hBN. In the inset the Hall bar definition of graphene on h-BN before the deposition of the ohmic contacts.

A preliminary characterization was obtained by optical contrast of the hBN flake (dark blue, light blue, green blue, yellow, grey colours can be found by increasing the thickness). Profilometer measurements gave us the accurate information regarding the thickness and quality (roughness) of hBN flakes (see Figure 3.2(a)). After choosing the flakes we placed the graphene flake on hBN with a transfer technique similar to [27] (PC method). Recently a similar technique was used to obtain cleaning interfaces in layered materials heterostructures [36].

The preparation of PC film can be summarized as:

- *Preparation of Polydimethylsiloxane (PDMS) stamp*. A mixture 1:10 of the bicomponent SYLGARD® 184 was placed (after removal of air bubble with various steps of vacuum-vent in a bell jar) in a Petri dish and baked at 75°C for 4-5h.

- *Preparation of the PC film on microscope glass slide*. Using a clean glass slide for microscope we dropped between 250 and 500 μl of PC in chloroform. Then we placed another clean glass on the top. The two glass slides and the PC film form a sandwich (with the PC in the middle). Then removing (as shown in Figure 3.2(b)) the top glass slide, both glass slides are covered with PC film, so both can be used. Finally the PC film is left in air for 15 min. The film is usable for 4-5 h, later the chloroform starts to evaporate and the composition changes, so a new film must be prepared.

- *Sticking PDMS stamp on glass*. Cutting the PDMS stamp with a pyramidal shape and using a Plasma Cleaner process (see section 2.1.10) the bottom side of the pyramid and the surface of a glass side can be functionalized. Subsequently, putting the PDMS pyramid on the glass, they are well sticked. The top PDMS side stamp can be cleaned putting a tape of Ultron adhesive tape and removing it.

- *Preparation of PC film on Magic tape*. Cut a stripe of Magic tape and define (cutting) inside a square hole (window), bigger than the top size of the PDMS stamp, so its sizes would be 2.5*2.5 mm (see first step in Figure 3.2(c)).

  Remove with a cutter the external part of the polycarbonate film on the glass slide, in this way the borders of the film are removed see second and third step in Figure 3.2(c).

  Align and place the window of the Magic tape on the center part of the PC film (fourth step in Figure 3.2c).

  Cut the external part of the PC film and remove gently the Magic tape (fifth step in Figure 3.2c). In this way a polycarbonate film stays in the window previously defined in the Magic tape (sixth step in Figure 3.2c).

- *Placing PC film window on PDMS stamp*. Align the window of PC film on the PDMS stamp. Put in contact PC film and PDMS. The polycarbonate window has to stay higher than the rest of the tape.

Everything is ready for the transfer process. The steps to transfer a graphene flake on hBN flake with the PC method are the following:

- We started to pick up the top flake of the heterostructure (graphene). Using the transfer setup (see section 2.2) we align the flake of graphene on the SiO_2 in the centre of the window of Polycarbonate.

- Move up (z-axis) slowly the wafer, when the Polycarbonate is in contact with the graphene, a "bubble"(contact area beetween PC film and SiO_2) appears. There are three possible situations (see Figure 3.2(d)). If the "bubble"is far from the flake (left in Figure 3.2(d)), moving the tilt stage, the PDMS stamp area can be extended until the flake is closer to the contact area (center in the Figure 3.2(d)). The last situation (right in Figure 3.2d), appears when the contact area completely covers the flake.

- Turn on the heater and increase the temperature at T=50 °C. Under this condition, the contact area is increasing its dimension and covering completely the flake.

- Turn off the heater and wait until room temperature while the contact area decreases its dimensions.

- Moving down the SiO_2 with the z-axis, the graphene flake is on the PC film and PDMS stamp.

- Align the flake of hBN on the SiO_2 with the flake of graphene on PC film.

- Move up the SiO_2 (with the hBN flake) through z-axis until the contact area appears. Control fringes on the PC film with the tilt movement.

- Increase the temperature until 150 °C. Again contact area is increasing during this process.

- Increase T until 170 °C. Move gently down with the z-axis to melt and release the PC film on the SiO_2 substrate. During this process the contact area is reducing (this process has to be not so fast). When the contact area disappears, the PC film with graphene is transferred on hBN on the substrate. Move the repeatedly the(x,y) stage to "break" the borders of the PC film.

- When the borders are broken, gently move down with the z- axis. At the end end of this step, the heterostructure of graphene-hBN is obtained, but it is still covered with polycarbonate.

- Cleave the substrate. This is the best moment because the area with the heterostucture is easily recognizable and the heterostructure is still protected by PC film.

- Remove the polycarbonate in chloroform for 15 minutes. The heterostructure of graphene-hBN is ready and clean to be processed.

We define the Hall Bar through electron beam lithography with PMMA resist and a subsequent etching process by reactive ion etching in O_2 and Ar atmosphere (see inset in Figure 3.2(e)). The evaporation of titanium and gold after a second step of EBL are necessary for the ohmic contacts. The typical prototype of Hall Bar of graphene on hBN is shown in Figure 3.2(e).

3.1.3 Hall Bar with hBN-encapsulated graphene (with option of the graphite backgate) and Nanoconstrictions with encapsulated graphene

In this section a description of the Hall Bar fabrication with encapsulated graphene is reported. Even if the major number of devices based on encapsulated graphene was without the graphite backgate, here we include this option for completeness. In fact it is well known that the use of a graphite backgate can improve the performances of graphene devices [37]. From a fabrication point of view the main difference between the devices based on heterostructures of encapsulated graphene with or without graphite backgate, consists in the transfer process, because for the graphite backgate we fabricated a four layers heterostructure instead of three layers heterostructure. Through the PPC method, it means a longer transfer process in terms of time (typically the double). In fact the graphite backgate devices need particular attention during the fabrication process, since it is very important to avoid short-circuit between ohmic contacts and the graphite backgate.

Besides the exfoliation of monolayer graphene and hBN (top and botton), we also need to exfoliate graphite to obtain a thin layer graphite (few graphene layers). The graphite thickness should be between 10-25 nm. it is chosen according homogeneity and optical contrast (light blue tending to

dark blue) and it is also characterized by profilometer. A particular attention in the choice of the bottom hBN flake is requested [38] because the thickness should be around 35-40 nm and well measured to avoid problem during the etching process (avoiding short-circuited graphite with ohmic contacts). Once the four flakes are chosen and measured, the transfer process can take place. As mentioned above, for heterostructure with more than 2 flakes we used a transfer technique similar to [29].

Firstly the preparation of PPC film is necessary. This process is faster and more controllable than the preparation of PC film. After its preparation, PPC film on PDMS can be also used as stamp for longer time (typically 1 week):

- *Preparation of the PDMS stamp with the PPC film.* A square piece of 0.8 cm^2 of PDMS is cutted and placed in a glass slide. The surface of the PDMS stamp is functionalised in an atmosphere of O_2 through ICP-RIE (see section 2.1.5). A solution of polypropilene previously dissolved in anisole (concentration of 9%) is spinned on the PDMS stamp and baked for 15 minutes at 100 °C in vacuum.

- *Placing the PPC film and PDMS stamp on a glass slide.* A small piece (9 mm^2) of PDMS and PPC stamp is cutted and sticked with transparent glue on a glass slide.

Everything is ready for the transfer process. The first step consists in obtaining a heterostucture of hBN (bottom) on graphite:

- Pick up of the hBN (bottom flake). The stamp is placed over the Si/SiO_2 substrate with the bottom hBN and by using the micrometer stages and the optical microscope, the top hBN flake (Figure 3.3(a) 1A) is located and positioned under the stamp.

- Then, the SiO_2 substrate is approched to the PDMS stamp through the z-movement stage until a contact area appears (Figure 3.3(a) 2A). If the

contact area is too far from the flake, the tilt stage can be used to increase it.

- The temperature of the substrate in increased up to 60 °C and the PPC will extend and cover the whole flake.

- Turning off the heater the SiO_2 substrate is removed with the z-movement allowing to pick up the bottom hBN flake by the stamp. In this step the flake has been transferred on th PPC film (Figure 3.3(a) 3A).

- Then the graphite flake (Figure 3.3(b)) on Si/SiO_2 is aligned with (x,y) stages and approached to the hBN bottom flake until a contact area (between SiO_2 substrate and stamp) appears. Tilt in case the bubble is too far from the flake (4A, 5A in Figure 3.3(a)).

- The top hBN flake is deposited on the graphite flake. The temperature of the substrate with the graphene is increased up to 120 °C which permit to melt the PPC film and enhance the adhesion between graphite and hBN. Therefore, the hBN bottom flake is deposited on the graphene flake reaching the above temperature (Figure 3.3(a) 6A).

The result is a heterostructure of Graphite/hBN on a Si/SiO_2 substrate (see Figure 3.3(b)). The heterostructure was cleaned in anisole, acetone and isopropanol and annealed at 350 °C in Ar with the RTP for 15 minutes to remove the contamination before the next steps of the transfer process.

Same steps can be repeated, obtaining a heterostructure of top hBN flake on graphene.

- Using a new stamp we pick up the top hBN flake from the SiO_2 substrate approaching the PDMS stamp, extending the contact area contact area with the temperature (until 60 °C) and removing the substrate from the stamp through z-movement (Figure 3.4(a) 1B, 2B).

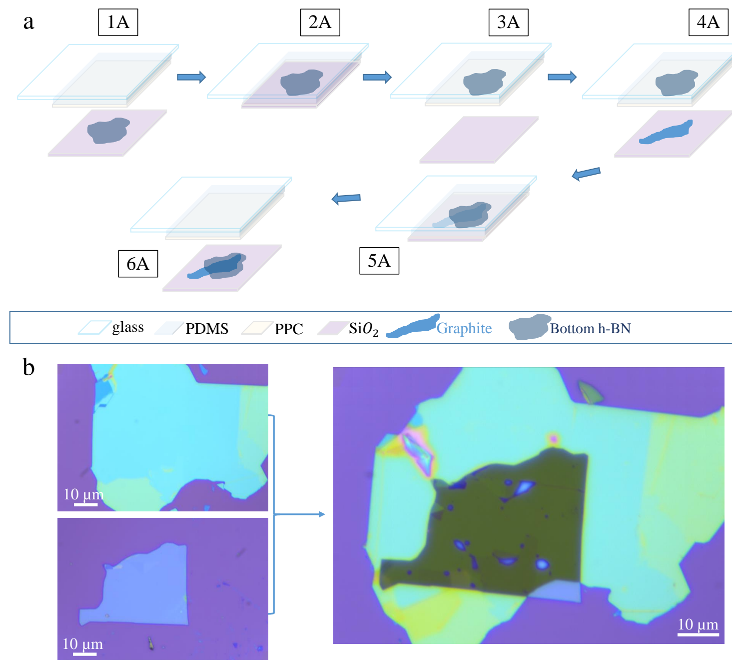

FIGURE 3.3: (a) Transfer step processes for graphite/hBN heterostructure. (b) Optical images of bottom hBN (top left) graphite (bottom left) and their correspondent heterostructure.

- Once the top hBN flake stays on the PPC film (3B in Figure 3.4(a)), we align and approach with (x,y,z) stage the graphene flake on SiO_2 with the top hBN flake (Figure 3.4a 4B).

- After the appearance of the contact area (5A in Figure 3.4(a)), it is increased with the temperature at 150 °C, then through the melting of the PPC film and removing the substrate with z-movement, the top hBN flake is released on the graphene flake (6B in Figure 3.4(a)).

Now the heterostructure of graphene/hBN (top) was obtained and cleaned in anisole, acetone and isopropanol (see Figure 3.4b).

So the heterostructure of graphene/hBN(top) is ready to be picked up and placed on the heterostructure of graphite/hBN (bottom):

- First the pick up of the heterostructure graphene/hBN(top) takes place with a new stamp. Approaching the SiO_2 substrate to the PDMS stamp,

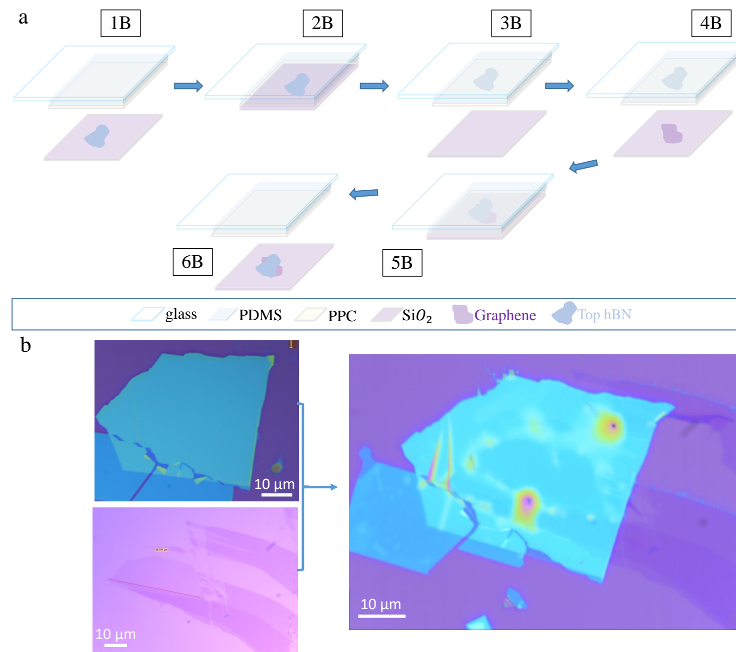

FIGURE 3.4: (a) Transfer step processes for hBN/graphene heterostructure. (b) Optical images of top hBN (top left) graphene (bottom left) and their correspondent heterostructure.

extending the contact area with the temperature (until 60 °C) and removing the substrate from the stamp through z-movement. After this step the heterostructure of graphene/hBN(top) is transferred on the PPC film (1C, 2C, 3C in Figure 3.5(a)).

- Then the align and approach of the heterostructure of graphite/hBN (bottom) on SiO_2 substrate with the heterostucture of graphene/hBN takes place until we obtain a contact area (4C, 5C in Figure 3.5(a)). Increasing the temperature (150 °C), the heterostructure of graphene/hBN (top) is transferred on the heterostucture of graphite/hBN(bottom) (6C in Figure 3.5a).

- The whole heterostructure is so cleaned in anisole, acetone and isopropanol and a rapid process annealing at 350 ° in Ar atmosphere removes contamination and PPC residual from the heterostructure and from the substrate.

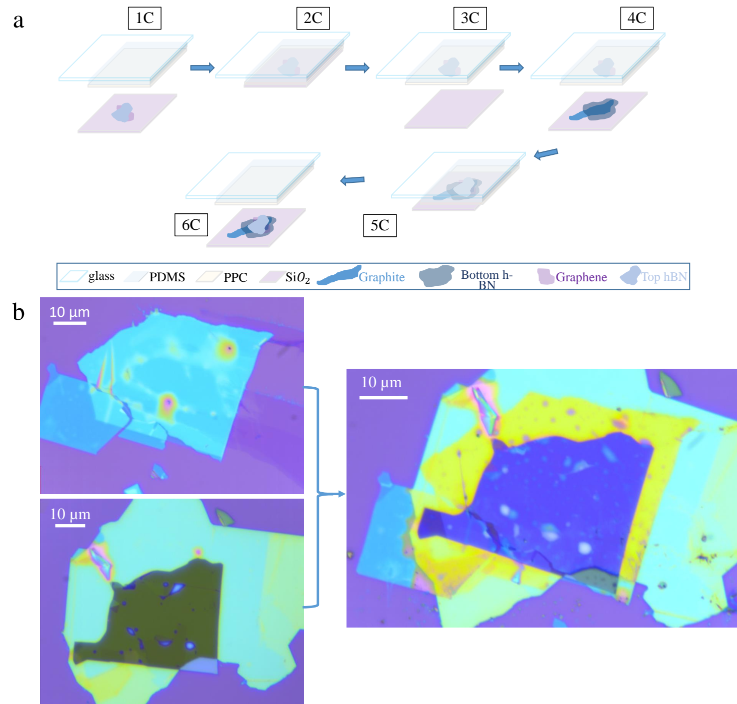

FIGURE 3.5: (a) Transfer last steps for graphite/h-BN/graphene/hBN heterostructure. (b) Optical images of graphene/top hBN (top left) graphite/bottom hBN (bottom left) and the whole heterostructure (right).

Upon completion of all the above steps, the entire vertical graphite/hBN/-Graphene/hBN heterostructure was obtained (Figure 3.5(b)). During this process a lot of blisters or bubble of air were trapped into the heterostructure. It is important to choose areas free of bubbles since it would reduce the quality of the encapsulated graphene. The best area was chosen through optical microscope and Raman spectroscopy. Raman spectra of graphene encapsulated in hBN is different from the Raman spectra of graphene on SiO_2. Figure 3.6a shows the Raman spectrum of the final hBN/graphene/hBN heterostructure on a SiO_2/Si substrate.

An indication of high crystalline quality in graphene is provided by the ratio between the 2D-peak and the G-peak. For example, for graphene on SiO_2 this value can vary from 1 (defected graphene) up to 3-4, [39] and in suspended graphene it is typically 10 [40]. In our heterostructures this ratio is around 10 (see Figure 3.6), larger than the value observed in heterostructures

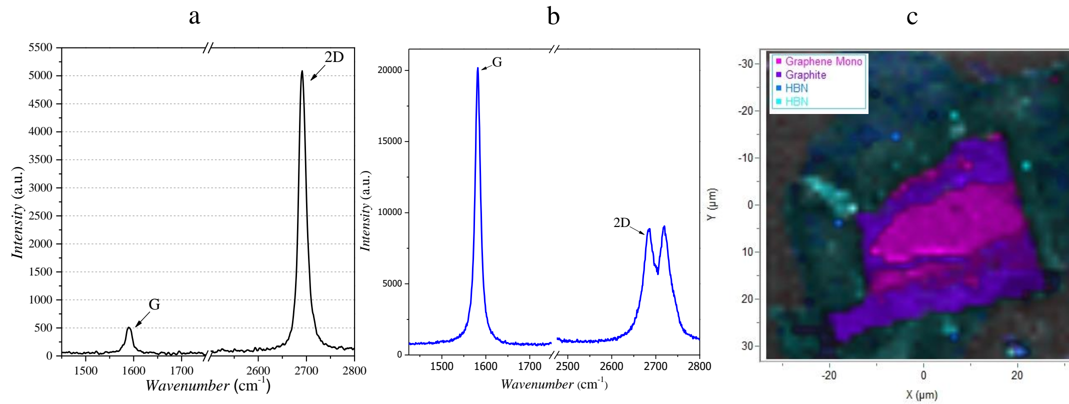

FIGURE 3.6: (a) Raman spectra of the hBN/graphene/hBN heterostructure (b) Raman spectra of the graphite/hBN/graphene/hBN heterostructure (c) MicroRaman Map of the whole heterostructure graphite/hBN/graphene/hBN heterostructure.

obtained with similar methods [29]. Another indication of the high quality of the graphite/hBN/graphene/hBN heterostructure is given by the Full Width Half Maximum (FWHM) of the 2D peak. We found a value close to 18.6 cm^{-1}, while in graphene flakes on Si/SiO_2 substrates is typically above 30 cm^{-1} due structural deformations that broaden the 2D-band [41]. The Raman spectra of graphene encapsulated in hBN with a bottom graphite layer (see 3.6(b)) is more complex due to the presence of the graphite flake that comports the evolution of the 2D peak as a function of number of layers [42]. Unfortunately optical contrast is not useful because graphene is not so clearly visible for the presence of the graphite flake. So in the case of graphite backgate we carried a MicroRaman Map (see Figure 3.6(c)) to identify the best area for the device.

Then the CAD of the Hall bar can be made using ELPHY plus nanolithography software and taking in account the presence of the graphite layer for the definition of the Hall Bar and ohmic contacts.

Through nanolitography we defined the Hall Bar mask and with ICP-RIE we created the "side"contacts in SF_6 atmosphere with an etching rate of 3 nm/s on hBN (see first step in Figure 3.7(a)). In our ICP-RIE recipe we used 40 sccm of SF_6, a power in RIE mode of 75W at 6mtorr of pressure and 10 °C

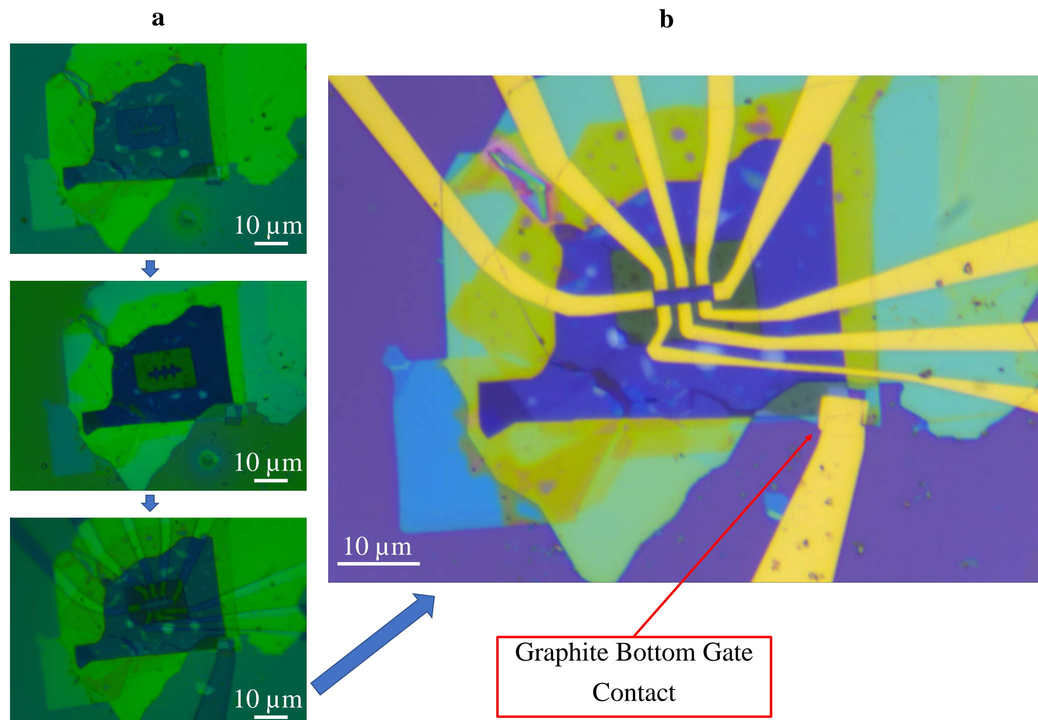

FIGURE 3.7: (a) From the top to the bottom: definition of the Hall Bar through EBL, etching of the Hall Bar through ICP-RIE process, definition of the contacts (and contact for the graphite bottom gate) with a second EBL. (b) Final devices after evaporation of Cr/Au and lift-off process.

of temperature for typically 12 s. A controlled etching rate gives us the possibility to etch only the top hBN flake avoiding the full etching of the bottom hBN (see second step in Figure 3.7(a)). After the etching process, the sample is cleaned in acetone and isopropanol and annealed through RTP process in Ar atmosphere at 350 °C. In this way contamination of the resist and residual bubbles from the heterostructure are removed. In fact it his well known that an annealing (below 500 °C) reduces the number of bubbles encapsulated in the graphene heterostructure [43]. Then, after a new deposition of the PMMA resist, with a new nanolithography process we define the ohmic contacts and the backgate contact (see third step in Figure 3.7a). Finally after an evaporation of Cr (10 nm) and Au (50 nm) and the subsequent lift-off process in acetone, the final sample is ready to be characterized (Figure 3.7(b))

.

Nanoconstrictions fabricated by cryo-ething in encapsulated graphene

After the definition of the bar, a constriction can be defined with a new process of nanolithography and cryo-etching process.

Also in this last EBL process, we used PMMA with lower concentration (2%) in chlorobenzene (resist thickness 70 nm), a smaller aperture (7.5 μm with a dose of 185 μC/cm^2) and a writing field of 100 μm (using closer markers with a separation of 70 μm previously defined in the second EBL). In this way a nominal resolution of 2 nm can be obtained.

It is important to highlight the etching process, because to the best of our knowledge this was the first time in which a cryo-etching method was successful used on graphene.

Whereas cryoetching was widely used in the 1980s to define Si-based structures with high aspect ratio, the appearance of a potentially cheaper method to fabricate such samples, i.e. the Bosch process where no liquid nitrogen was involved, made cryoetching to be forgotten. Besides, to our knowledge, cryo-etching was never used in the generation of nanostructures based on 2D materials.

We introduce for the first time a cryo-etching step to define graphene-based nanoconstrictions tailored using a commercial ICP-RIE (PlasmaPro 100 Cobra system). Such system is equipped with a cryogenic module that enables an operational temperature down to $-120\,^{\circ}$C, ideal to perform cryo-etching. Figure 3.8 shows the SEM images of a NCs etched on hBN with the cryo-etching technique (magnification of 450k) (a) and at room temperatures (magnification of 300k) (b). The upper panels display the original SEM micrographs while the lower part coloured SEM images that help to visualize the borders of the constrictions. The higher roughness of the second image is evident at the edges, in comparison with the very well defined cryo-etched structure.

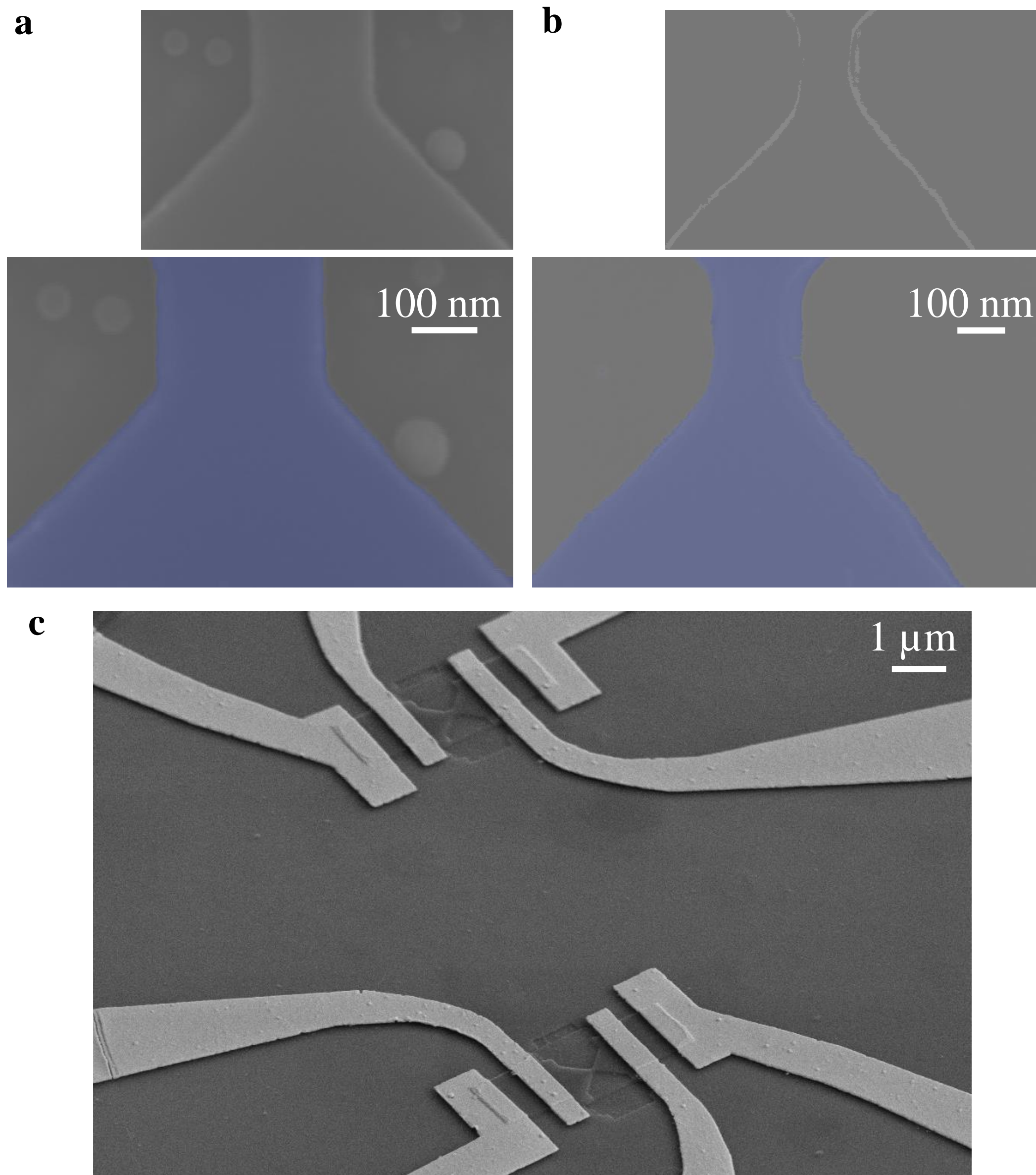

FIGURE 3.8: (a) SEM image of a NC etched by our cryo-etching process. Three bubbles appear in the image, they are blister of air trapped into the original heterostructures and in this case they are transferred to the substrate after the etching process (so they do not affect the device). (b) SEM image of a NC on hBN etched with a standard ICP-RIE procedure. The upper panel of each column shows the original SEM images in grey scale and the lower panels display the coloured ones. (c) Tilted SEM image of typical devices with NCs in encapsulated graphene

Two devices are shown in the SEM image of Figure 3.8(c), where are defined two different nanoconstrictions, the upper one has a width of $w \approx 200nm$, the lower one has a width of $w \approx 100nm$.

3.1.4 FETs detectors based on encapsulated graphene

Thanks to its high carrier mobility, frequency-independent absorption, gapless or controllable gap according the number of layers (monolayer or bilayer) graphene is a very interesting material for the development of detectors working in the terahertz region of the electromagnetic spectrum, still severely lacking in terms of solid-state devices. Here we describe the fabrication process of terahertz detectors based on antenna-coupled graphene field-effect transistors, using encapsulated high mobility and high stability graphene [44] instead of graphene on silicon oxide [7].

Starting from the heterostucture of hBN-graphene-hBN obtained by the transfer method (step 1 in Figure 3.9), the fabrication process of FETs in encapsulated graphene can be divided in three different steps; Bar definition, fabrication of the external contacts and top gates.

For the bar definition, a nanolithography and etching process similar to the Hall Bar definition was carried out. After the deposition of the resist (PMMA with a concentration at 4% in chlorobenzene, baking at 160° for 10 minutes) the bar is defined by means lithography process (step 2 in Figure 3.9) and etched with ICP-RIE in SF_6 atmosphere (step 3 in Figure 3.9).

The "side"contacts were fabricated after an annealing in Ar atmosphere at 350 °C, through a second nanolithography process (step 4 in Figure 3.9) and subsequent evaporation of Cr/Au (5-40 nm) and lift off process (step 5 in Figure 3.9).

Before the definition of the top gates it is necessary to cover the device with a dielectric film. In our Clean room we do not have an equipment (i.e.

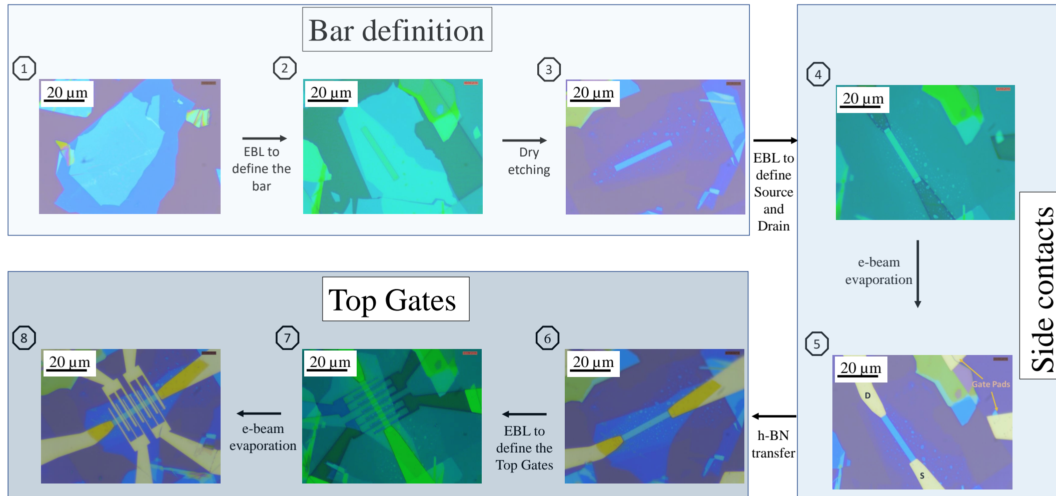

FIGURE 3.9: Fabrication process of FETs in encapsulated graphene can be divided in three different steps; Bar definition, fabrication of the external contacts and top gates.

atomic layer deposition, sputtering etc.) for dielectric deposition. For this reason we transferred a flake of hBN on the device (step 6 in Figure 3.9). The gates were defined by another EBL process (step 7 in Figure 3.9) and evaporation and lift-off of Cr/Au (5/40 nm) (step 8 in Figure 3.9). The final device ADGG-GFET (asymmetrical dual grating gate FET based on graphene) is shown in the step 8 of Figure 3.9. A multi-finger dual-gate topology greatly improves considerably the performance of THz detectors based on plasma-waves, as demonstrated theoretically and experimentally [45]. The use of asymmetric fingers FETs based on graphene instead of a large antenna tuned for THz frequency has a technological advantage respect a conventional antenna [46] in terms of space.

3.2 Epitaxial graphene and CVD graphene devices

Even if mechanical exfoliation continues to give graphene flakes with the best properties (sush as the carrier mobility), epitaxial growth [47] and Chemical Vapour Deposition (CVD) [48] are postulated as a very good methods to produce graphene in industrial scale. In this section we describe the fabrication

processes of devices based on epitaxial graphene, grown by GPNT and CVD graphene, grown by Graphenea.

3.2.1 Hall bar with epitaxial graphene with the option of gate voltage

Epitaxial graphene was grown from a substrate of Silicon Carbide (SiC). This material has a wide bandgap semiconductor (2.3-3.3 eV), with incredible properties: high breakdown electric field, good thermal conductivity etc.

Graphitization [47] takes place via the sublimation of Si atoms from the substrate at high temperatures (>1500°C) leaving behind the carbon atoms, due to the fact that the vapor pressure of carbon is negligible compared to the one of silicon.

Graphene is growth in terraces. The devices are fabricated after the selection of the best terrace though optical microscope and Raman spectroscopy.

We found some problems of lift off for the deposition of gold metal for Pads and contacts due the poor adhesion of metal on graphene. For this reason it is necessary to define the graphene bar and to remove the major part of graphene under the Pads and contacts before their definition and evaporation. Another complication is due to the lack of markers on the substrate, in which the graphene is almost not visible with optical microscope.

FIGURE 3.10: Fabrication process of Hall Bar on epitaxial graphene. (a) Optical image of the Bar definition and removal of graphene under pads and contacts. (b) Optical image contacts definition. (c) SEM image of the device after contacts and Pads deposition.

The nanofabrication process for the Hall Bar in epitaxial graphene was the following:

- Deposition of resist (ARP679.04), (4000 rpm) and bake at 170 °C for 5 min.
- First nanolithography for definition of crosslinked markers in the resist (with an high dose of 6000 μC/cm^2, aperture of 10 μm, fast developing of 30 sec in AR60056 and then isopropanol for 20 sec).
- Cad modification according the new markers and the terrace.
- Second nanolithography for definition of the bar and removal of graphene under pads and contacts (dose of 230 μC/cm^2, apertures of 10 and 60 μm, developing for 2 min in AR60056 and stop in isopropanol for 20 s). Figure 3.10(a) shows the optical image of the lithography performed on the epitaxial graphene.
- Dry etching process with ICP-RIE (O_2 and Ar atmosphere (10:30 sccm) at T=20 °C and P=60mtorr, P=40W). Finally cleaning in acetone and isopropanol.
- Second deposition of resist (ARP679.04) (1500 rpm and 500 rpm/s) and bake at 170 °C for 5 min.
- Third nanolithography for definition of new markers in the resist (dose of 230 μC/cm^2, aperture of 10 μm, fast developing of 30 sec in AR60056 and then isopropanol for 20 sec).
- Definition of the contacts and Pads through a fourth nanolithography (dose of 300 μC/cm^2 for contacts and 500 μC/cm^2 for Pads, aperture of 10 and 60 μm respectively, developing of 120 sec in AR60056 and then isopropanol for 20 sec). Figure 3.10(b) shows the optical image of the contacts and pads defined by e-beam lithography.

- Evaporation of Ti and Au (10 and 40 nm) for the fabrication of the ohmic contacts and lift-off in acetone.

The final device is shown in the SEM image of Figure 3.10(c).

Definition of gate voltage on epitaxial graphene

Controlling the carrier concentration in graphene devices is a very important capability of the graphene-based devices as promising candidates to complement semiconductors in the future generations of microelectronic devices. The SiC substrate presents a limitation due to its intrinsic electrical properties, in fact its insulator nature comports the inability to control the carrier density in situ. A complicate implantation is necessary to obtain a conductive substrate with epitaxial graphene and so a bottom gated epitaxial graphene device [49][50]. Alternatively carrier density control can be achieved by top-gate techniques, but the common dielectric films (SiO_2[51], SiN[52], Al_2O_3 [53]) modify the epitaxial graphene properties. HBN represents a solution to the inconvenience created by dielectric film. In fact it was proven that the electronic properties of graphene, such as the Dirac cone, remain intact and no significant charge transfer i.e. doping, is observed [54]. For this reason we fabricated Hall Bar on epitaxial graphene using hBN as dielectric film. After the Hall bar definition (see Figure 3.11a), the fabrication process was the following:

- Transfer (exfoliation, pick up and release) of hBN flake on the Hall bar as dielectric film. The transfer method was made with PPC film as explained in section 3.1.3 (see Figure 3.11b).

- Cleaning in acetone and isopropanol and annealing at 350° C in Ar atmosphere.

- Nanolithography and evaporation of Ti and Au for the gate definition.

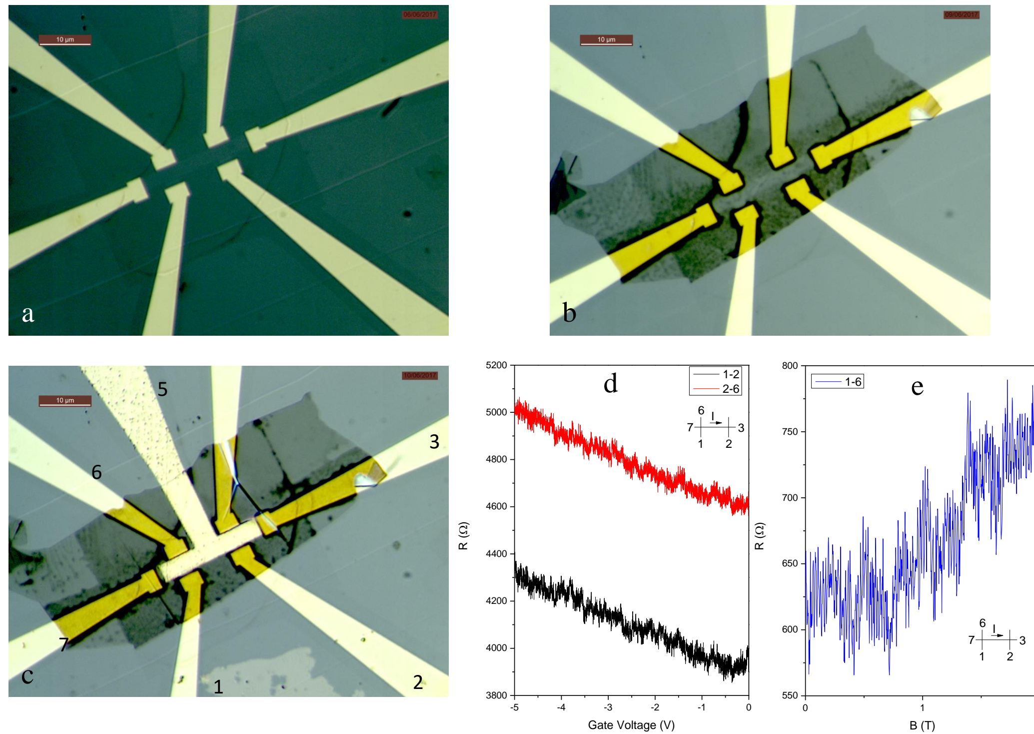

FIGURE 3.11: (a) Optical image of the Hall Bar on epitaxial graphene. (b) Transfer of a hBN flake on the epitaxial Hall Bar. (c) Optical image of the final device, top-gated Hall Bar with hBN as dielectric film. (d) Longitudinal resistance (black line) and quasi longitudinal resistance (red line) in function of top gate voltage (V_g) at room temperature. (e) Transversal resistance versus magnetic field (B) at room temperature

The final device is shown in Figure 3.11(c). Figure 3.11(d) and (e) shows the electrical characterization at room temperature of the device. Figure 3.11(d) shows the resistance as the function of the top gate voltage (black line for pure longitudinal resistance, quasi longitudinal resistance in red line), demonstrating the possibility to control in situ the charge carriers using a top gate and hBN dielectric film for the first time to the best of our knowledgment. The transversal resistance versus the magnetic field is reported in Figure 3.11(e). The measurement configurations are shown in the schematic inset of Figures 3.11 (d) and (e).

3.2.2 CVD graphene devices

Chemical vapour deposition (CVD) graphene consists in the growth of graphene on single crystalline transition metals such as Co, Pt, Ir, Ru, and Ni [55][56]. The nucleation and growth of graphene usually occurs by exposure of the transition metal surface to a hydrocarbon gas under low pressure or Ultra High Vacuum (UHV) conditions and a typical temperature at T>900 °C. The process gives rise to an ultrathin graphene film (1 to less then 10 layers) over the transition metal surface disposed in domains. The transfer of the CVD-graphene films to a different substrate is typically enabled by various wet and dry transfer [57].

We fabricated Pads on CVD graphene transferred on quartz for large scale characterization though 4-probes measurements.

Due to the big size of the pads we used a photolitography through MBJ4 mask aligner (see section 2.1.6) for their definition. We used PMMA as photoresist [58], because conventional optical resists (as well as their developer) result too aggressive for graphene. The fabrication process was:

- Coating PMMA (4000 rpm) and bake at 170 ° C for 5 min the sample
- Align the sample under the optical mask and exposure for 16 min the PMMA film
- Developing in MIBK:IPA (1:1) (2 min) and stopping in isopropanol for 20 s. The pads are defined in the sample (see Figure 3.12(a))
- Evaporation of Ti (5 nm) and Au (50 nm)
- Soft lift off in acetone; since the adhesion of metal on graphene is poor.

Figure 3.12(b) shows a pad of 1 mm* 1 mm and Figure 3.12(c) shows the whole sample. In both Figures it is evident the problem with the lift off process due to the poor adhesion of metals on graphene.

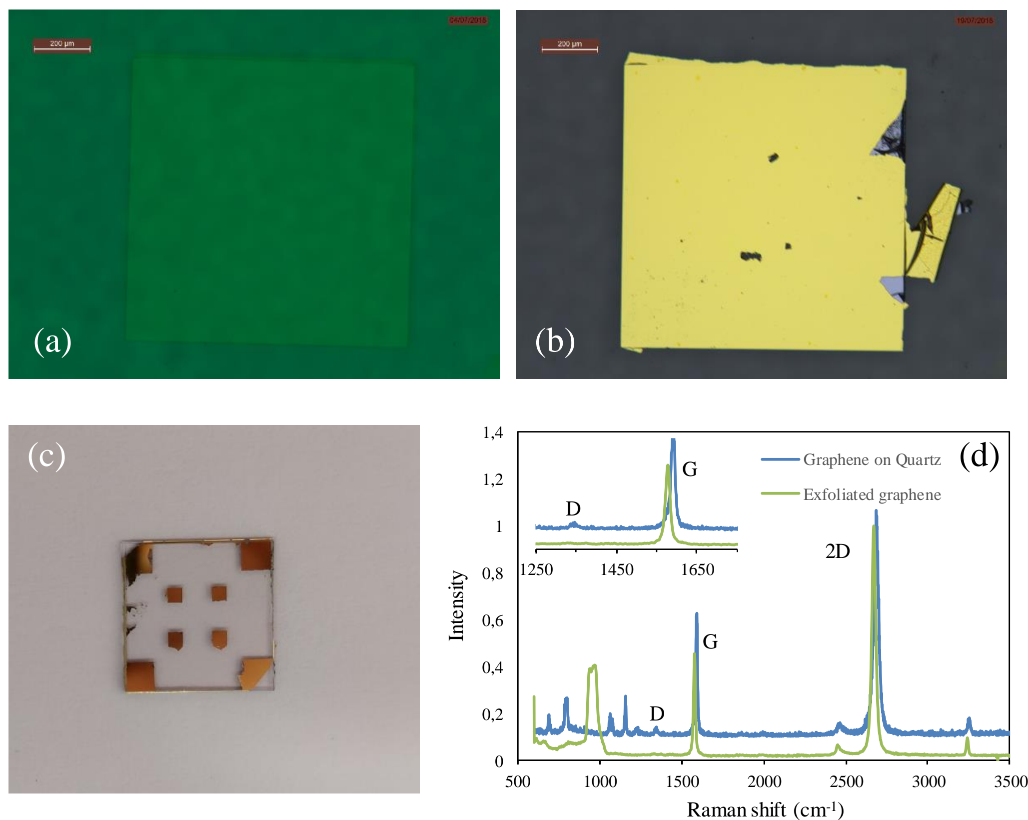

FIGURE 3.12: (a) Optical image of the Pad after developing. (b) Optical image of the Pad after evaporation and lift off. (c) All the Pads on CVD graphene transferred on quartz. (d) Comparison between the Raman spectra of exfoliated graphene (green line) and CVD graphene (blue line).

Figure 3.12(d) shows the comparison between the Raman spectra of exfoliated graphene (green line) and CVD graphene (blue line). The ratio between 2D peak and G peak is almost the same, indicating the high quality of the CVD graphene, even if more defects are present as demonstrate from the D peak in the inset of the same graph.

3.3 $MoSe_2$ and $MoTe_2$ devices

In 2005 Novoselov et al. [59] demonstrated that, apart of graphene, it is possible to obtain other 2D materials (hBN, MoS_2, $NbSe_2$, $Bi_2Sr_2CaCu_2O_x$) by exfoliation. They are named 2D materials so to put in evidence their very small thickness in comparison with the other two dimensions, starting from

the bulk three dimensional material through mechanical exfoliation. This is possible because there are layered materials with strong in-plane bonds and weak, van der Waals-like coupling between layers. Transition metal dichalcogenide materials (TMDs) attracted particular interest among the 2D materials. They are thin semiconductors composed by transition metal atom (M) and chalcogen atom (X) [60]. In this section we describe the fabrication and preliminary characterization of $MoSe_2$ and $MoTe_2$. They have a direct band gap between 1 and 2 eV and represent excellent candidates for application in electronics and optics.

3.3.1 $MoSe_2$ devices

We started with the mechanical exfoliation of the material from the bulk material (grown by HQ Graphene). The bulk material was firstly pealed with Magic tape and later transferred in the blue tape, where we peeled 5-6 times before placing the blue tape on a SiO_2 substrate (it was previously cleaned in acetone and isopropanol and treated with Plasma cleaner for 5 min). The flake is obtained and identified by optical microscope (inset in Figure 3.13(a)) and a first characterization was made by profilometer (Figure 3.13(a)), before the Raman measurements (Figure 3.13(b)). For example for the flake of the inset of Figure 3.13(a), the measured thickness was 5 nm and considering the thickness of a monolayer flake (9.5 Å), we can estimate a 5-layers $MoSe_2$ flake. This was confirmed by Raman spectroscopy, comparing another 5 nm flake in literature [61] with whom we found a lot of analogies. There is a prominent A_{1G} peak on the material also in bulk as well as other peaks (E_{1G}, E^1_{2G}, B^1_{2G}). We tried to transfer with the PPC method this flake on preppatterned contacts but the flake was damaged as visible in Figure 3.13(c). The device electrically worked but we noticed it was instable. For this reason we changed the fabrication method on another 4L-$MoSe_2$ flake. In this case we

used EBL on ARP67904 (coating at 4000 rpm, bake 160 °C for 10 min) and evaporation of Ti and Au (5 nm and 35 nm). The final device is shown in Figure 3.13(d).

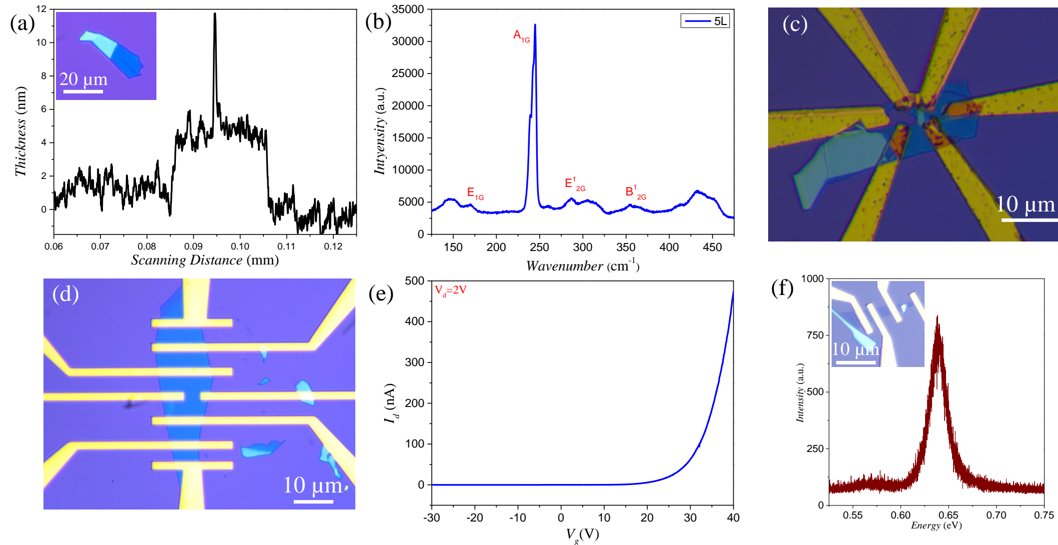

FIGURE 3.13: (a) Profilometer of the blue colour flake. It had a thickness around 5 nm. Inset: Optical image a flake of $MoSe_2$. (b) Raman spectra of the flake (c) Transfer of the flake on a prepatterned device (d) Another device with a $MoSe_2$ flake of 4 nm (e) Drain current as a function of gate voltage with fixed drain voltage (2V) (f) Photoluminescence PL measurement of the monolayer flake with MicroRaman. Inset: Optical image of monolayer $MoSe_2$ device.

We measured the drain current as a function of the gate voltage from -30V to 40 V at fixed drain voltage (V_d=2V)(Figure 3.12(e)) and the behaviour of the current is typical of a n-type semiconductor, as expected [62].

We fabricated also a 1L-$MoSe_2$ device (shown in Figure 3.13(f)) but it did not work probably due oxidation. We estimated the gap with Photoluminescence PL measurement through Raman, as shown in Figure 3.13(h). The measured gap was 1.57 eV [63].

3.3.2 $MoTe_2$ devices

The mechanical exfoliation of $MoTe_2$ is similar to the $MoSe_2$ material. The only difference consists in peeling 3/4 times with the Magic tape and placing

a stripe of the blue tape and peeling only once the blue tape. In fact this material results harder to be exfoliated.

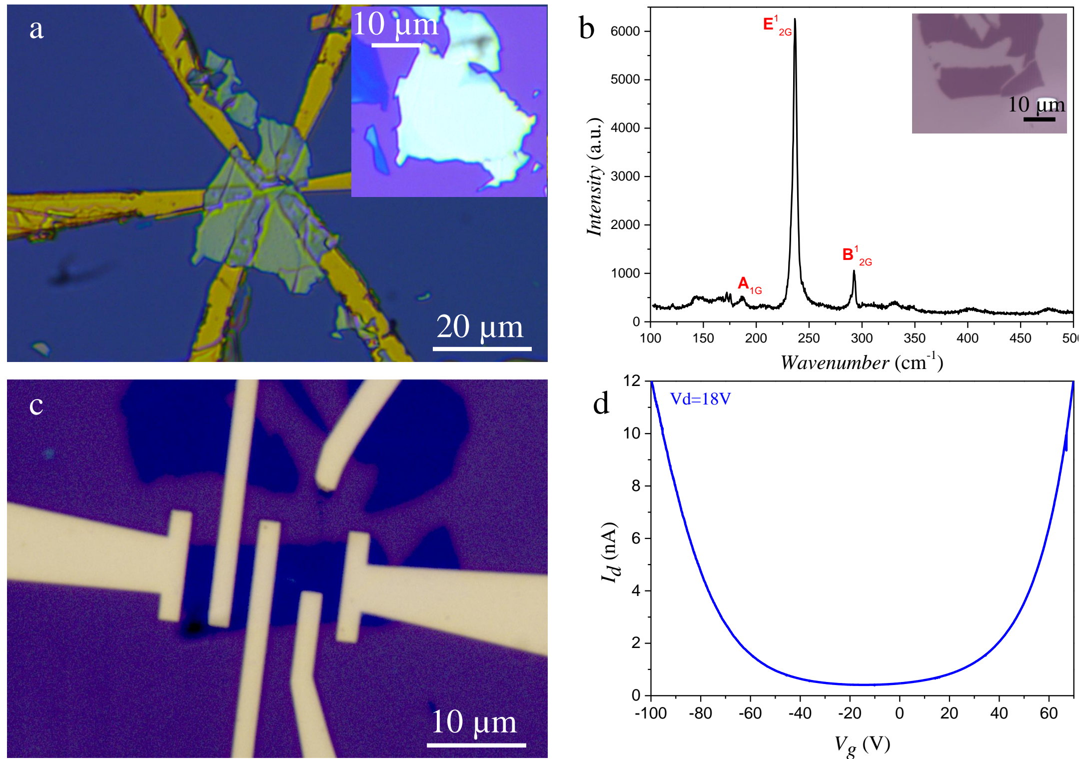

FIGURE 3.14: (a) Optical image a flake of $MoTe_2$ (inset of Figure 3.14a) transferred on prepatterned contacts (Figure 3.14a). (b) Raman spectra of a 5L-$MoTe_2$ (c) device with a 5L-$MoTe_2$ flake (f) Drain current as a function of gate voltage with fixed drain voltage (18V) of 5L-$MoTe_2$.

Also in this case we tried to transfer a flake with a thickness of approximately 20 nm (Optical image in the inset of Figure 3.14(a)) on prepatterned contacts. The transfer process was successful as shown in Figure 3.14(a), but also in this case the measurement was not stable.

For this reason we fabricated another device with the same fabrication process described in the previous section. In this case the flake was a 5-layers flake (Optical image in the inset of Figure 3.14(b)). It was confirmed by Raman spectra in Figure 3.14(b), in fact the ratio between the characteristic peaks B^1_{2G} and E^1_{2G} was around 0.17 [64]. After the EBL process, evaporation of Ti and Au (5 nm and 35 nm) and lift-off, the final device is shown in Figure 3.14(c) (one contact was broken during the lift-off process). A preliminary

measurement of the drain current (I_d) as a function of the gate voltage (V_g) at fixed drain voltage (V_d=18 V) shows the characteristic ambipolar behaviour of this material [65].

Chapter 4

Quantum Hall Effect at high temperatures

In this chapter we present the study of Quantum Hall effect up to room temperature on sample with different substrates and the fractional Hall effect in encapsulated graphene samples.

4.1 Quantum Hall Effect up room temperature in graphene

Quantum Hall Effect (QHE) is a phenomenon observed in a bidimensional conductor subjected to a perpendicular magnetic field that splits the constant density of states into discrete Landau levels (LLs)[66]. In a real sample only the extended states contribute to the conduction. The characteristic quantized Hall conductance (Ne^2/h, with N integer number, e the electron charge, h the Planck constant), appears when the Fermi level E_F lies into the gap (Δ) of localized states between two LLs. Therefore, the disorder potential plays a fundamental role in the observation of the QHE. QHE was primarily observed in different kinds of semiconductor heterostructures at very low temperatures, however, more recently, QHE was observed in graphene [67], in

which the band structure is characterized by a linear energy momentum relation and under magnetic field, a quantization $E_N = \nu_F \sqrt{e\hbar BN}$ is observed (ν_F the Fermi velocity, is the reduced Planck constant, B the magnetic field and N the LL). Graphene is the first and unique Dirac material in which QHE was measured at room temperature [4] and it still represents the best candidate for detailed study of QHE at high temperatures (HT). In comparison with other Dirac material (i.e. HgTe quantum wells [68]) graphene has a high Fermi velocity and a very large energy gap between the lowest LLs N=0 and N=1, almost one order of magnitude larger than the thermal energy at RT. Besides its high carrier concentration helps to fully populate the lowest Landau level even in High Magnetic Field (HMF) and the high mobility (μ) entails a large scattering time, that is almost not affected by changing the temperature so the quantization criterion $\omega_c \tau = \mu B \gg 1$ (with ω_c is the cyclotron frequency, τ the scattering time) is maintained at HT and HMF. Until now, the mechanisms of localization of charge carriers, due to long range potentials (impurities, dislocations etc.) and/or short range potential (adatoms, vacancies), are not completely understood in single layer graphene at HT. The aim of this section consists in addressing this problem in a detailed study of the QHE in single layer graphene at HT. For this aim we measured six h-BN encapsulated graphene samples (HBUN04, HBUN05, HBUN06, HBUN13, HBUN14, HBUN15) and for comparison only one graphene sample on SiO_2 (HBUN12). We focused the attention on the encapsulated devices since in the last sample the results are very similar to the work of Novoselov et al.[4].

High Temperature and density carrier dependence

Applying a gate voltage we are able to to tune the carrier density from hole to electron side through the charge neutrality point (CNP). This capability of graphene devices on insulating substrate is unique and it gives a lot of

information on the quality of the graphene device and its behaviour (i.e. mobility). In Figure 4.1(a) is shown the optical image of a typical device studied in this Chapter. We report the study of the longitudinal resistivity in function of the normalized gate voltage at high temperatures from 125K to 283K (Figure 4.1(b)). We normalized the gate voltage but for encapsulated graphene

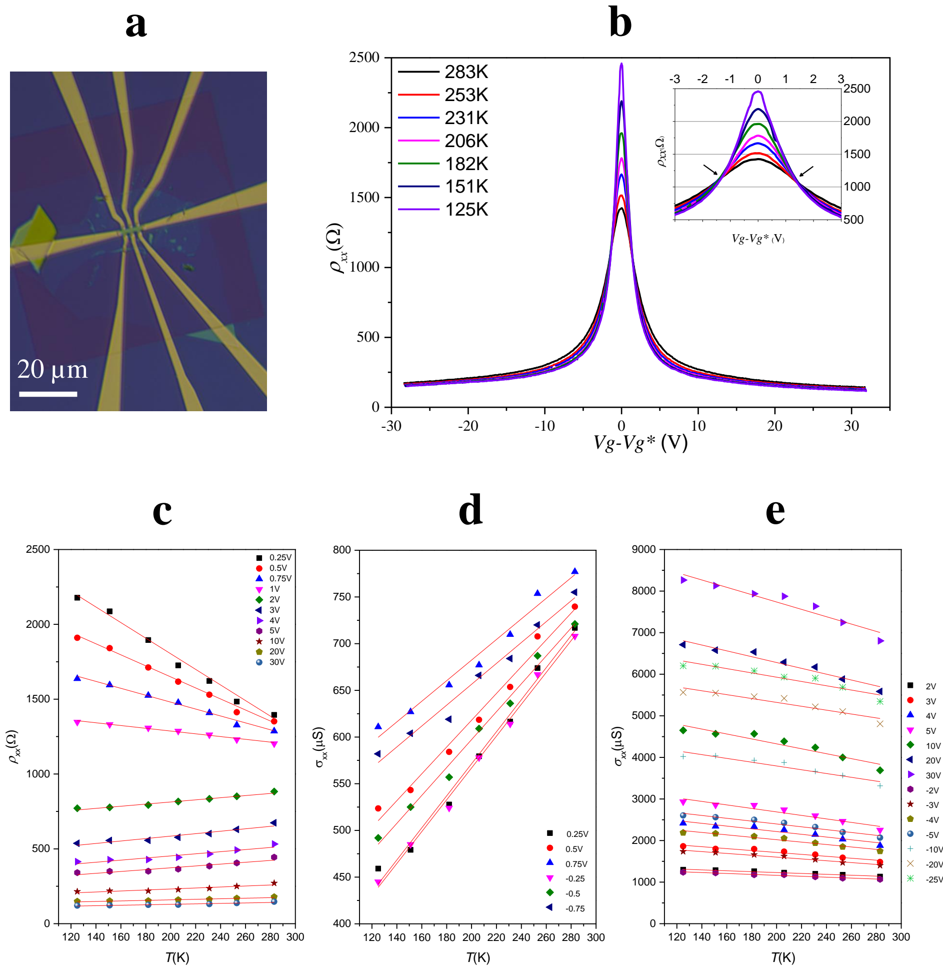

FIGURE 4.1: (a) Optical Image of encapsulated graphene Hall Bar. (b) Longitudinal resistivity versus normalized gate voltage for different temperatures. (c) Longitudinal Resistivity temperature dependence for different valued of gate voltage. (d) Longitudinal conductance temperature dependence for gate voltage values close the CNP. (e) Longitudinal conductance temperature dependence for gate voltage values far from the CNP.

the Dirac point is located very closed to the zero voltage (less than 2V). As expected the longitudinal resistivity at the CNP decreases with the temperature. These measurements refer to the sample HBUN15. In this sample we

can notice a temperature independent crossing point ($V_g - V_g^* \approx \pm 1.33V$, that corresponds to a carrier density of $n = n_c \approx 8.65 * 10^{10} cm^{-2}$) as indicated by the black arrows in the inset of Figure 4.1(b). This crossing point ($n = n_c$) defines two regions. Closed to the Dirac point ($n < n_c$) a no-metallic behaviour ($\frac{d\rho_{xx}}{dT} < 0$) dominates the transport. Further away from the Dirac point ($n > n_c$) a metallic behaviour ($\frac{d\rho_{xx}}{dT} > 0$) is measured. In Figure 4.1(c) we plot the resitivity values at different gate voltage for all the high temperatures studied. From the linear behaviour of the resistivity we can notice that a change of sign in the slope appears passing through the crossing point. We report only the electron side because the hole side has the same trend. In Figure 4.1(d)(e) the longitudinal conductance in μS unit is reported for different temperatures and for values of the gate voltage close (d) or far (e) the CNP. The longitudinal conductance is calculated in conventional way as $\sigma_{xx} = \frac{\rho_{xx}}{(\rho_{xx})^2 + (\rho_{xy})^2}$. As expected the slope of the linear fit is positive for the values of voltage close the CNP (Figure 4.1(d)) and negative for the far values of the voltage from the CNP (Figure 4.1(e)). The same trend was observed in all the encapsulated samples, with the no-metallic behaviour more close the CNP for the higher mobility samples, even if without a real presence of the peculiar crossing point observed in HBUN15. Similar behaviour was observed in high mobility suspended monolayer graphene devices [69], where at high density the increament in linear behaviour of $\rho_{xx}(T)$ suggests electron-phonon interaction as the dominant source of carrier scattering [70]. In graphene on hBN devices, this phenomena, as well the high insulator behavior in the CNP at low T, is an indication of clean and high quality graphene devices and it has been attributed to sublattice symmetry breaking [71].

4.1.1 Mobility and random strain fluctuations

We studied the correlation at room temperature between carrier mobility μ and the width of the resistance peak n^* and we found similar results obtained in [72], where the same analysis was made at low temperature. We measured a larger range of mobility, in which the mobility value was obtained through the Field Effect formula. In comparison with the Hall mobility, Field effect formula give us an average mobility, calculated on a large range of carrier density and not only for a particular carrier density n. In any case the carrier mobility estimated as $\mu = \frac{\sigma}{ne}$ with the estimation of n obtained by the Hall mobility gives comparable values.

The carrier mobility was obtained by fitting the resistance in function of the carrier density (Blue line for holes side, red line for electron side), as shown in Figure 4.2(a) according to the following expression [73] [74]:

$$R = R_c + \frac{N_{sq}}{e\mu\sqrt{n_0^2 + n^2}} \quad (4.1)$$

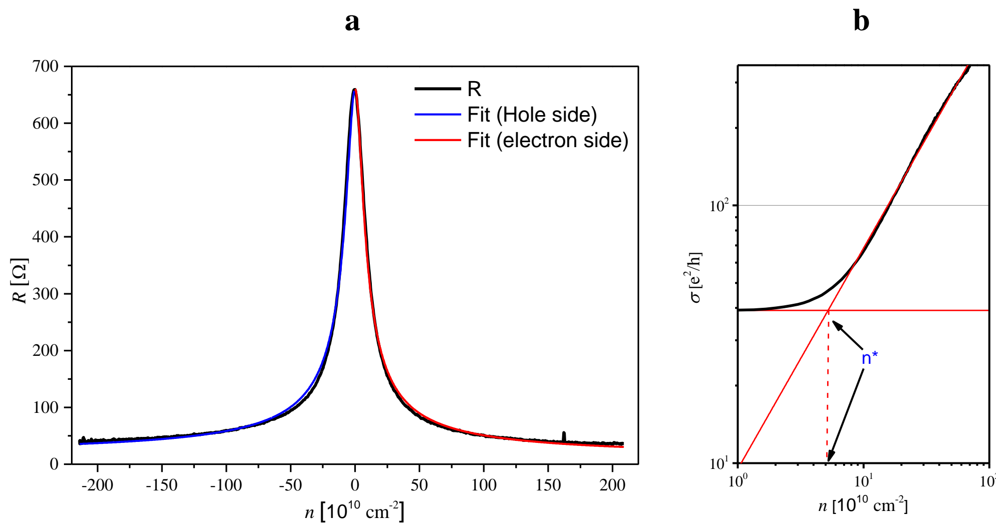

FIGURE 4.2: (a) Resistance (R) versus carrier density n and fit with the field effect formula for hole (blue line) and electron side (red line). (c) Conductivity σ in function of carrier density n in double-logarithmic scale for the extraction of the value n*.

where R_c is the contact resistance, N_{sq} is the number of squares in graphene channel, that is, the length over width ratio, n_0 is the residual doping and μ is the field effect mobility.

The carrier density can be calculated from the gate voltage as:

$$n = \frac{C_{ox}}{e}(V_{bg} - V_{CNP}) \tag{4.2}$$

where e is the elementary charge, $V_{bg}^* = V_{bg} - V_{CNP}$ is the normalized gate voltage, C_{ox} is the capacitance for area of SiO_2 for graphene device on SiO_2 or the total capacitance per area for encapsulated devices ($C_{ox} = \frac{C_{ox}^{SiO_2} C_{ox}^{hBN}}{C_{ox}^{SiO_2} + C_{ox}^{hBN}}$), taking in account the contribution of the SiO$_2$ ($C_{ox}^{SiO_2}$)and the hBN capacitance (C_{ox}^{hBN}) . The mobility of the measured devices varies in a large range, from 1000 $cm^2V^{-1}s^{-1}$ to 150000 $cm^2V^{-1}s^{-1}$ at room temperature. The value of the estimated carrier density fluctuations n^* quantifies the potential fluctuations [75] in the different graphene devices. Its estimation is shown in Figure 4.2(b) from the plot of the conductivity σ versus the carrier concentration n^* in double-logarithmic scale. n^* value is extrapolated from the intersection between the linear behaviour of $log(\sigma)$ and the constant value of $log(\sigma)$ at low density.

If we plot the mobility (μ) in function of n^* (Figure 4.3(a)) for different devices (and both side, electrons and holes), a trend is well defined and it is clear that higher mobility device has a lower value of n^*. The graph in Figure 4.3(b) shown the dependence of $\frac{1}{\mu}$ versus n^*. The two points for lower mobility (on SiO_2 with a mobility lower than 2000 $cm^2V^{-1}s^{-1}$) diverge from the other data, instead if we focus the attention on the higher mobility devices, we found a very linear trend (inset in Figure 4.3(b)). From the fit we obtain a value $\frac{1}{\mu} = (\frac{h}{e})n * \cdot 0.01728$, very closed to the value of 0.018 found in [72]. For the lower mobility devices (not considered in the previous study [72]), there is probably a different dominant disorder mechanism at high temperatures.

In the graph of Figure 4.3(c) we report the minimum of conductivity $\sigma^* = n * e\mu$ calculated from the estimated carrier density fluctuation n^* and mobility as a function of the minimum conductivity. As shown the values are placed around the dashed line of slope 1 and this evidence confirms the validity of the procedure to extract n^* and μ from the experimental data.

The peculiar dependence of mobility with n^*, observed in our analysis, is a proof that in high quality graphene encapsulated in hBN, the random local strain fluctuations in the graphene lattice are the dominant source of disorder also at room temperature. We can so assume that the mobility is limited by intravalley scattering long ranged potentials as founded in [72] also at high temperatures. This disorder is presumably the dominant mechanism for the appearance of QHE in encapsulated graphene, until almost room temperature, as we will show in the next section.

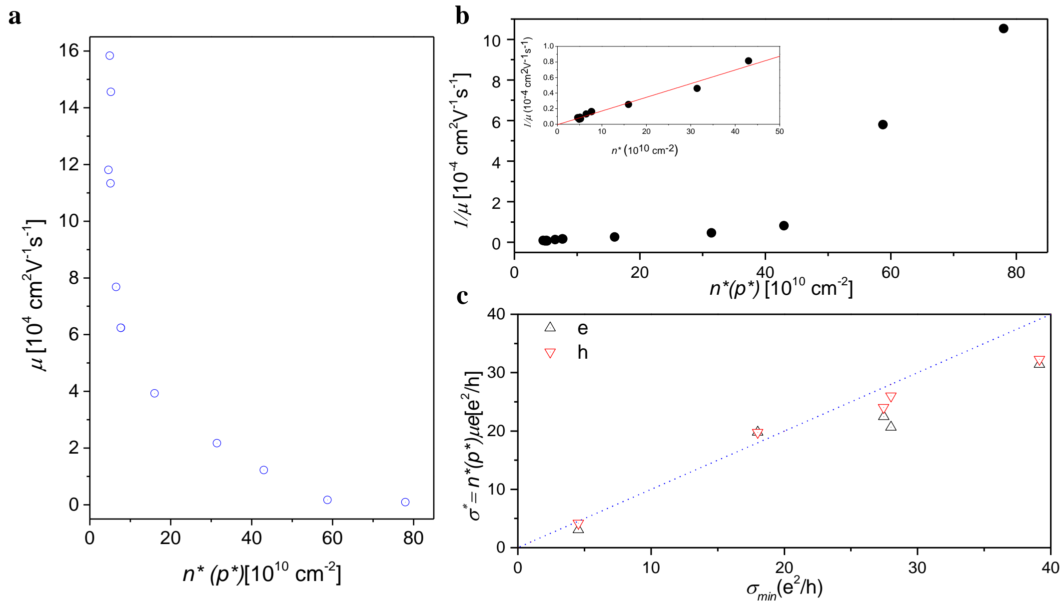

FIGURE 4.3: (a) Mobility (μ) versus the extrapolated value of n^* for different devices. (b) $\frac{1}{\mu}$ versus n^*. In the inset we consider only the higher mobility devices. (c) σ^*, estimated by the carrier density fluctuation, versus σ_{min}, both are in e^2/h unit.

4.1.2 QHE at room temperature

In Figure 4.4(a) the most important result of this chapter is shown.

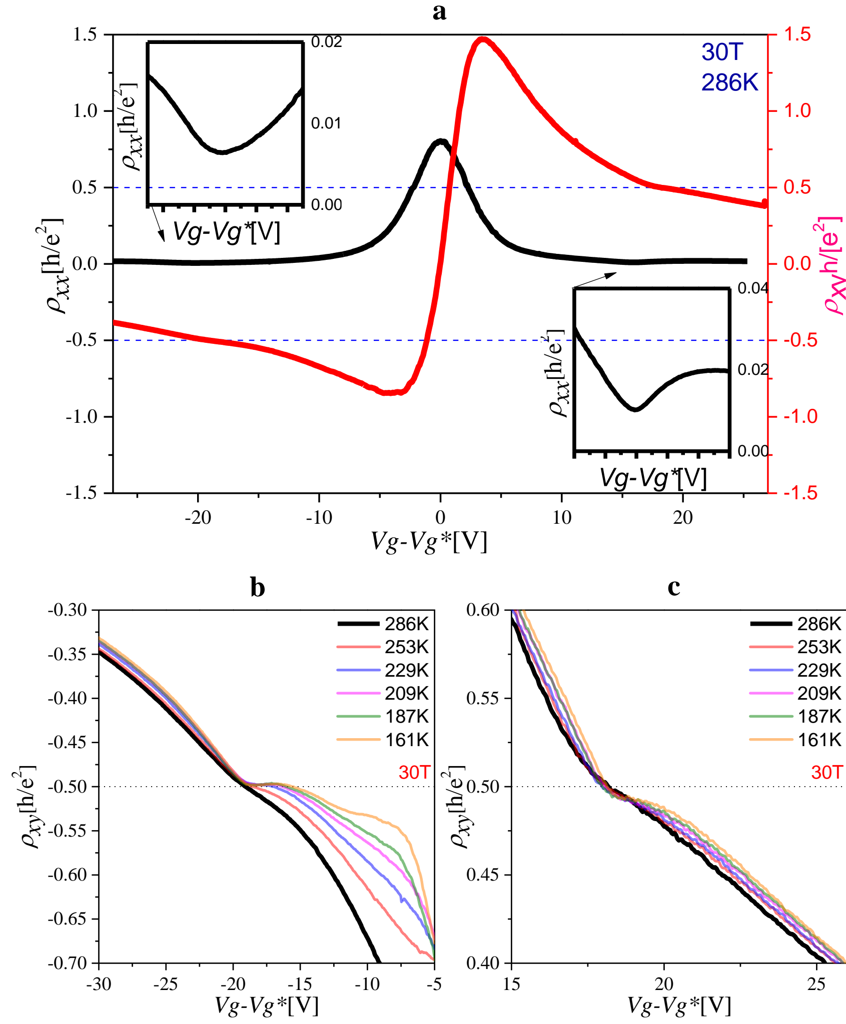

FIGURE 4.4: (a) Longitudinal and transversal resistivity in h/e^2 unit versus normalized gate voltage at room temperature and 30T. In the inset the zoomed longitudinal resistance of the hole side (top-left) and electron side (bottom-right). Zoomed transversal resistance at different temperatures around the filling factor 2 for hole (b) and electron (c) side.

We measured the longitudinal (ρ_{xx}) and trasversal (ρ_{xy}) resistance in the encapsulated graphene (HBUN05) at room temperature (286K) and high magnetic field (30T) sweeping the gate voltage. The result is shown in h/e^2 unit, where ρ_{xx} in black line has two pronounced minimum at the gate voltages $\Delta V \approx -20V$ for the hole side (see inset on the top-left) and $\Delta V \approx +18V$ the electron side (see inset on the bottom-right for major clarity). The values of these minimum are in both cases more than 150 Ω, so one order of magnitude higher than the values found in graphene on SiO_2[4] at similar temperature

and similar perpendicular magnetic field.

The values of ρ_{xy} at the same gate voltages are around $0.5h/e^2$ as expected (see dashed line), but a real quantization is not evident. In Figures 4.4(a) the absence of this quantization at room temperature (black line) is clear if we plot the zoomed transversal resistance at various high temperatures around the value $0.5h/e^2$ for the hole side (b) and electron side (c). The plateau starts to appear clearly only at lower temperature.

Studying other encapsulated samples, we found always less pronounced plateaus at temperatures close to the room temperature. This result strongly differs from the work of Novoselov et al. [4], in which a much lower mobility device showed a clear and very stong quantization at room temperature.

In our lower mobility graphene devices (Figure 4.5(a)) instead we also find a stronger QHE at room temperature as shown in Figure 4.5(a).

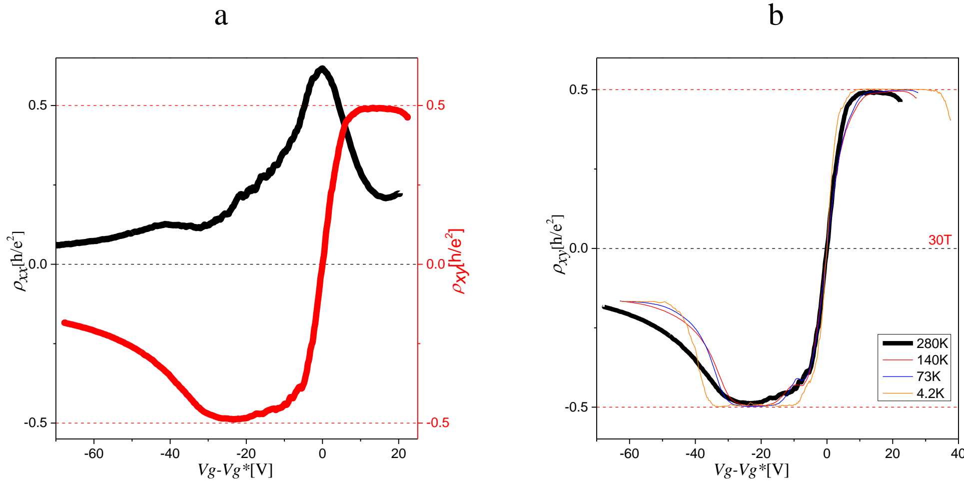

FIGURE 4.5: (a) Longitudinal resistance and transversal resistivity in h/e^2 unit versus normalized gate voltage at room temperature and 30T for low mobility ($1700cm^2V^{-1}s^{-1}$ at room temperature) graphene device (graphene on SiO_2). (b) Transversal resistance at different temperatures versus normalized gate voltage. Room temperature measurement is highlighted with a thicker black line.

A clear quantization appears at room temperature and 30T in this case, it is clear that when the transversal resistivity achieves the value $h/2e^2$ in the longitudinal resistance, an intense minimum appears. Unfortunately we

can plot only the longitudinal resistance, not the resistivity because this is a three probes measurements. Besides the quantization in the electron side is just resolved due to the high voltage appeareance of the Dirac Point (V_{CNP} around 70V and gate voltage leakage starts to appear at 90V). Neverthless the minimum are very clear also without a zoom. This evidence of quantization at room temperature in graphene on SiO_2 Hall Bar is in accordance with the previous result of Novoselov et al.[4].

The major robustness of this QHE in graphene on SiO_2 in comparison with encapsulated (higher mobility) devices is evident studying the dependence of the plateaus with filling factor $\nu = 2$ with the temperatures. In fact we observe a very large plateaus in both side.

4.1.3 Activation gap in encapsulated graphene

We report the estimation of the integer Landau activation gap for different encapsulated graphene devices. For this aim we measured ρ_{xx} as a function of the gate voltage at a constant high magnetic field (20T, 25T, 30T) and at different high temperatures (higher than $100K$). At these temperatures ρ_{xx} has a clear visible minimum at a certain carrier density correspondent to the filling factor $\nu = 2$ for holes 4.6(a) and electrons 4.6(b).

This resistance minima decreases with the temperature, approaching to a zero value for temperatures closed to $100K$. For $T > 100K$ the values of this minima resistance at different temperature can be fitted by Arrhenius plot:

$$\rho_{xx} \approx e^{-\frac{\Delta_a}{kT}} \tag{4.3}$$

From the linear fit of the $ln\rho_{xx}$ versus the inverse of the temperature (T^{-1}), as shown in Figure 4.6(c) for the holes side of the sample HBUN15, it is possible to estimate the activation gap (Δ_a) for all devices.

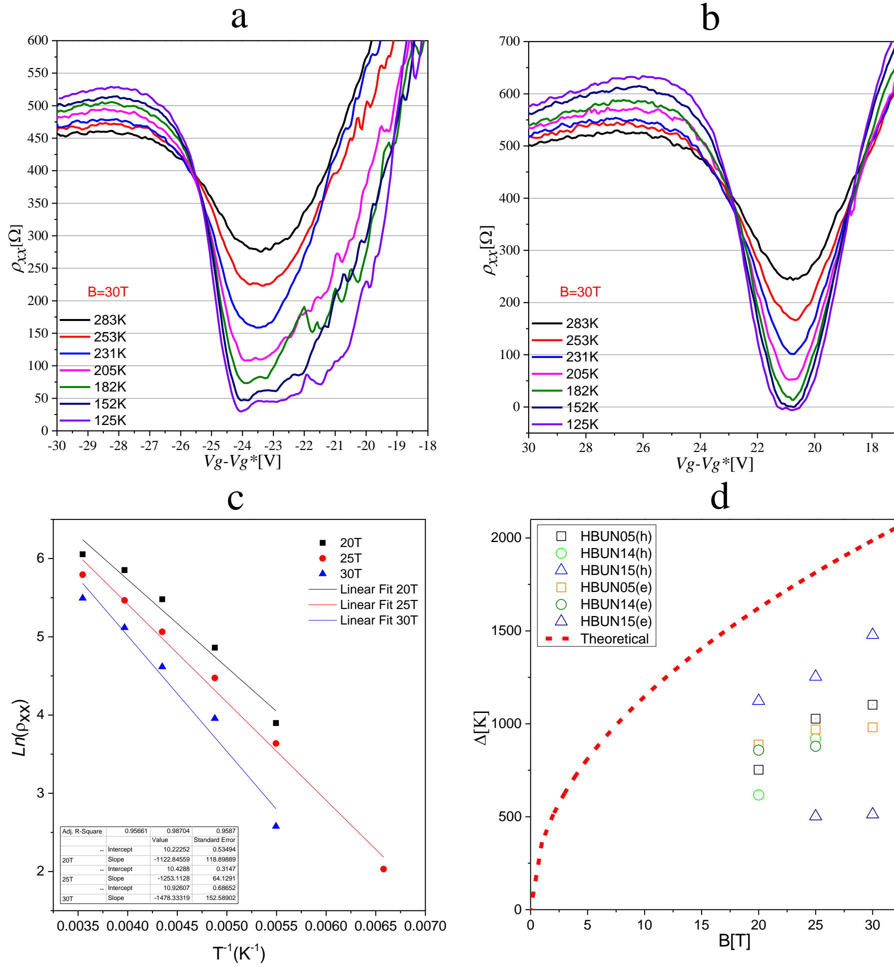

FIGURE 4.6: Longitudinal resistance at different temperatures as function of the gate voltage around the filling factor 2 for hole (a) and electron side (b). (c) Estimation of the activation gap from the resistivity versus the inverse of the temperature for HBUN15 (holes). (d) Dependence of the activation gap for different magnetic fields in comparison with the theoretically expected energy gaps for sharp Landau levels.

In Figure 4.6(d) we show the activation gaps estimated for three samples (HBUN05, HBUN14, HBUN15) at high magnetic fields (20T, 25T, 30T) and the theoretically expected energy gaps (dashed red line). Some values of the energy gaps are missing because in some cases the filling factor $\nu = \pm 2$ moved to gate voltage in which a leakage current through the gate insulator appeared.

Considering th bare Landau level separation that is given by the equation:

$$E_N = sgn(N)\sqrt{2\hbar v_F^2 eB \mid N \mid} \tag{4.4}$$

where v_F is the electron velocity ($v_F \approx 10^6 ms^{-1}$) that behaves as chiral Dirac fermions[76] with a linear dispersion $E = c\hbar \mid k \mid$ and N is the Landau level (negative for holes and positive for electrons), the measured energy gaps are not so close to the theoretical sharp Landau-level separation (according the formula 4.4) for all the devices. This behaviour diverges from the measured energy gaps of graphene on silicon oxide (for comparison see Figure 3(c) in [77]), in which the measured gap approached the theoretically energy gap for high fields ($B > 20$T). The approach to the theoretical energy gaps was explained in [77] with the special nature of the N=0 Landau level, in particular in high magnetic fields where the lowest Landau level is sufficiently separated from the neighboring levels. We can so suppose that the missing of the approaching behaviour in our encapsulated samples is due to the not enough separation between the lowest Landau level and the higher ones.

4.1.4 Zero-Landau level

We study in detail the lowest Landau level (LL) behaviour in particular if it is ruled by any scaling law. The scaling is related with the width of $\Delta\nu$ and the maximum value of $d\sigma_{xy}^{max}/d\nu$ at a certain LL, in which $\sigma_{xy} = \frac{\rho_{xy}}{(\rho_{xx})^2+(\rho_{xy})^2}$. For this aim we have firstly to obtain the filling factor ν, that is directly measured from the relation $\nu = nh/hB$ in which n is calculated from equation 4.2. So we can estimated $\Delta\nu$ from the two extrema of $d\sigma_{xx}/d\nu$ versus $d\nu$ around the Landau level zero (see black line in Figure 4.7(a)). $d\sigma_{xy}^{max}/d\nu$ (red line in Figure 4.7b) was estimated by the maximum in the peak of $d\sigma_{xx}/d\nu$ versus ν of the Landau level zero.

In Figure 4.7(b) we report $\Delta\nu$ and $d\sigma_{xy}^{max}/d\nu$ estimated for the zero-Landau level for high temperature ($T > 100K$) and high magnetic fields ($20T$, $25T$ and $30T$). There is not a clear trend of the data with the temperature, so a

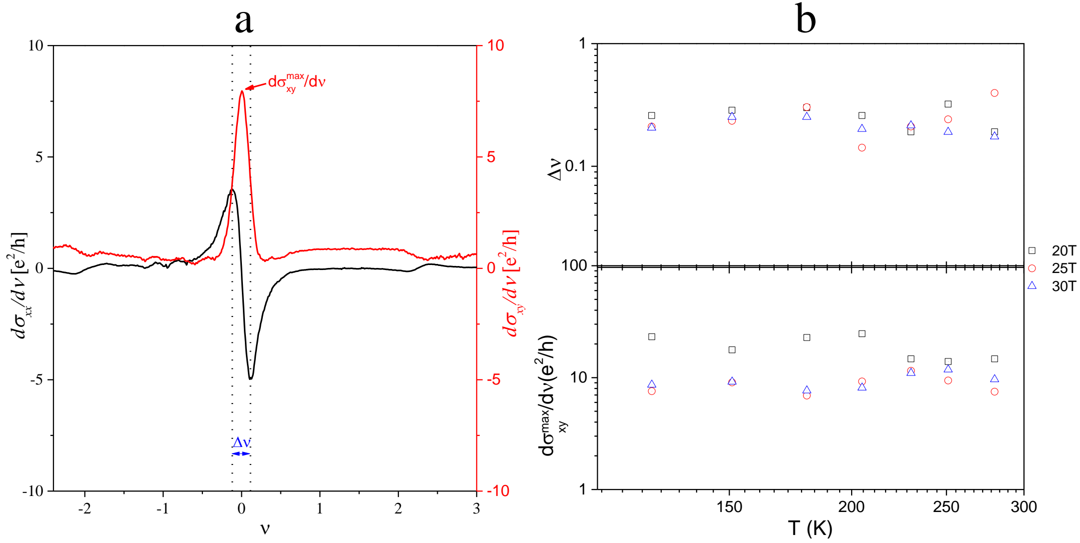

FIGURE 4.7: (a) Derivative of the longitudinal (black line) and transversal conductivity (red line) respect the filling factor ν, measured at room temperature and 30T. (b) Width $\Delta\nu$ and $d\sigma_{xy}^{max}/d\nu$ estimated for the zero Landau level at high magnetic fields (20 T, 25 T and 30 T) and high range of temperatures.

clear scaling of the QHE [78] cannot be deduced for the lower LL. The absence of a universal scaling was obtained also in graphene on silicon oxide [79], highlighting the different localization mechanism governed by an independent temperature localization length.

4.2 Fractional Quantum Hall effect in encapsulated graphene

Fractional Quantum Hall effect (FQHE) [80] has almost the same characteristic of QHE, except that the quantized Hall conductance is multiplied by a fraction for the fractional charge excitations due to strong Coulomb interactions and correlations among the electrons.

In graphene, QHE was observed from the beginning of its discovery [67], but only some years later FQHE was observed [69]. For graphene an important role is played by valley isospin that combined with the electron spin produce the four degenerate Landau levels, for this reason the FQHE in

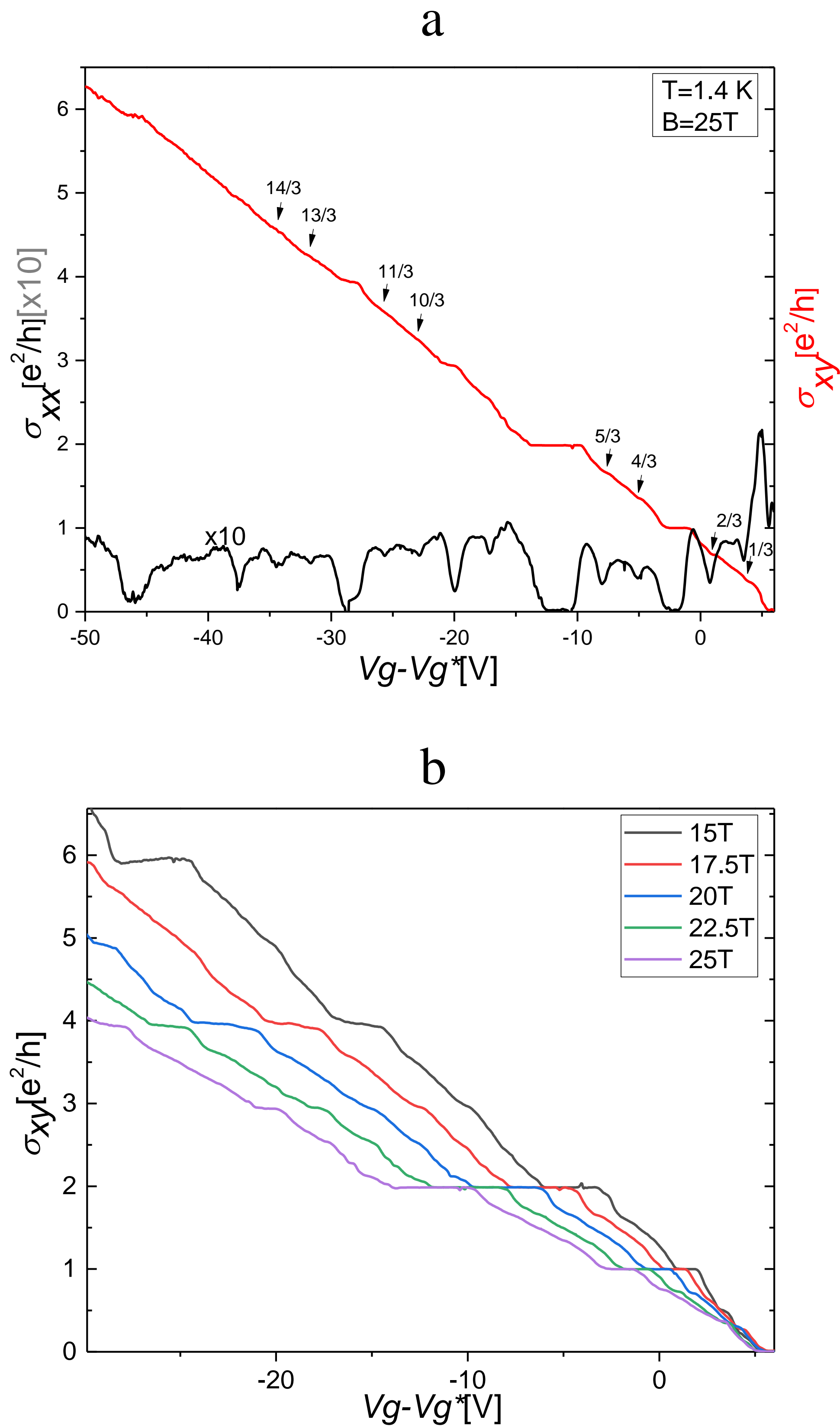

FIGURE 4.8: (a) Longitudinal (multiplied by a factor of 10) and transverse conductance in function of normalized gate voltage at 25T and 1.4K. (b) Transverse conductance for different magnetic field values (15T, 17.5T, 20T, 22.5T, 25T) at 1.4K.

graphene is different respect to other semiconductors and it is attracting a lot of attention. Standard low mobility graphene devices on SiO_2 does not permit the observation of FQHE, and few years ago only in high mobility suspended graphene was possible to observe the phenomena. The necessity of subtracting the contact resistance to the conductance (for the 2-probes measurements) in suspended samples and the difficulty in obtaining for sure the right quantized values, have made suspended graphene, in spite of their incredible mobility, not the best choice to study FQHE. With the advent of the Hexagonal Boron Nitride [26] high quality, high mobility and more stable samples were fabricated and FQHE was observed in SLG [5] and BLG [81] graphene. In this section we report the evidence of Fractional Quantum Hall Effect our graphene encapsulated in Hexagonal Boron Nitride device (HBUN05).

In Figure 4.8(a) FQHE is clearly observed at 25T and 1.4K. In the longitudinal conductivity (σ_{xx} in black line) deep minima appear in corrispondence of fractional values of the trasversal conductivity (σ_{xy} in red line).

The FQHE is observed also at lower magnetic fields (until 15T) as shown in Figure 4.8(b).

The appearance of FQHE in our encapsulated graphene represents another proof of high quality in our devices.

4.3 Conclusion

In this Chapter we studied the QHE at room temperature and high magnetic fields, focusing the attention on encapsulated graphene devices. To the best of our knowledgment it is the first time that this kind of study is made on hBN-graphene-hBN Hall Bars. In these devices we found a less pronounced quantization in comparison with the previous study [4] and our

measurements on a graphene on SiO_2 Hall bar. The missing of a clear quantization is probably due to different mechanisms of localization of charge carriers, mainly due to long range potentials and strain fluctuations, that govern disorder on encapsulated graphene devices. A smaller activation gap was found studying the filling factor $\nu = \pm 2$ in comparison with lower mobility graphene devices [77], as well as a no clear scaling law rules the graphene characteristic zero Landau level, similar to a previous work [79].

The high quality of our devices was confirmed by the evidence of FQHE at low temperature.

Chapter 5

Ballistic Transport in graphene Nanoconstrictions

The future use of graphene in electronics will depend on the full understanding of transport properties in nanostructures based on graphene. At the nanoscale the properties of graphene are strongly influenced by confinement effects and electronic edge states. Nanoconstrictions [82] and Nanoribbons [83] are intensively studied in the last year and different kind of effects as the creation and tunability of a electronic gap [84], edge states [85], Fano resonances [86], of topological phases [87] were predicted and/or observed in these systems.

One of the most intriguing phenomena expected in graphene Nanoconstrictions (GNCs) and Nanoribbons (GNRs) is the quantized conductance without the presence of magnetic field. There are two indipendent ways of achieving quantized conductance in graphene without the presence of the magnetic field. External potential gate can confine the density of the charge into a channel as well this charge confinement could be obtained by physically etched two-dimensional graphene flake into a narrow structure. The quantized conductance of GNCs was observed by Tombros et al. in the 2011 [6] in suspended graphene, and only several years after Terres et al. [88] and Kim et al. [89] were able to observe again quantization in GNCs sandwiched in hexagonal Boron Nitride. The main limitation of suspended

graphene is the inaccurate control in defining a NC with a certain size. The suspended two probes NCs of Tombros et al. was built by passing a high current through a previously suspended graphene flake, stretching and deforming it into a NC-like structure. The physically etched NCs of Terres [88] presented a high roughness of the edges where the ballistic behaviour of the NC differed from the theoretical one. The quantization appeared in form of 'kinks' but the separation did not correspond exactly to integer values of the quantum conductance ($2e^2/h$). Very clear quantization of $2e^2/h$ and $4e^2/h$ was instead observed thanks to the use of electrostatic potential gates in different recently electrostatic constrictions of monolayer [89] and bilayer graphene[37][90] but the observation of a clear size quantization in ballistic physically etched GNCs is most desiderable. One of the most important property of graphene is its intrinsic very high mobility also a room temperatures. A high mobility entails a large free mean path (l). When l is equal or major than the device/nanostructure lenght the ballistic regime is achieved. Obtain a truly ballistic regime is not technologically simple and this is basically the reason why more than a decade after the discovery of graphene, ballistic transport on graphene nanostructures still represents a challenging of research in two-dimensional systems. In this chapter we present a powerful theoretical model to predict graphene NCs and NRs transport and the experimental results of NCs fabricated in two different ways. We started to study GNCs fabricated with a HMDS (Hexamethyldisilazane) treatment where a quasi-ballistic regime was achieved and GNs fabricated in sandwiched hBN-Graphene-hBN structures where ballistic behaviour is satisfied on the whole device thanks to the very high mobility of encapsulated graphene.

5.1 Tight-Binding model

The electronic properties of graphene close to Dirac point can be accurately described by a tight-binding Hamiltonian for π electrons, $\mathcal{H} = -\sum_{\langle i,j \rangle} t_{ij} |i\rangle\langle j|$, where $|i\rangle$ is the atomic orbital of the i-th carbon atom [91]. The corresponding orbital energy level is set as the origin of energy without losing generality. Here t_{ij} stands for the hopping energy parameter between orbitals of the i-th and j-th carbon atoms and has been set to be constant between nearest-neighbor atoms ($t_{ij} = 2.8\,\mathrm{eV}$, see Ref. [92] and zero otherwise. Such approximation provides reliable results near the K and K' points of the Brillouin zone, as already reported in Ref. [93].

Neglecting electron-phonon [94, 95] and electron-electron[96] interactions in our calculations, we consider electrons in the fully coherent regime, hence with ballistic motion through the whole device. Combining the *quantum transmitting boundary method*, based on a finite element approximation [97], and an *effective transfer matrix method* adapted for graphene (see Ref. [98]) for technical details), the wave function in the whole sample and the transmission coefficient $\tau_n(E)$ for each mode at an energy E is calculated. These modes, also known as channels or subbands, arise from the transverse quantization due to the lateral confinement at the leads [99]. According to the Buttiker-Landauer formalism [99], at very low temperature the electrical conductance is proportional to the transmission coefficient at the Fermi energy E_F

$$G = \frac{2e^2}{h} \sum_n \tau_n(E_F)\,, \tag{5.1}$$

where the index n runs over the transverse modes. The factor 2 accounts the spin degeneracy whereas the valleys are considered explicitly in our tight-binding calculation of the transmission coefficient τ_n. As the NC becomes wider, the number of transverse modes for a given energy increases and so does the conductance. But interestingly, we found that the main features are

essentially the same provided that the conductance is plotted against Wk_F, where k_F is the Fermi wavenumber and W is the NC width. This has an important practical consequence, namely we can extrapolate results to much larger systems as the ones fabricated experimentally and otherwise computationally very expensive (or even impossible) to simulate.

To compare the experimental results with the ideal model we consider the conductance within the Landauer approach:

$$G = (\frac{2e^2}{h})\frac{2Wk_F}{\pi}t \tag{5.2}$$

Where for a constriction of width W the transmission parameter t will assume values between 0 and 1. In particular $t = 1$ for the ideal constriction whereas, instead smaller values are expected for constrictions with a certain roughness.

5.2 Transport measurements on Graphene Nanoconstrictions (GNCs) with Hexamethyldisilazane (HMDS) treatment

We have fabricated GNCs [100] through electron beam litography of mechanical exfoliated graphene flakes transferred to Si/SiO2 wafers treated before and after the exfoliation with hexamethyldisilazane, following a similar procedure to the one used by Caridad et al. [101]. Details on the fabrication process can be found in section 3.1.1. It is expected that graphene deposited on a hydrophobic substrate has better transport properties due to the HMDS immersion. In particular, these samples show higher carrier mobility and Dirac peaks closer to zero due to the low interaction of graphene with the substrate [31][32]. As we anticipated the edges of the GNCs play a crucial role in

the trasport properties of the NC. A high roughness implies variation from theoretical ballistic model [88]. From another perspectives for many years exfoliated graphene flakes over wafer of Si/SiO_2 had been used to obtain GNCs with low edge roughness and good control size [102]. The low carrier mobility due to the direct contact of graphene with oxide had prevented the observation of size quantization effects, instead other physical phenomena as charging effects [103] and interference [86] appear. For all this reasons fabrication of NCs with HMDS treatment represents a good compromise between good mobility and well defined edges.

In this section we present two-terminal transport measurements for GNCs fabricated on a graphene flake using the HMDS treatment described above. The results are representative and reproducible in similar devices with the same width and electron mobility. All transport measurements were taken at 5 K and we used two probes lock in technique for this kind of graphene samples.

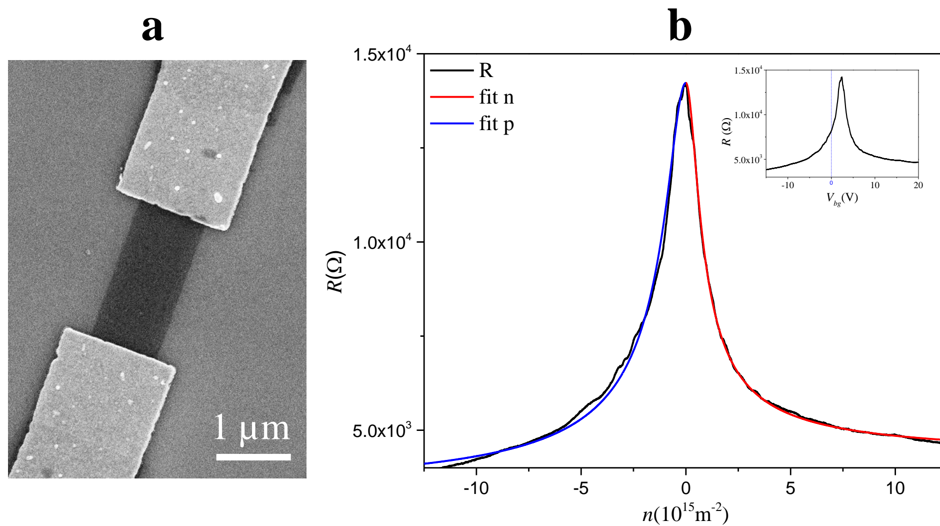

FIGURE 5.1: (a) SEM image of a bar of graphene (1μm*2μm) with HMDS treatment. (b) 2-probes resistance (R) versus carrier density carrier (n). In the insert the original resistance versus backgate voltage (V_{bg})

In Figure 5.1(b) we show the resistance of the graphene bar with HMDS treatment as a function of the carrier density n created by a back-gate voltage

V_{bg}. The 2-probes (1μm*1μm) bar is shown in the left side of Figure 5.1(a). In the inset of 5.1(b) the measured resistance versus the backgate voltage V_{bg} is shown.

From the inset is clear the effect of the HMDS treatment. The peak is close to zero volts and this is an indication of the reduction of the doping level in graphene due to the reduces effect of the substrate on the graphene itself. This carrier density can be estimated from the gate voltage with the formula 4.2, where this time C_{ox} is only the SiO_2 capacitance per area and V_{CNP} the voltage is less than 3 V in this device (see inset of Figure 5.1(b)). We can estimate the mobility, residual doping, and contact resistance by fitting our data with the FET formula 4.1 [73] [74] (Blue line for holes side, red line for electron side), as shown in Figure 5.1(b).

The values obtained for the bar with $N_{sq} = L/W$ when $L = 2\mu m$ and $W = 1\mu m$ yield a residual doping of $n_0 = 5.5 * 10^{10} cm^{-2}$. On the other hand, the mobility for the electrons is $\mu_n = 2 * 10^4 cm^2 V^{-1} s^{-1}$ whereas the hole mobility is $\mu_h = 1.3 * 10^4 cm^2 V^{-1} s^{-1}$. These values are comparable to those obtained in similar samples of graphene subjected to HMDS treatment [104], being higher than those of the standard graphene samples on SiO_2. From the mobility we can determine the elastic free mean path $l = \mu\hbar/e\sqrt{n\pi}$. For an electron density $n \approx 1 \times 10^{12}\,\mathrm{cm}^{-2}$ we obtain a value of l larger than 200 nm. Therefore, we can assume a ballistic regime in the NCs smaller than 200 nm.

In Figure 5.2(a) we show a SEM image of our devices, GNC with 85 nm of width.

Similar GNCs based on heterostructures of graphene and hexagonal boron nitride were studied by [88]. In spite of the high electronic mobility, they restricted their study to GNCs larger than 200nm due to several issues in the etching process of the heterostructure. So the dielectric nature of hBN is a complication for EBL masking. On the other hand, they obtained an high edge roughness during the etching process. Furthermore, the thickness of

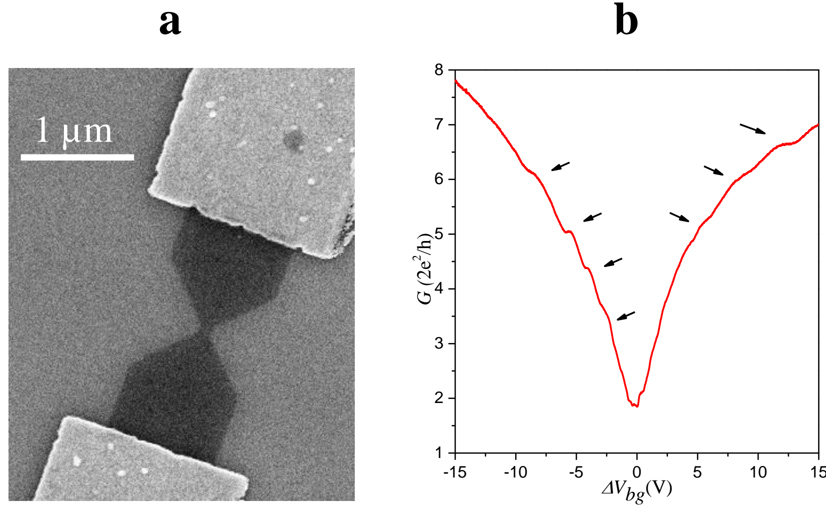

FIGURE 5.2: (a) SEM image of a GNC with HMDS treatment ($W = 85nm$) with HMDS treatment. (b) Conductance (G) of the GNC in $2e^2/h$ unit versus normalized backgate voltage (V_{bg}).

the heterostructure, usually thicker than 20 nm, demands aspect ratios much larger than in bare graphene monolayer flakes, as the graphene flake treated with HMDS.

The two-terminal conductance $G = Nsq/R$ (in e^2/h) as a function of the shifted back-gate voltage V^*_{bg} is shown in Figure 5.2(b). The curve shows a well-defined scaling $G \propto \left|V^*_{bg}\right|^{1/2}$. This scaling is regarded as an indication of both ballistic transport regime and homogeneity of the graphene flake. In particular, this trend is very similar to the two-terminal transport measurements reported in [6] in high-mobility suspended GNCs. Black arrows in Figure 5.2 highlight a set of reproducible kinks in the conductance curve. These kinks are well reproduced in several cool-downs and even with measurements taken after several months and after additional steps of HMDS cleaning. The separation between two consecutive kinks is less than $2e^2/h$, indicating a quasi-quantized conductance through the single GNC.

In Figure 5.3(a) we plot the conductance G in function of the Fermi wavenumber Wk_F where W is the width of the GNC and k_F is the Fermi wave number,

just after the HMDS treatment (black line) and when the effect of the treatment start to disappear (red line). We neglect a small additional contribution due to the localized trap states that would slightly modify the relation between n and k_F.

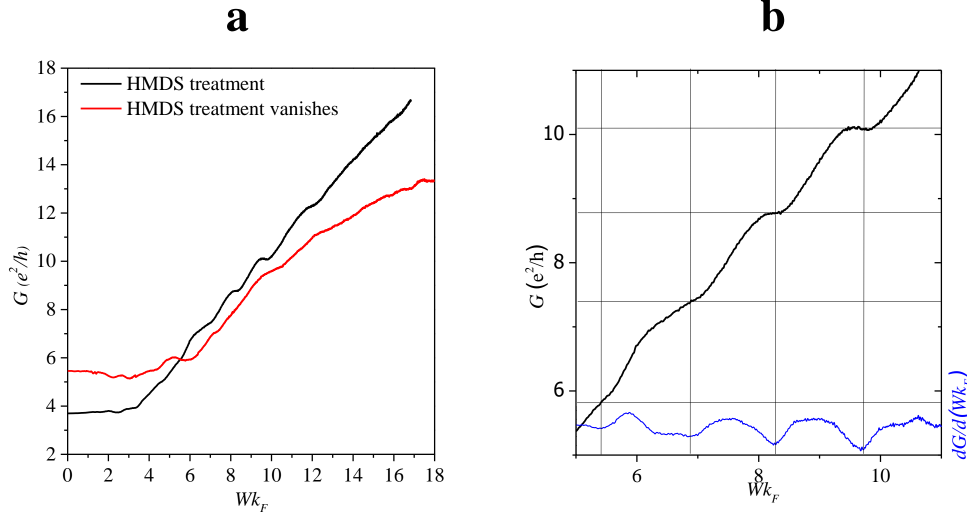

FIGURE 5.3: (a) Conductance (G) as function of the Fermi wavenumber k_F with (black line) and without (red line) the effect of HMDS.b) Conductance (G) (black line) and transconductance ($\frac{dG}{dWk_F}$) (blue line) of the GNC in e^2/h unit versus Wk_F.

Figure 5.3(a) shows that the experimental conductance achieves an almost constant value when $Wk_F < 4$ and a nonzero minimum value of the experimental conductance. These two facts are attributed to the residual doping in the graphene flakes, which prevents from achieving a zero carrier density experimentally. Accordingly, we cannot reach values of k_F below a minimum cutoff arising from the residual doping density n_0. From the linear fit of the conductance we find $k_F^{cut-off} = \sqrt{\pi n_0} = 4.2x10^{-5}m^{-1}$, with $n_0 = 5.5x10^{10}cm^{-1}$. After the minimum cutoff wavenumber, the linear behavior of the conductance with k_F is typical of ballistic system and this dependence changes when the effect of HMDS starts to disappear, so the mobility decreases and the ballistic regime is no longer satisfied.

In Figure 5.3(b) we plot the zoomed conductance (black line) in e^2/h unit as a function of the dimensionless magnitude Wk_F. The quantization is very

clear even if the separation between plateaus does not correspond exactly with the value of the quantum conductance. The plateaus appear in the minima values of the transconductance ($dG/(dWk_F)$), that is shown in the same graph with the blu line. Results of Figure 5.3(b) are similar to those predicted by Ihnatsenka and Kirczenow [105] who found plateaus in nanoconstrictions conductance and attributed them to the quantization due to the finite length of the GNC and in which small imperfections could lead in variation of the quantized value.

5.3 Transport measurements on Graphene Nanoconstrictions (GNCs) fabricated by cryo-etching in encapsulated graphene

As previously stated, the use of lattice-matched h-BN layers was a great leap forward into high-quality nanostructures, allowing for the fabrication of much higher mobility devices with intercalated graphene [82]. Electron transport properties of samples of encapsulated graphene show signatures of quantum conductance in form of *kinks* [88, 106]. Yet, the effect of roughness of the structure due to the intrinsic dielectric behavior of the h-BN film and the lack of control in the edge-definition of the heterostructures (of paramount importance to reduce edge scattering) have been detrimental for the appearance of well-defined plateaus of conductance. The problem of edge-definition and high roughness values was partially overcome thanks to the definition of GNCs with exfoliated graphene on hydrophobic silicon oxide substrate with the use of HMDS [100, 101]. As we said in the previous section this method increases the graphene mobility for a fair period of time after its treatment. The results reported in the previous section and as well in Refs. [101], show quantized conductance at zero magnetic field. This quantization appears,

once more, in form of *kinks*. This procedure represents a promising compromise between relatively high mobility and very good edge-definition (roughness of the order of 1 nm), but improvements on the etching definition in higher mobility and more stable graphene GNCs are necessary.

The fabrication process started from heterostructures of h-BN/graphene/h-BN and the details of fabrication can be found in section 3.1.3. It is important to highlight the role of cryo-etching technique used during the fabrication process.

This technique was commonly applied for bulk three-dimensional materials has been used in quasi-2D structures achieving an unprecedented control of the edge-definition. It was successfully implemented in silicon-based devices, where it was possible to control and define low-roughness sidewalls, observe the absence of sidewall scalloping[107], and generate samples with a high aspect ratio and cleaning[108] in nanometric-size structures[109]. The extension of the cryo-etching technique to graphene allowed us to built NCs with very low sidewall roughness.

We focus the attention on a h-BN/graphene/h-BN constriction of a few hundreds of nm width W. Figure 5.3(a) shows a tilted SEM micrograph of a typical NC in encapsulated graphene defined by cryo-etching. The lateral width of this NC is $W \simeq 206\,\text{nm}$ and the length is $L \simeq 200\,\text{nm}$. The inset shows the SEM micrograph at higher magnification, in which the sandwiched structure (h-BN/graphene/h-BN) is colored in sky blue. A standard 4–probes configuration to perform the electronic characterization at low-temperatures is sketched in the figure, where a pseudo-dc (13 Hz) current of 5 nA was injected/collected from the outer contacts while the voltage drop was measured by an in-phase lock-in preamplifier closer to the constriction (the contacts are gold colored for better clarity). The result of a typical measurement at $T = 3.1\,\text{K}$ is depicted in Figure 5.4(b). The conductance in units of e^2/h is displayed as a function of the normalized back-gate voltage $\Delta V_g = V_g - V_g^*$,

V_g^* being the value of the voltage at the CNP. The conductance is directly obtained by the measured contactless resistance as $G = 1/R$. The typical mobility in our best devices is $\mu \simeq 150\,000\,\mathrm{cm}^2/\mathrm{Vs}$ at room temperature, as shown in the previous Chapter 4.

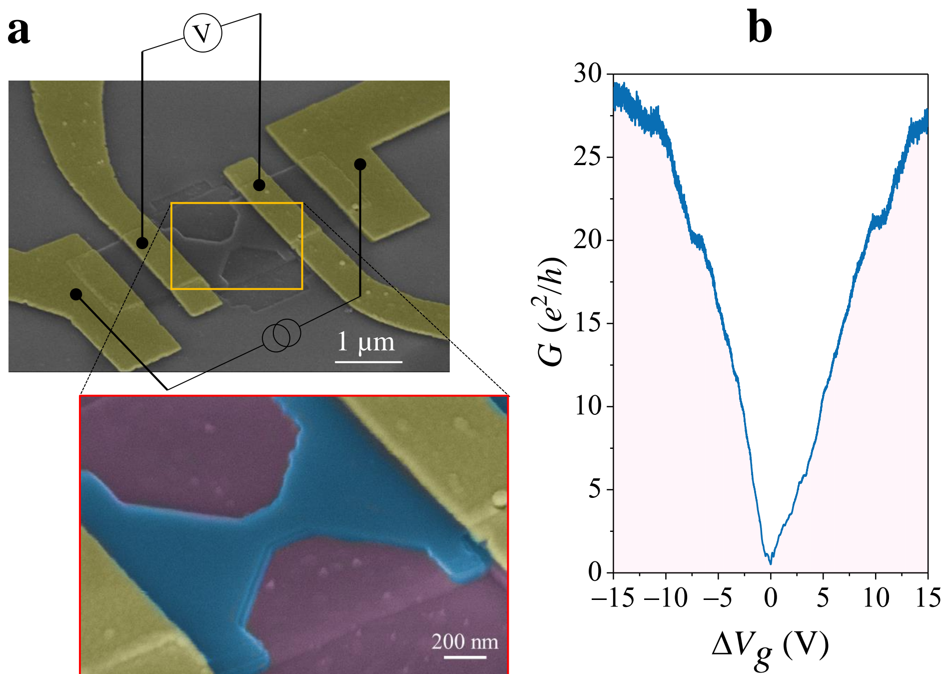

FIGURE 5.4: (a) Tilted SEM micrograph of an encapsulated graphene NC with lateral width $W \simeq 206\,\mathrm{nm}$ and length $L \simeq 200\,\mathrm{nm}$ including an schematic view of the electronic setup. The inset shows an enlarged view where the hBN/graphene/hBN heterostructure is colored in sky blue, the SiO_2 substrate (partially etched) in violet and the contacts in yellow gold. (b) Conductance as a function of the normalized voltage $\Delta V_g = V_g - V_g^*$ for the same NC measured at $T = 3.1\,\mathrm{K}$.

The very good definition of the graphene NCs is qualitatively visible in the SEM micrograph shown in Figure 5.3(a). However, in order to get a quantitative analysis of the edge roughness, AFM measurements were performed in our samples. We have used a Nanotech AFM instrument operating in contact mode. Figure 5.5(a) displays the AFM image of the whole NC. The edge and the corresponding contour profile within the square marked in panel (a) are shown in Figure 5.5(b). The AFM images reveal the excellent definition of our graphene NC and, in particular, the smooth sidewall. The contour plot (black line in Figure 5.5(b)) is taken 15 nm under the top hBN flake (with a

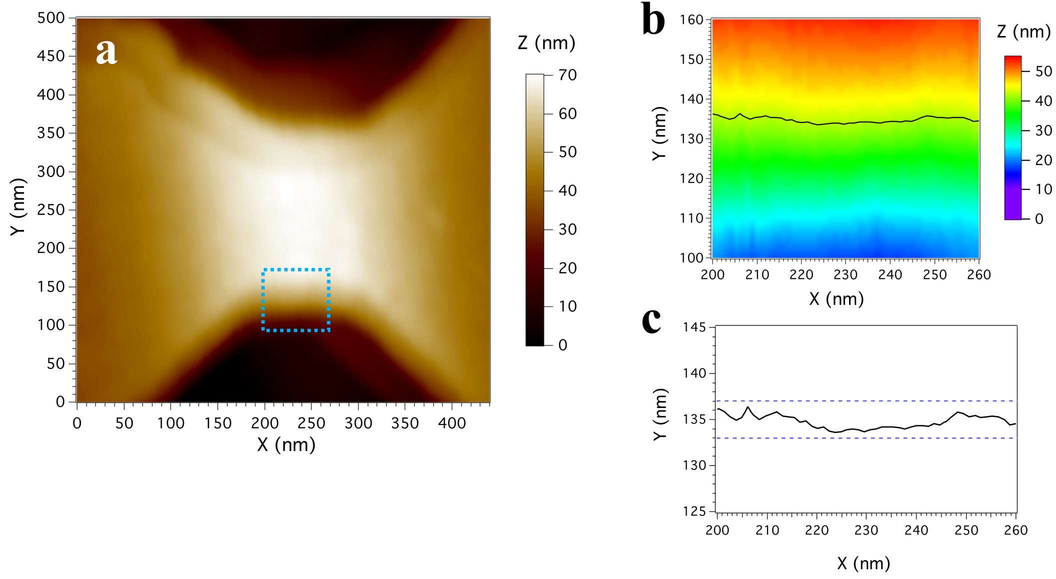

FIGURE 5.5: (a) AFM image of the graphene NC with $W = 206$ nm. (b) Contour plot taken from the square highlighted in panel (a), at 15 nm from the top of the nanostructure. (c) Enlarged view of the contour plot, where the dashed lines indicate the values used to estimate the edge roughness.

thickness of about 15 nm) in order to assess the actual size and roughness of the NC. The average edge roughness can be estimated by zooming in this profile and then a roughness around 2 nm is obtained (see Figure 5.5(c)). This value is not far from the edge roughness estimated in lower mobility graphene NCs on HMDS[101], namely without h-BN, where the value was of the order of 1 nm. Our measurement represents the first quantitative estimation of the roughness observed in encapsulated graphene nanoconstrictions as well.

In Figure 5.6(a), the conductance of 206 nm encapsulated graphene as function of the Fermi wave number k_F for the hole side ($V_g - V_g^* < 0$) is shown. The quantization steps are clearly developed for forward and backward currents (black and red line). The small shift in the red line is due to the residual gate doping but it does not affect the slope (proportional to the transmission parameter t). A linear fit of the conductance as a function of Wk_F shown in Figures 5.6(a) and 5.6(b) leads to transmission parameters $t = 0.865$ and $t = 0.863$ for the hole and electron sides, respectively. These

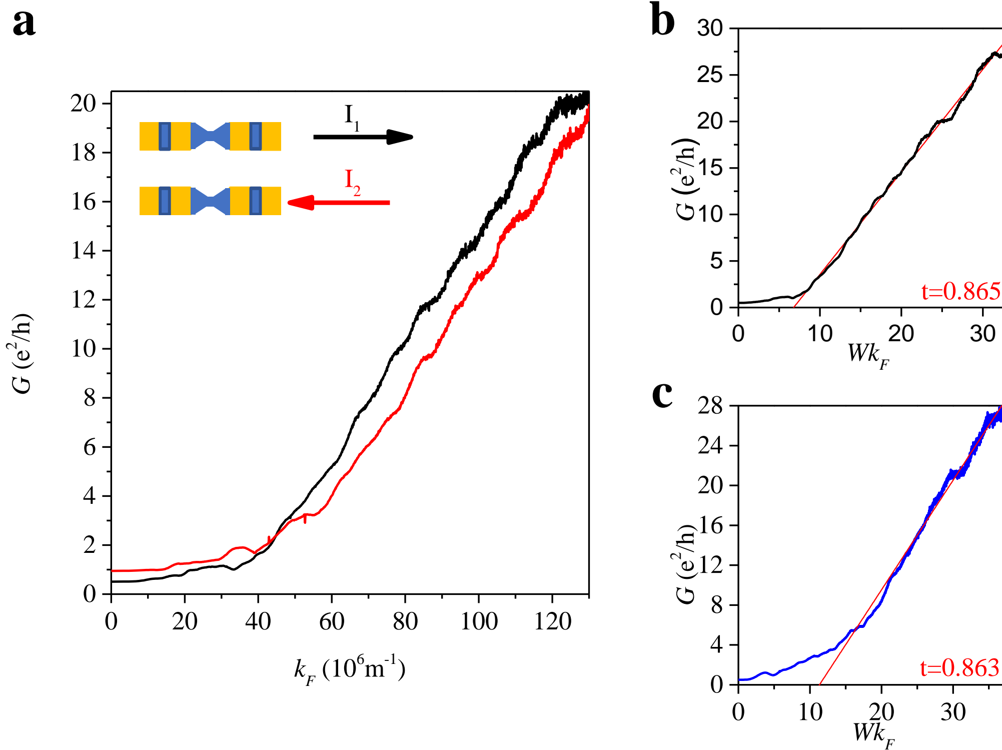

FIGURE 5.6: (a) Conductance in units of e^2/h versus the Fermi wavenumber k_F for forward and backward currents at the hole side, showing well-defined plateaus of the conductance. The transmission parameter t is obtained from the linear fitting of the conductance (in units of e^2/h) as a function of Wk_F for the (b) hole side ($t = 0.865$) and (c) electron side ($t = 0.863$). The width of the constriction is $W = 206\,\text{nm}$.

values are very close to each other. Furthermore, they are closer to unity than the value previously reported in [88]. From the normalized gate voltage ΔV_g we can obtain the carrier density n and therefore the Fermi wavenumber $k_F = \sqrt{\pi n}$. Due to the presence of residual doping in our NC, we cannot tune the carrier density below a minimum value $n_0 \sim 3.3 \times 10^{10}\,\text{cm}^{-2}$ experimentally, and accordingly Wk_F could not be tune below a threshold value $Wk_F^0 = \sqrt{\pi n_0}\,W \sim 6.7$ for the holes side. It is also apparent the larger residual carrier density in the electron side, yielding a threshold Fermi wavevector $k_F^0 \approx 65 \times 10^6\,\text{m}^{-1}$. In our sample the hole-side region ($\Delta V_g < 0$) is always better resolved than the electron one ($\Delta V_g > 0$), where the ballistic behaviour starts at higher back-gate voltage due to the residual charge density.

Thanks to the accurate profile obtained with AFM measurements, we are able to study also the real edge roughness in our simulations based on a tight

binding model.

Figure 5.7(a) shows the conductance G as a function of Wk_F measured at $T = 3.1\,\mathrm{K}$ (red line) and the theoretical conductance (blue line) from our tight-binding simulations with the same edge roughness obtained from the AFM measurements (Figure 5.5).

We note the good agreement of the experimental and simulated conductance as well as the linear dependence on Wk_F, characteristic of ballistic transport above a threshold value Wk_F^0. The transmission parameter t is estimated from the linear fit of the conductance when $Wk_F > Wk_F^0$ using Equation (5.2). It is worth stressing the remarkable agreement of the slopes obtained from the theoretical and experimental conductance curves, yielding the transmission parameter $t = 0.9$. This value is close to the fully transmitted carrier regime $t = 1$, in contrast to the $t \sim 0.6$ given in Ref. [88] for a graphene NC with a comparable width of $W = 230\,\mathrm{nm}$ that was not defined by cryo-etching. This result, supported by the remarkable agreement with theoretical calculations using realistic profiles of the edge roughness, is a clear indication of ballistic transport due to the very high mobility and smooth edges that arise from the novel use of the cryo-etching procedure in their preparation. The estimated value of t in our structure is also significantly higher than the one obtained in much narrower NCs of width $W = 100\,\mathrm{nm}$ produced by means of a HMDS treatment [100, 101] and reported in the previous section. In these samples, low-roughness edges are generated mainly due to the fact that the etching process on a single layer graphene is more controllable and a clean edge on a single layer of material is easier to attain than the one obtained on a thicker encapsulated graphene nanostructure. In that case, the corresponding transmission parameters are significantly lower than the ones found in encapsulated graphene NCs defined by cryo-etching.

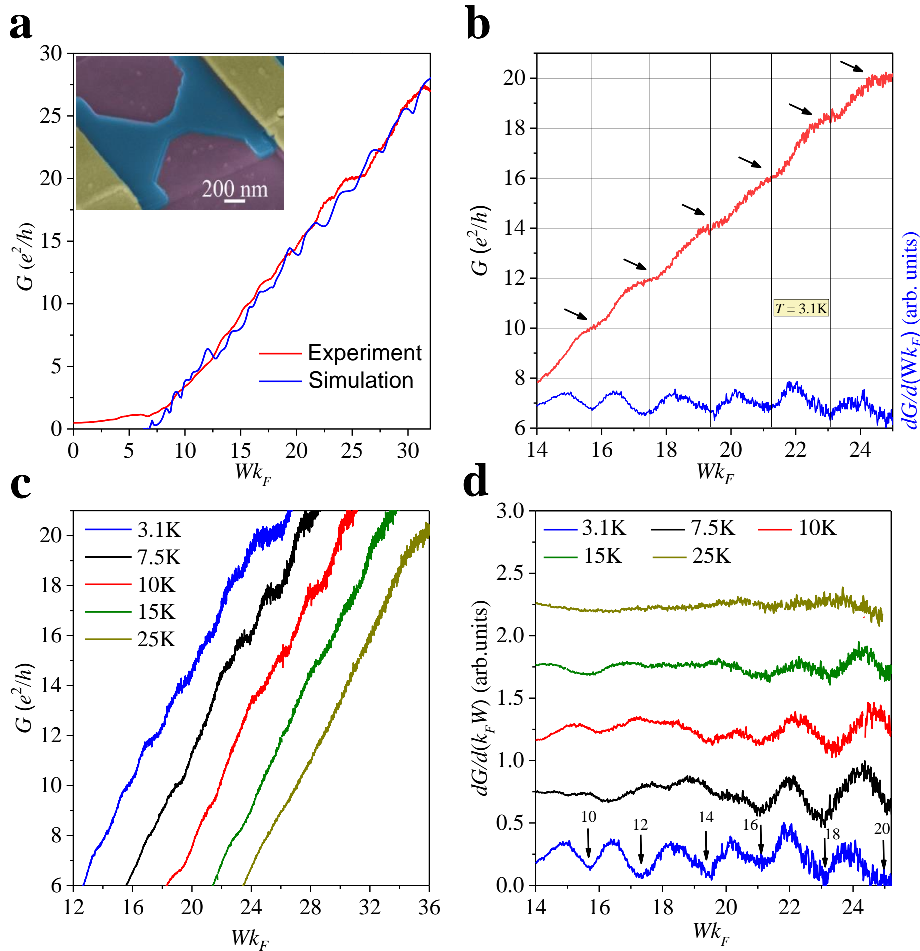

FIGURE 5.7: (a) Comparison of simulated and experimental conductance of a GNC of width $W = 206$ nm. (b) Conductance (red line) and transconductance (blue line) as a function Wk_F measured at $T = 3.1$ K. Solid black arrows show the position of the plateaus of conductance separated by $2e^2/h$ and matching integer values from $G = 10e^2/h$ onwards. (c) Evolution of G as a function of Wk_F at different temperatures. The curves have been horizontally shifted by a factor $2.5Wk_F$ for clarity. (d) Temperature dependence of the transconductance as a function of Wk_F. Black solid arrows represent the value of the plateaus of conductance in units of e^2/h at $T = 3.1$ K, matching the position of the minima in $dG/d(Wk_F)$.

A closer inspection of the conductance G (red line) and the dimensionless transconductance $dG/d(Wk_F)$ (blue line) versus Wk_F is shown in Figure 5.7(b), signaling the second goal of this work. The plateaus of quantized conductance are clearly observed at regular intervals of Wk_F, corresponding to equally spaced marked minima of the transconductance. The quantization of G is also very clear after reverting the direction of the current. Up to six plateaus appear at values of the conductance of $G = 10, 12, 14, 16, 18, 20\, e^2/h$, hence the jump between neighboring plateaus has been found to be $2e^2/h$. This value matches the theoretical estimation by Guimarães *et al.*, where the conductance of a graphene NC where $W \sim L$ is quantized into well-defined plateaus separated by $2e^2/h$[110]. Ihnatsenka *et al.* put forward electron-electron interaction and boundary scattering as the major responsible for the appearance of plateaus separated by $2e^2/h$ instead of $4e^2/h$, [105] as it would be expected in ideal nanoribbons with perfectly smooth edges where both spin and valley degeneracy are preserved [89]. To the best of our knowledge, this is the largest number of plateaus of conductance observed in single layer graphene samples that have been have been physically narrowed down into nanoconstriction-shape to date. While in bilayer graphene it is noticeably easier to confine carriers due to the presence of an already existing gap and hence plateaus of conductance are easier to achieve[37, 90], shaping electrostratically the conductive region into a constriction[37, 89] allows to narrow-down the constriction further into a few tens of nm wide structure and to diminish the number of channels responsible of electric conduction. Our approach becomes a good compromise to achieve almost fully transmitted structures with smooth sidewalls where a systematic experimental study of NCs having differing widths may developed. In Figure 5.7(c) we present the temperature dependence of the conductance (taken at $T = 3.1, 7.5, 10, 15$

and 25K), where the curves have been shifted by a factor of $2.5Wk_F$ for clarity. The presence of the plateaus is clear and they are noticeably visible below $T \sim 10\,\mathrm{K}$. They start to smear out at higher temperatures until they are completely washed out at $T = 25\,\mathrm{K}$. Such a temperature dependence of G can be better studied by inspecting the dimensionless transconductance as presented in Figure 5.7(d). The amplitude of the periodic oscillations of the transconductance as a function of Wk_F decreases by increasing temperature and finally disappears above $T = 15\,\mathrm{K}$. A similar threshold temperature for the vanishing of the conductance quantization was very recently found in bilayer graphene constrictions[90]. This behavior differs markedly from other non-desired effects, such as localized charge carriers, that disappear at higher temperature.

5.3.1 Graphene constriction defined with Orion Nanofab Helium Ion Microscope

Even if nanometric size is achieved through electron beam lithography, the technique is limited by the well-known "proximity effect". This effect basically is a ’charge’ effect due to the backscattering of electrons and comports unwanted exposition area that limits the resolution. In graphene devices the use of PMMA is probably the best choice but the maximum achieved resolution is not enough for smaller size features (lower than 50 nm).

For this reason in September 2017, during one of my PhD stay at Zeiss SMT in Peabody (USA), we defined the nanoconstrictions/nanoribbons on graphene samples through the Orion Nanofab Helium Ion Microscope. This is a special microscope with Helium Ion as beam, in this way there is no proximity effect and the resolution of the equipment is sub-nanometric for imaging and sub-10nm for definition of materials. In comparison with a standard FIB (Focused Ion Beam), where the Ion is typically Gallium, the use of

Helium is much less invasive for the specimen.

The definition of nanoconstrictions and nanoribbons through this technique is reported in the SEM images of Figure 5.8. In particular in (a)(b) encapsulated graphene constrictions of ≈30 nm and ≈ 60 nm and (c)(d) nanoribbon of 85 nm and nanocostriction of the same size on the exfoliated graphene on SiO_2 are reported. In spite of the incredible nanometric definition, after the definition of the nanoconstriction/nanoribbon, the devices became high resistive or stopped to work. We found main reasons. The first one is the necessity to improve the last process (i.e. reduction the exposition time), the second problem could be related with the transport of these fragile samples. A possible solution for the future, it consists in changing the order of fabrication steps, defining the nanoconstriction/nanoribbons before the etching for the "side"contacts and the deposition of the contacts.

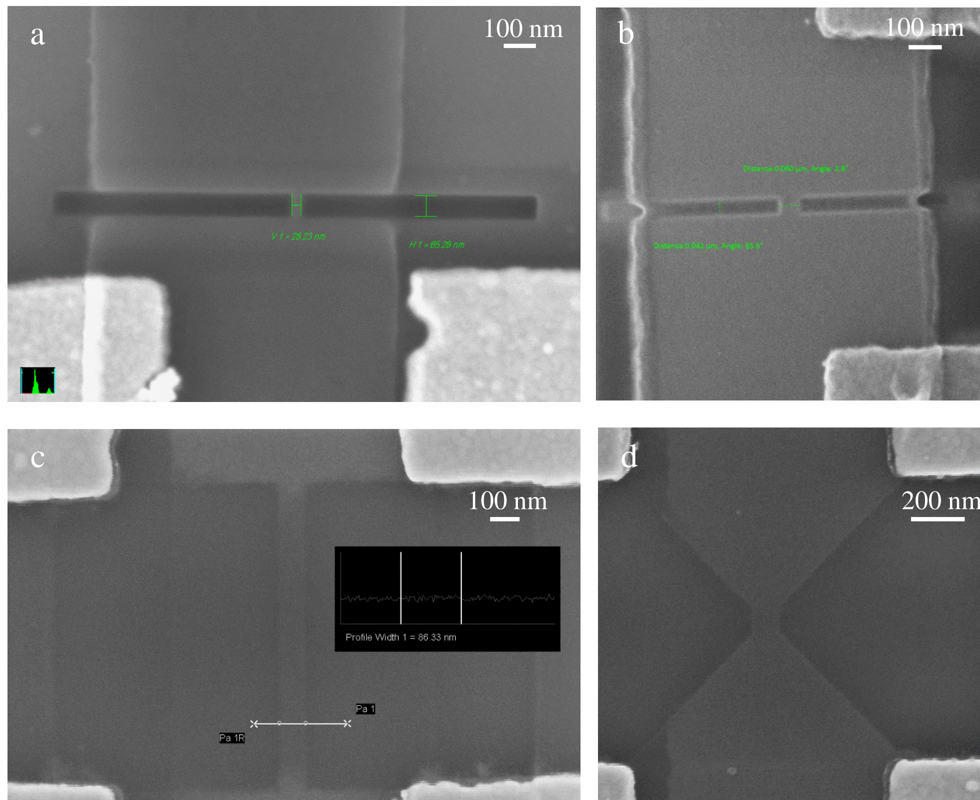

FIGURE 5.8: Sem images of : (a)(b) Nanoconstrictions in encapsulated graphene of ≈30 nm and ≈ 60 nm, (c)(d) Nanoribbon and nanocostriction of ≈ of 85 nm in graphene on SiO_2 with HMDS treatment.

5.4 Conclusion

Starting from the HMDS treatment graphene nanoconstrictions, that represent a good compromise between good mobility and high edge definition[111], we pass to a novel implementation of the cryo-etching method, which we used for fabrication of high quality encapsulated graphene nanoconstrictions. The main advantage of the method is an unprecedented control of the edge definition and reduced roughness. The latter enabled us to fabricate high-mobility hBN-encapsulated graphene nanoconstrictions with well defined, sharp and extraordinarily smooth edges. These systems have been characterized by the standard AFM imaging techniques and then the obtained data on the realistic geometry was used in the large scale theoretical transport calculations. Results of such modelling agree very well with our experimental measurements and suggest that the transport in the system is almost fully ballistic. In particular, both the predicted and measured values of the transmission parameter are as high as $t = 0.9$. On the other hand, the size quantization is clearly manifesting itself as a ladder of several equally $2e^2/h$-spaced plateaus of conductance at temperatures up to $T = 10$ K, confirming the high quality of the samples. We claim that the cryo-etching technique paves the way to study truly-ballistic-high-mobility encapsulated graphene-based nanostructures where definition of the edges and the control of the scattering processes are crucial.

Chapter 6

Magnetotransport Measurement on InAs/GaSb double quantum wells (DQWs)

As shown in Chapter 4, graphene is an ideal candidate to study QHE and FQHE due to its incredible properties. In 2005, Kane and Mele [112], starting from a earlier model of Haldane [76], proposed in graphene a new state of the matter: the Quantum Spin Hall State. The Quantum Spin Hall Effect (QSHE) is characterized by quantized spin-Hall conductance and a vanishing charge-Hall conductance without the presence of magnetic field, there is no breaking of the time reversal symmetry and Helical edge states (Two states with opposite spins) counterpropagate at a given edge. Unfortunately graphene has a weak spin orbit coupling and only through the application of a large magnetic field is possible to observe properties [113] analogous to the ones of the quantum spin Hall (QSH) effect.

In recent years, new electronic materials, topological insulators (TIs), have been attracting increasing interest thanks to the possibility of hosting new exotic states of matter [114][115], including QSHE. Among many TIs, the InAs/GaSb double quantum wells (DQWs) are of particular interest, as they

can readily be integrated within current semiconductor processing technologies. In this material system, the top of the valence band of GaSb is 0.143 eV higher than the bottom of the conduction band of InAs [116]. Due to the quantum confinement effect, the alignment of E_0 (the lowest electron subband in the conduction band) and H_0 (the highest hole subband in the valence band) can be tuned by varying the wells' thickness (an alternative way is represented by application of an electrical field [117]). For a given thickness of the GaSb QW, the bilayer is a conventional semiconductor provided that the thickness of the InAs QW is sufficiently small to keep E_0 above H_0 [118]. Above a critical thickness of the InAs QW, a quantum spin Hall (QSH) phase is realized [119] due to the inversion between the electron and the hole ground levels. Recently new signatures for the inverted phase in InAs/GaSb were studied [120][121] as well as edge transport in the trivial phase [122]. However, little is still known about the transport properties at the critical thickness, which corresponds to the phase boundary between the normal insulator (NI) and the QSH insulator.

Here we report transport measurements on InAs/GaSb samples in different regimes (normal, critical and inverted regime). In particular in the critical sample, we observe a narrow and intense maximum (≈500 kΩ) in the four-terminal resistivity in the charge neutrality region, separating the electron-like and hole-like regimes, with a strong activated temperature dependence above T = 7 K and perfect stability against quantizing magnetic fields. We discuss several mechanisms for that unexpectedly large resistance in this zero-gap semi-metal system including the formation of an excitonic insulator state.

More than 50 years ago, Mott made a seminal observation on the anomaly at the transition from a metal to a semiconductor [123]. Later on, Knox and co-workers [124] developed this idea and argued that, if in a semiconductor

(which at low temperature is insulating) the binding energy (EB) of the excitons exceeds the energy gap (E_g), the conventional insulating ground state would be unstable against a new phase, dubbed excitonic insulator, which originates from the formation of an exciton condensate. The low temperature behavior of the conductivity for an excitonic insulator was theoretically predicted by Jerome and co-workers [125] and many other studies, both theoretical and experimental, have been performed afterwards [126, 127, 128, 129, 130, 131, 132, 133, 134, 135, 136, 137, 138, 139, 140]. Although experimental evidence on the existence of this unusual insulating state has been reported [129], no completely conclusive results have been obtained so far.

6.1 8-Band $\mathrm{K}\cdot\mathrm{P}$ Calculation of InAs/GaSb Double Quantum Wells

An 8-band $\mathbf{k}\cdot\mathbf{p}$ method was employed to calculate the band structures of these DQW samples, using the Hamiltonian and basis functions of Ref. [141] and considering the strain effect resulting from the lattice mismatch between the GaSb substrate and each individual QW layer 2.

In the following, we briefly describe the 8-band $\mathbf{k}\cdot\mathbf{p}$ numerical method utilized in the main text to determine the critical thickness d_c of the InAs quantum well (QW) and to calculate the energy bands of Figure 6.1(a). It shows the structure of the InAs/GaSb double quantum well (DQW) samples, where the growth is along the $[001]$ direction (defined as z) of the GaSb substrate.

In our calculation, we used the Kane Hamiltonian and the corresponding basis functions of Ref. [141], considering the quantum confinement along z. The k_z in the Kane Hamiltonian is thus replaced by a momentum operator, while the in-plane momentum k_x and k_y still take continuous values because

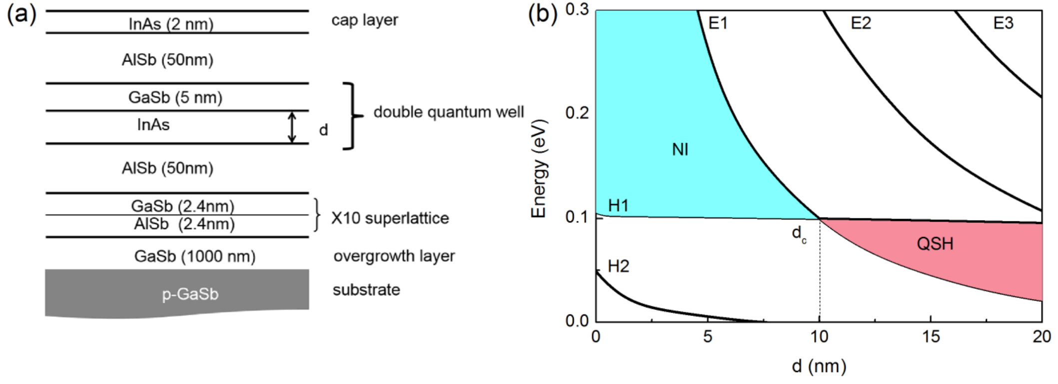

FIGURE 6.1: (a) Schematic structure of the InAs/GaSb DQW samples. (b) Evolution of the electron and hole subbands as a function of the InAs thickness d, calculated using the 8-band $\mathbf{k}\cdot\mathbf{p}$ method. The critical thickness d_c, corresponding to the boundary between the normal and inverted band structures, is found to be $d_c = 10.03nm$.

of the translational invariance. Following the envelope function theory [142], the wave function $\Psi(\mathbf{r})$ can be expanded in terms of the envelope function F_n and the Bloch function U_n of the nth spinor:

$$\Psi(\mathbf{r}) = \sum_n F_n(\mathbf{r})U_n(\mathbf{r}) \tag{6.1}$$

where $F_n = e^{ik_x x + ik_y y} f_n(z)$ and U_n is assumed to be independent on the material of each layer. Within the framework of $\mathbf{k}\cdot\mathbf{p}$ theory, the envelope function can be determined by solving a set of coupled differential equations. We assume that all the band parameters are discontinuous at each interface, which is described by the piecewise function along the growth direction and take the limit of zero temperature. We employed an axial approximation by replacing the second and third Luttinger parameters with their average in the Hamiltonian.

In addition to the quantum confinement effect, we considered the strain effect due to the lattice mismatch between the GaSb substrate and each individual QW layer, using the strain Hamiltonian that is described in Ref. [143]. Here, since the QWs are grown along $[001]$ direction, we also assumed a biaxial strain. In this case, the off diagonal elements of the strain tensor matrix

are zero and the diagonal elements are $\epsilon_{xx} = \epsilon_{yy} = \frac{a_0 - a}{a}$ and $\epsilon_{zz} = -\frac{C_{12}}{C_{11}}\epsilon_{xx}$, where a_0 and a are the lattice constants of the substrate and layer material respectively, and C_{11} and C_{12} are the stiffness constants.

In order to solve this set of coupled differential equations, $f_n(z)$ is expanded in plane wave basis. The wave function of the sth subband can then be written as:

$$f_n(z) = \frac{1}{\sqrt{L}} \sum_{m=-N}^{N} c^s_{nm} e^{ik_m z}$$

where L is the total thickness including the thickness of the DQW and the top and bottom AlSb barriers, and $k_m = \frac{2m}{L}$. Such expansion implies that the wave function is continuous across each interface. The plane wave expansion also helps to reduce the coupled differential equations to a more straightforward eigenvalue problem, which can be solved numerically although the size of the matrix increases to $(8(2N + 1))2$. In our calculation, we use $N = 20$.

Finally, following the formalism described above, we calculate the band structures of the InAs/GaSb DQWs (sandwiched between two 50 nm AlSb barriers) as a function of the InAs thickness d. The GaSb QW is fixed at 5-nm-thick, while the thickness of the InAs QW varies from 0 to 20 nm. In Figure 6.1 (b) we plot the low-energy subbands of the DQW at the Γ point as a function of d, with the energy of the bottom of the conduction band in InAs being set to zero. The critical thickness d_c, corresponding to the boundary between the normal and inverted band structures, is found to be $d_c = 10.03$ nm. The band parameters used in our calculation have been taken from Refs. [141][143][142][144] and summarized in the Table 6.1.

Band Parameters	InAs	GaSb	AlSb
E_g (eV)	0.417	0.812	2.386
E_v (eV)	-0.417	0.143	-0.237
E_p (eV)	21.5	27.0	18.7
Δ (eV)	0.39	0.76	0.676
A_c (eV nm^2)	-0.18	-0.09	-0.004
γ_1	2.81	2.31	2.57
γ_2	-0.093	-0.842	-0.116
γ_3	0.607	0.458	0.664
a nm	0.6058	0.6096	0.6136
C_{12} (GPa)	452.6	402.6	434.1
C_{11} (GPa)	832.9	884.2	876.9
a_c (eV)	-5.08	-7.5	-4.5
a_v (eV)	-1	-0.8	-1.4
b (eV)	-1.8	-2.0	-1.35
d (eV)	-3.6	-4.7	-4.3

TABLE 6.1: Table with the summary of the band parameters

6.2 Anomalously large resistance at the charge neutrality point in a zero-gap InAs/GaSb bilayer

In Figure 6.2(a) we plot the evolution of the calculated band structures of the InAs/GaSb DQW for at three different d values of the InAs QW thickness d, corresponding to the normal, critical and inverted regimes.

We found that for $d < 10$ nm, $Eg > 0$, signaling a normal semiconductor band structure, while for $d > 10$ nm, $Eg < 0$, indicating the band-inverted regime of the DQW InAs/GaSb. At $d = d_c$ =10 nm (critical thickness) we obtain $Eg = 0$, which corresponds to the boundary between the normal and inverted band structures. Recent cyclotron resonance infra-red measurements in magnetic fields [145] confirmed our assignment of these three regimes. In Figure 6.2(b), we report also the schematics energy of band profiles [118] of the samples in the three conditions. In Figure 6.2(c) we plot the four-terminal resistance measured as a function of gate voltage (V_g) in three typical samples, for which where the InAs QW thickness is 9 nm (sample A), 10 nm

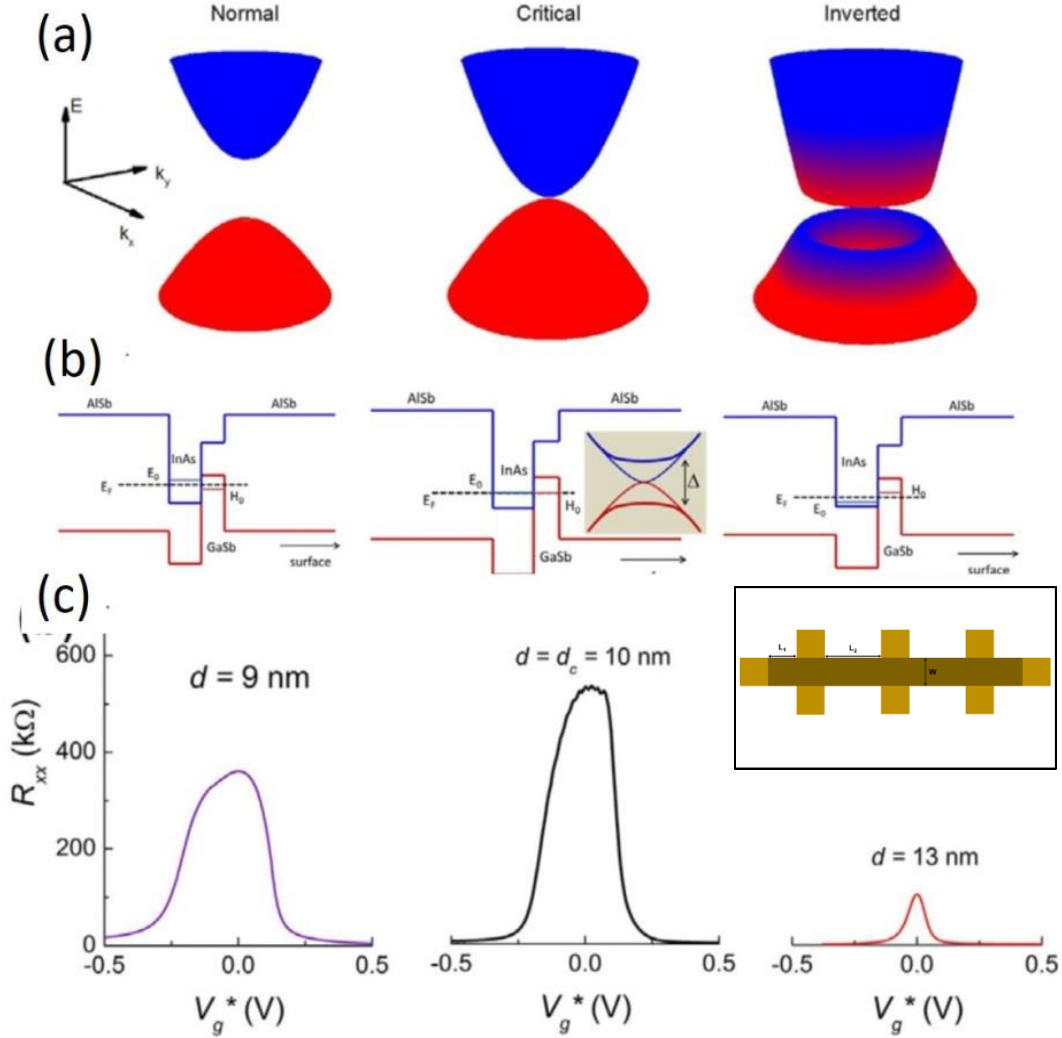

FIGURE 6.2: (a) Band structures of the InAs/GaSb DQWs calculated using the 8-band $\mathbf{k} \cdot \mathbf{p}$ method (see previous section) for three typical configurations: (left, sample A) d = 9 nm, (middle, sample B) d = 10 nm, and (right, sample C) d =13 nm. (b) shows schematic band profiles for samples A-C, respectively. E_0 is the lowest electron subband in the conduction band and H_0 the highest hole subband in the valence band. E_F is the Fermi level, at the charge neutrality point. The shaded inset in the middle panel shows the opening of the energy gap (Δ) due to the formation of an excitonic insulator phase. (c) displays 4-terminal resistance as function of gate voltage, measured at T = 500 mK, in samples A-C, respectively. The gate voltage is normalized so that the gate voltage at the CNP is zero ($V_g^* = V_g - V_g^{CNP}$). Hall Bar configuration of the measured samples in the inset of the bottom figure, in which $W = L_1 = 250\mu$m, $L_2 = 500\mu$m

(sample B), and 13 nm (sample C), respectively. All the samples have a Hall Bar geometry, with $L_1 = W = 250\mu$m, $L_2 = 500\mu$m, as shown in the inset of Figure 6.2(c). The CNP peak was centered in each sample at $V_g = -0.60$V (sample A), $V_g = -0.53$ V (sample B), and $V_g = -0.70$ V (sample C) and in the Figure 6.2(c), the gate voltage is normalized so that the CNP corresponds to $V_g^* = 0$ V.

In all three samples a resistance peak, centered at the CNP, separates two highly conductive regions associated to positively ($V_g^* < 0$V) and negatively-charged carries ($V_g^* > 0$V). The sign of the carriers in the two regimes was confirmed by Hall measurements at a finite magnetic field. Most strikingly, for $d = d_c = 10$ nm, where the electron and hole subbands are degenerate (middle panel of Figure 6.2(a) and a semi-metal phase is expected, the 4-terminal resistance reaches an overwhelmingly large value $\approx 530k\Omega$ in the CNP (Figure 6.2(c), the middle panel). Measurements with both constant current and constant voltage bias were carried out to confirm the value of this resistance peak. In contrast, in d = 9 and 13 nm DQWs, where the band gap is either positive or negative, the resistance in the CNP assumes smaller values: in the normal regime (Figure 6.2(c), the left panel), the resistance at the CNP is 400 $k\Omega$, while in the inverted regime (Figure 6.2(c), the right panel), the resistance is ≈ 60 $k\Omega$.

6.2.1 Temperature Dependence

By comparing our experimental data with previous studies, we propose that such high resistance state in our critical thickness sample is probably due to the formation of an excitonic insulator phase.

First, we observed that the maximum value of R_{xx} shows very weak temperature dependence at low T (see Figure 6.3(a)). We note here that this low temperature saturation behavior is different from the insulating state at

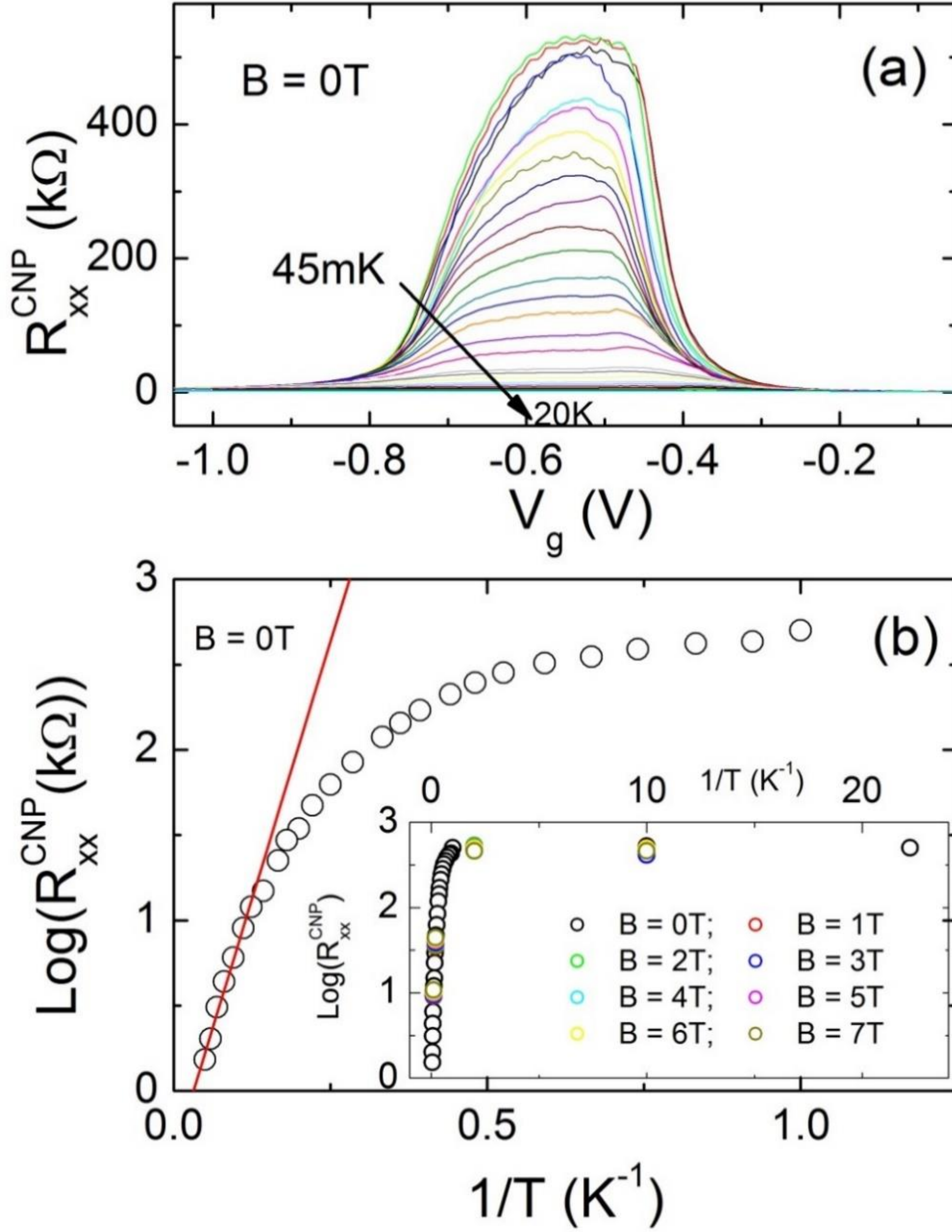

FIGURE 6.3: (a) Longitudinal resistance R_{xx} as a function of gate voltage Vg for different temperatures (40mK-20K) at $B = 0T$, measured in sample B. (b) maximum of R_{xx} in the CNR as a function of $1/T$. The red line is a fit to $R_{xx}^{CNP} \sim e^{\frac{\Delta}{2k_BT}}$, obtained for the data at $T > 7K$, which provides the estimation of the energy gap Δ reported in the text. The inset shows the temperature dependent data of R_{xx}^{CNP} at various magnetic fields.

the charge neutrality point (CNP) in the single layer graphene[146]. On the other hand, this weak temperature dependence seems to be a generic feature in InAs/GaSb heterostructures [147][148][149][150], whether in the normal, critical, or inverted band regimes. The exact origin of this anomalous temperature dependence is not understood and requires more detailed studies. The high-T regime ($T > 7K$) is properly described by an activated behavior $R_{xx}^{CNP} \approx e^{\frac{\Delta}{2k_BT}}$. The best fit of R_{xx}, shown in Figure 6.3(b), gives an estimated energy gap $\Delta = 2.08 \pm 0.10\ meV$. Temperature dependence measurements of R_{xx}^{CNP} were also carried out in sample A and sample C, and the results are shown in Figure 6.4. The energy gap in normal semiconducting sample A ($\approx 3.3\ meV$, see Figure 6.4(b)) is quite different from that found in other normal semiconducting InAs/GaSb bilayers. For example in Ref. [118] the authors report an energy gap of $\approx 0.5\ meV$, which is value is six times smaller than that measured in our sample. On the other hand, the value of the R_{xx} peak at low temperature reported in Ref. [118] is one order of magnitude larger than ours. The physical origin for these discrepancies is not known at present and more detailed studies are under course. For our inverted sample C ($d = 13$ nm), similar to normal sample B ($d = 10$ nm), the temperature dependence is weak at $T < 1K$. R_{xx} only becomes strongly activated at higher temperatures of $T > 5K$. Using the Arrhenius fit (Figure 6.4(d)), we deduce the energy gap of 3.1 meV.

6.2.2 Perpendicular and parallel magnetic fields dependence

Perpendicular Magnetic Field

In Figure 6.5 we plotted the longitudinal resistance R_{xx} as a function of the gate voltage in the presence of a perpendicular magnetic field for samples in the three regimes.

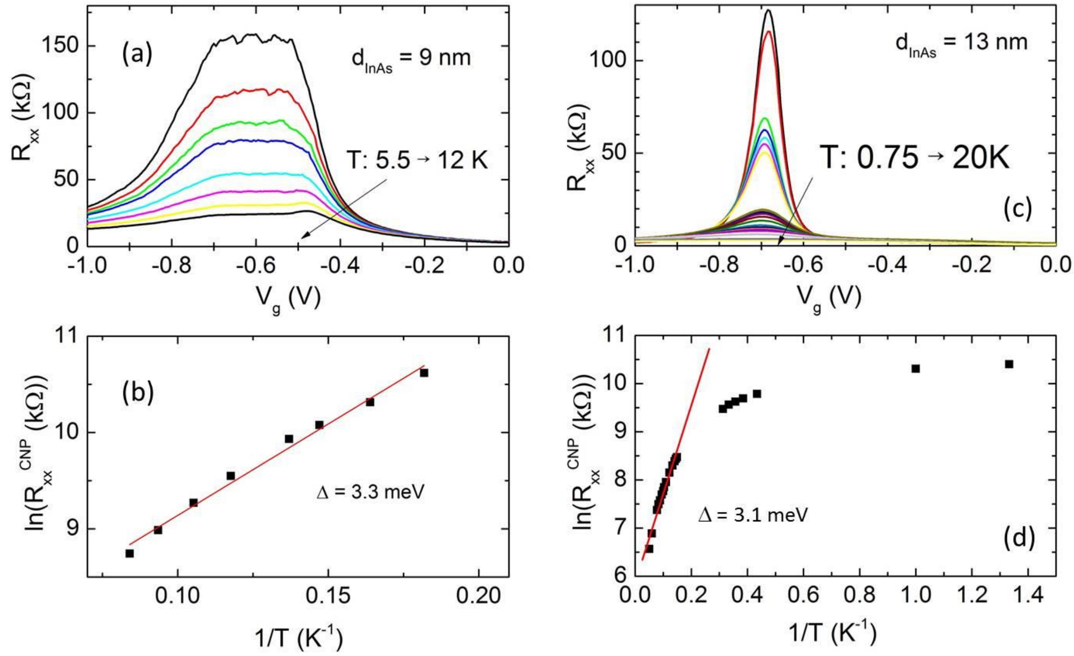

FIGURE 6.4: (Temperature dependence (a) and Arrhenius fit (b) for sample A. The data for sample C are shown in (c) and (d), respectively.

While for both the normal insulator (a) and inverted (c) samples the CNP resistance increases by increasing the perpendicular field, in the critical sample (b) exhibits an unexpected decrease of the CNP resistance up to 2 T. This result could be explained in the frame of the excitonic insulator phase. We estimated a value of 2 meV for the excitonic binding energy in the critical sample as we will report in section 6.5. From the effective masses of InAs and GaSb we have obtained an estimation for the energy band displacements of 2 meV per Tesla. So the observed decrease in resistance value at the CNP for the critical sample (see Figure 6.5 (b)) could be just due to the excitonic phase breaking that should fade out below 2 T.

Parallel magnetic Field

In Figure 6.6 we show the measured longitudinal resistance (R_{xx}) as a function of the gate voltage (V_g) in the presence of a parallel magnetic field for the NI sample d = 9 nm (a), the critical sample d = 10 nm (b), and two inverted

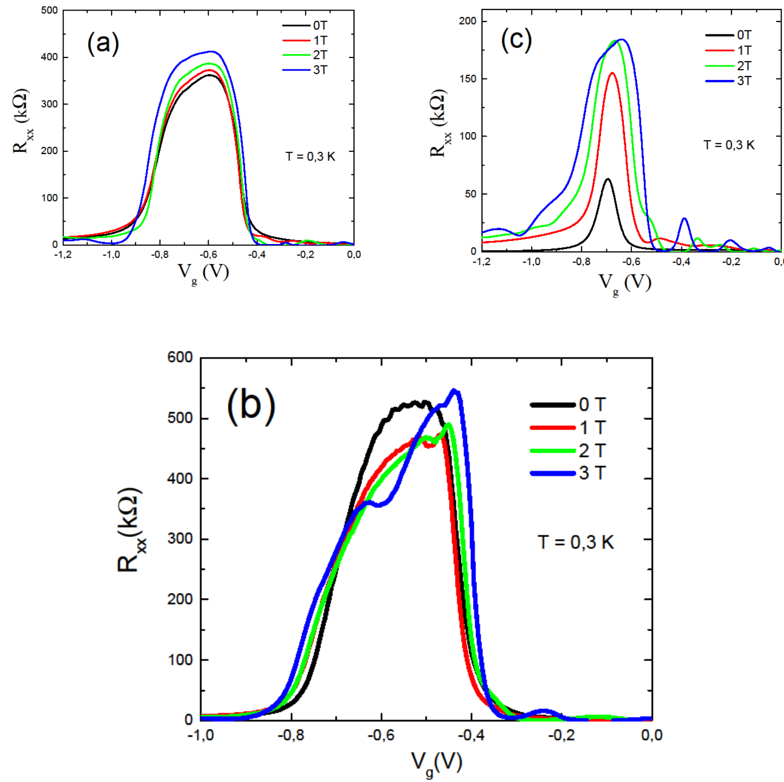

FIGURE 6.5: Longitudinal resistance versus gate voltages at 0.3K from 0 to 3 T perpendicular magnetic field for the normal insulator sample InAs(9nm)/GaSb(5nm) (a), the critical sample 10/5 nm (b) and an inverted sample 13/5 (c). Notice the decrease of the CNP resistance at low magnetic fields up to 2 T for the critical sample whereas in the other two there is always a systematic increase.

samples (c) and (d) with *d* equal to 11 and 13 nm, respectively.

In the CNP, a very strong dependence on the parallel magnetic field appears in the inverted samples whereas it is missing in both the NI and the critical sample. The strong dependence on the parallel magnetic field was expected for an inverted phase [151], so that these data support our theoretical calculations of the respective band structures.

Phenomenological method

Another method for identifying the three different regimes was proposed by Büttner et al.[152] few years ago. These authors showed that the crossing point of the lowest Landau levels for the electron and heavy-hole sub-bands

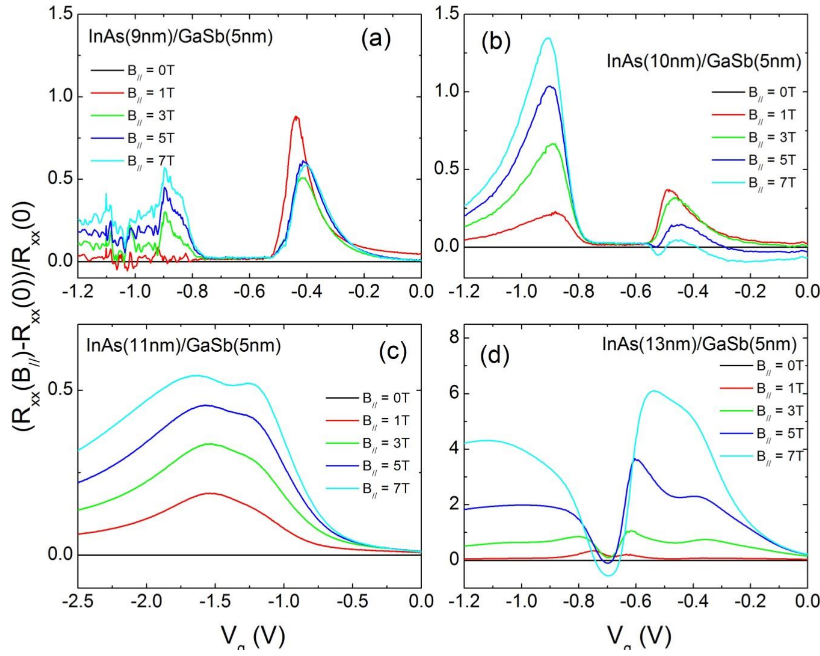

FIGURE 6.6: Longitudinal resistance in parallel magnetic field. Normalized magnetoresistance $\frac{(R_{xx}(B\|)-R_{xx}(0))}{Rxx(0)}$ versus gate voltages in the presence of different parallel magnetic fields for the NI sample (a), critical (b), and two inverted samples (c) and (d). While the NI sample InAs(9 nm)/GaSb(5 nm) and critical sample (10/5 nm) shows almost no parallel magnetic field dependence in the CNP, samples (11/5) nm and (13/5 nm) show a strong field dependence, characteristic of inverted band configurations.

reveals the sample regime; at strong enough perpendicular magnetic fields ($B_\perp > 2T$), a clear plateau in the CNP separates the $\nu = \pm 1$ QH states, and its boundaries, where the magnetic field is strictly an integer number, can be marked by continuous line. From the crossing of these two lines one can identify the system regime. For an inverted system ($Eg < 0$), the crossing point (B_c) should appear at positive magnetic fields ($B_c > 0T$) while for a normal insulator band structure ($Eg > 0$) should appear at negative magnetic fields ($B_c < 0$). Finally, for the critical sample ($Eg = 0$) we should find the crossing point at zero magnetic field ($B_c = 0T$).

In Figure 6.7 it can be observed that our data confirm very well these expectations; in particular, in Figure 6.7(b) we plotted our data for sample B (the critical thickness sample). The crossing point at $B_c = 0T$ demonstrates

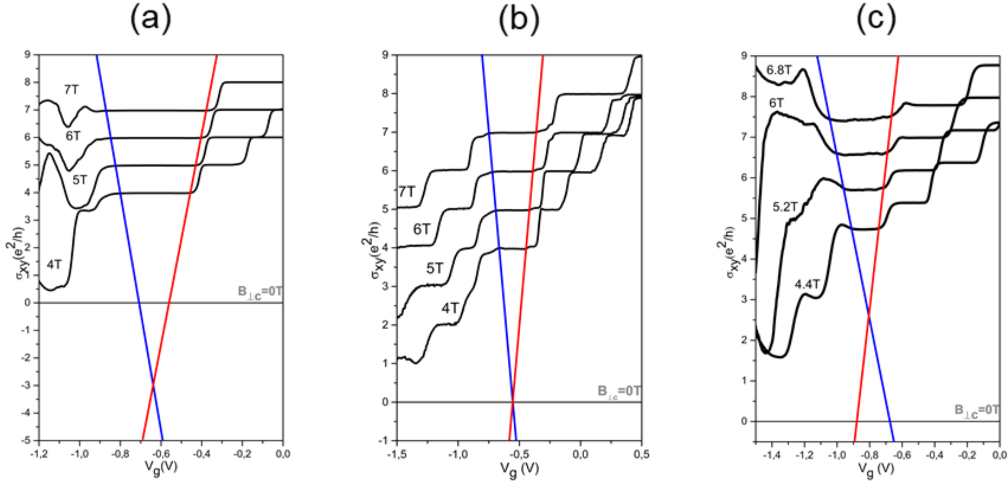

FIGURE 6.7: Hall conductivity (σ_{xy}) at 300 mK at different perpendicular magnetic fields. The blue and red lines, defined by the boundaries of the plateau in the CNR in sample cross at $B_c < 0T$ revealing a normal insulator regime for sample (9/5 nm) (a); in sample (10/5 nm) cross at $B_c \approx 0T$ revealing a zero gap sample (b); finally in sample (13/5 nm) cross at $B_c > 0T$, indicating an inverted regime.

the realization of a zero-gap system, so that the above experimental results are very consistent with our tight-binding simulations.

6.3 Critical sample

In Figure 6.8(a) we plot the longitudinal (σ_{xx}) and Hall (σ_{xy}) conductivities, measured at B = 7 T and T = 100 mK.

Quantized plateaus at filling factors $\nu = 1$ and $\nu = 2$ (as well as at all higher values in the standard integer Quantum Hall sequence, here not shown) are clearly developed for both electrons and holes. In the vicinity of the CNP, an additional plateau at $\sigma_{xy} = 0$ is observed; a similar quantized plateau was reported for an inverted InAs/GaSb sample in Ref. [153], as well as for a degenerate HgTe quantum well in Ref. [152]. In Figure 6.8(b), we show the two-dimensional density of charge carriers for electrons n and holes p as a function of Vg. The experimental points (red and black open circles) were obtained from the position of the integer quantum Hall plateaus

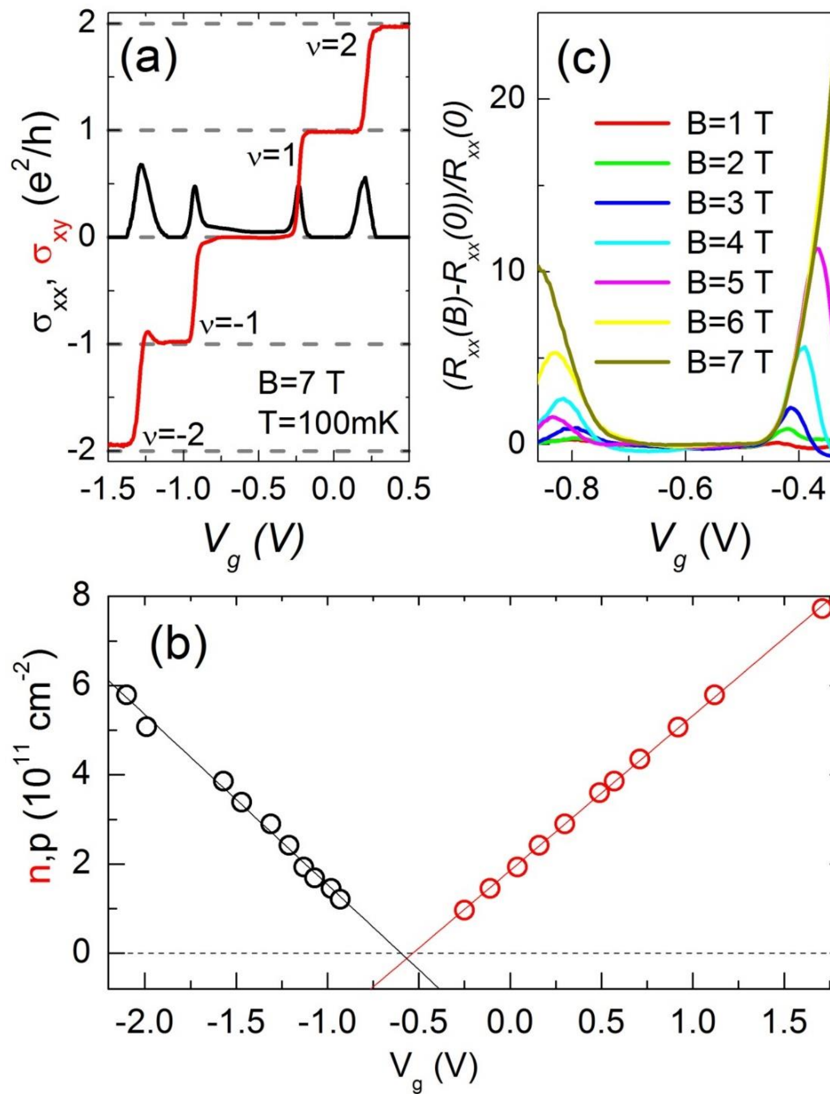

FIGURE 6.8: (a) Longitudinal (σ_{xx}) and Hall (σ_{xy}) conductivities as a function of Vg, measured at B = 7 T. (b) Two-dimensional charge density for electrons n and holes p as a function of Vg. (c) Normalized magnetoresistance ($R_{xx}(B)$)

at several different magnetic fields, while the continuous lines are linear best fits. The lines of the fits cross at Vg = -0.55 V and at $n_0 = p_0 = 1.1 \cdot 10^{10} cm^{-2}$ (which corresponds to the CNP condition n+p = 0). We note here that the obtained electron and hole densities at the CNP are the lowest reported, indicating a high quality of our sample. Figure 6.8(c) shows the normalized magnetoresistance ($\frac{R_{xx}(B)-R_{xx}(0)}{R_{xx}(0)}$) in the CNR at T = 100 mK: zero magnetoresistance is observed up to B = 7 T. Such stability under quantizing magnetic field extends also to its temperature-dependence, as shown in the inset of Figure 6.8(b). Indeed, we observed little differences between the data collected in the range $0T < B < 7T$. These observations strongly differ from those reported for the insulating state at the CNP in Ref. [153], where a huge magnetoresistance accompanied by strong B-induced strengthening of the T-dependence was reported.

6.4 Inverted sample (d=13nm)

A TI (topological insulator) is an electronic material with a bulk gap like an ordinary insulator but they have conducting states on their edges or surface [114]. In this section we report transport measurements on the inverted sample $d = 13$ nm, in which typical features of the topological phase appear. In Figure 6.9(a) the logarithmic longitudinal resistance versus the gate voltage at $B = 0T$ and $T = 50mK$ is shown.

Apart of CNP, that is located in $\approx -0.8V$, two secondary peaks appear around $\approx -1.5V$ and $\approx -0.5V$ in the hole and electron regions respectively. Similar experimental signatures of the inverted phase were find in [120][121]. The reason is due to the Fermi Energy E_F that resides in the valence band (dark green in left side of the CNP) or in the conduction band (light blue in the right side of the CNP) (see inset of Figure 6.9(a)). This peculiar behaviour of the longitudinal resistance are a signature of high quality samples [154]

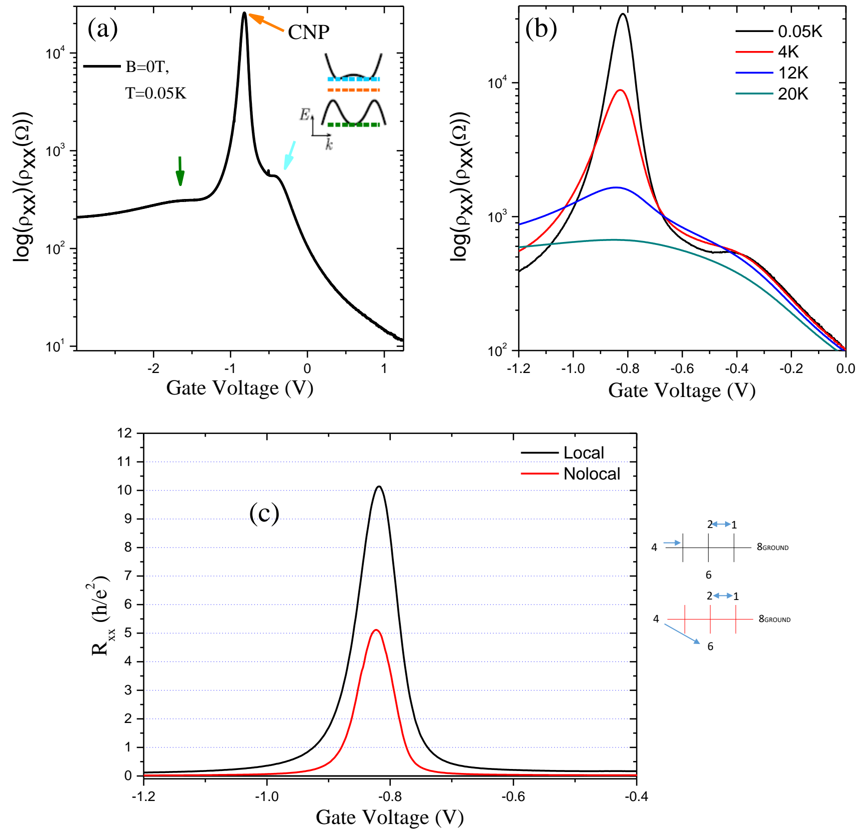

FIGURE 6.9: (a) Logarithmic longitudinal resistance ($\log(\rho_{xx})$) versus the gate voltage. (b) Temperature dependence of the logarithmic longitudinal resistance. (c) Local (black line) and no local (red line) measurements (on the right the schematic configuration).

and interpreted as influence of the energy-dependent density of states on ρ_{xx}.

The strong decay of the CNP and the disappearance of the two secondary peaks with the temperature (Figure 6.9(b)) is also a signature of a possible hybridization gap [120].

In Figure 6.9(c) we report the local (black line) and no local measurement (red line) on the inverted sample with the configuration that is shown on the right of the graph. Electrical transport experiments in local and non-local configurations and the presence of an edge current proved the first realization of the QSH (Quantum Spin Hall) effect in band-inverted HgTe

quantum wells [10][155]. Only some years later the same effect has been recently observed in the InAs/GaSb double quantum well (DQW), a tunable 2D electron-hole system [118].

In Figure 6.10 we report the trasversal resistance with the sweep of the magnetic field, for different gate voltage in the electron (a) and hole (b) side.

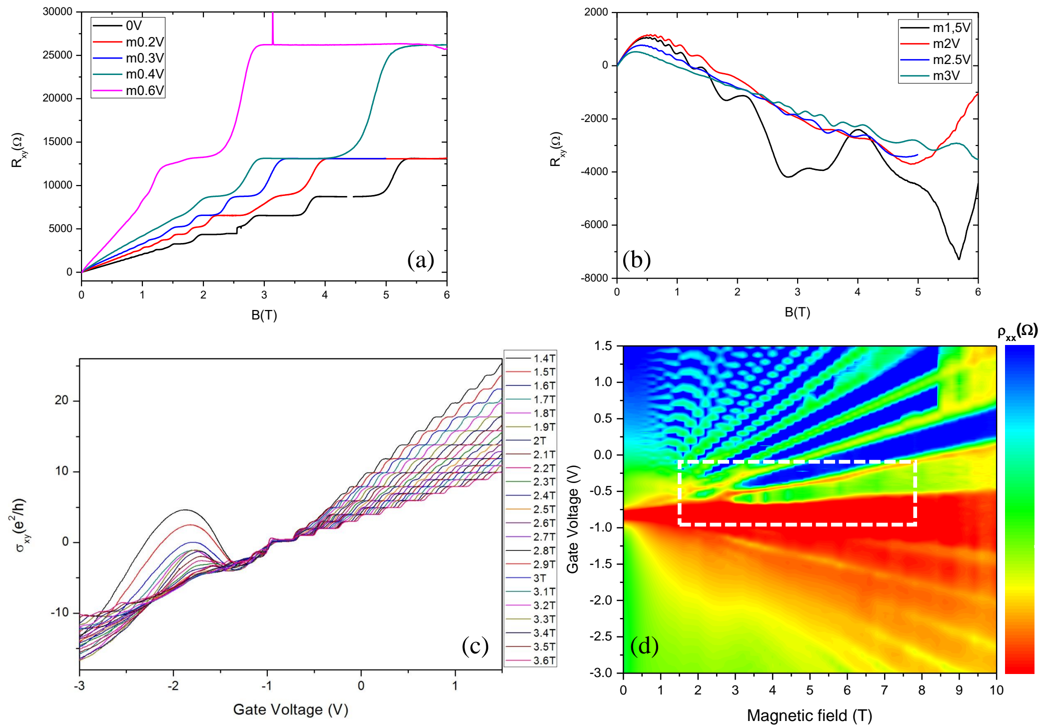

FIGURE 6.10: (a)(b) Trasversal resistance as function of the magnetic field for different value of the gate voltage in the electron (a) and hole (b) region. (c) Trasversal conductance versus gate voltage at different value of magnetic field (d) Colour map of the longitudinal resistivity as function of magnetic field and gate voltage.

A linear behaviour and very defined plateaus appear at the right side of the CNP. The left side instead shows a no-defined behaviour and only at higher magnetic field ($B > 2T$) the sign of the resistance assumes the correct value. In a trivial regime, carriers on either side of the charge neutrality point are either purely electron-like or hole-like, giving rise to a R_{xy} that is linear in B, in either case. The inverted regime, on the other hand, involves an overlap of electron-like and hole-like carriers near the charge neutrality point, giving rise to a R_{xy} that is non-monotonic in B [122]. In fact at gate voltage

lower than the charge neutrality a non-monotonic behavior, that indicates simultaneous transport of electron- and hole-like carriers (Figure 6.10b). This peculiar behaviour due to the hybridization of the gap is visible sweeping the bottom gate voltage for different values of the magnetic field. Meanwhile the 'electron side' shows very well quantized values, in the 'hole side' a mixed regime is evident especially for low magnetic field. In Figure 6.10(d) there is the coloured map of ρ_{xx}. Observing the map ρ_{xx} as a function of V_g and B we find close to the CNP in the electron side, a Landau fan similar to another inverted sample measured in [120] (see highlighted region in Figure 6.10(d)). This modulation of ρ_{xx} is caused by a modulation of energy gaps in the Landau level spectrum and they are another features of the inverted sample. For higher value of the gate voltage instead the minima of ρ_{xx} are evident, defining the different filling factor.

6.5 Discussion

The main result of this Chapter is the observation of an unexpectedly huge resistance peak in the charge neutrality region in a sample where the E_0 and H_0 subbands almost perfectly touch each other at $k = 0$, and a semi-metallic state is nominally expected. Based on this observation, we propose that that the large resistance in the CNP in our critical sample is probably due to the formation of an excitonic insulator phase. When the Fermi level is tuned to the CNP, excitons will form by the attractive Coulomb interactions between residual electrons and holes, whose densities are vanishingly small. At the critical thickness d_c, the band energy gap is almost zero and, thus, smaller than the exciton binding energy E_B, realizing the condition $Eg < E_B$. As predicted more than 50 years ago [123], the excitons under this condition condense, giving rise to an energy gap, which is responsible for the large resistance peak in the CNP. Away from the critical thickness, for $d < 10$

nm, a normal gap $Eg > E_B$ appears (see Figure 6.1(b)). For $d > 10$ nm, the energy band structure becomes inverted. Due to strong interactions between electrons and holes, a mini gap (Δ) is formed at a finite k. At the band edges, the two types of carries coexist. As a result, E_B is much reduced [136]. Consequently the condition $E_B < \Delta$ prevents the formation of exciton condensation. Furthermore, the value of $4n_0a_u^2$ reached in our critical thickness sample also supports the formation of an excitonic insulator phase [136], being a_u the Bohr radius. Using the values quoted in Ref. [156], i.e., effective mass of $m_e = 0.023m_0$ for electrons in InAs and $m_h = 0.33m_0$ for holes in GaSb, and an effective dielectric constant $\kappa \approx 15$, the calculated Bohr radius is $a_u \approx 36.9nm$. With $n_0 = 1.1 \cdot 10^{10}cm^{-2}$, $4n_0a_u^2 \approx 0.6 < 1$, condition at which an excitonic condensed phase was shown to be thermodynamically stable [136]. The existence of an excitonic insulator phase in the critical sample is consistent with recent theoretical calculations [157], where the excitonic insulator phase is shown to be stable for samples with zero band gap and strong inter-layer interactions. Recently in a theoretical study of the charge transport in two-dimensional disordered semimetals by Knap et al.[158], it was found that electron and hole puddles, due to smooth fluctuations of the potential, are responsible for a large resistance peak in the CNP measured in HgTe QWs by Olshanetsky et al. [159] First, we point out that the HgTe QW structure considered in Ref. [159], 20 nm wide, is far from the critical thickness of 6.3 nm in the HgTe QW [152]. As a result, the conduction and valence bands overlap is much greater than the gap estimated in our critical sample. Second, in Ref. [159] the authors found that the resistance at the CNP increases monotonically with decreasing temperature (Figure 3 in Ref. [159]), a behavior different from what we have observed. R_{xx} shows relatively strong magnetic field dependence in Ref. [159] at the temperature considered, which, again, is very different from our observation. Recent work, did not found enhancement in the resistance at the charge neutrality point

[154][160] however the presence of enhancements is markedly dependent on the distance from the critical regime. Finally, in a recent work on InAs/GaSb double-quantum wells [16], the authors also reported on the observation of an excitonic insulating phase, by gating the residual electron and hole density at the CNP towards the diluted regime, which is naturally realized in our nominally zero-gap system. Notably, the activation gap as measured in their most diluted regime matches our value of Δ.

Chapter 7

Conclusion and future perspectives

This thesis starts with a detailed description of the Clean room facilities. The development of the equipment of the Clean Room occupied the larger time of first two years of my PhD studies. In the CR of the University of Salamanca is possible to fabricate different type of devices, even if it was built with a special predisposition for 2D materials devices. For the future, the installation of an equipment for dielectric film deposition as atomic layer deposition (ALD), sputtering or a chemical vapour deposition (CDV) could improve the completeness of the CR. In the past I missed the possibility to deposit dielectric especially when I worked with CVD and epitaxial graphene . In fact when I tried to replace a conventional dielectric film (SiO_2, Al_2O_3, $HfOO_2$) with a resist film (PMMA[61] or Hydrogen silsesquioxane (HSQ) [161]), I found different technical problems, since it was very easy to have cracks and instability with PMMA or having difficulties with the treatment for HSQ.

The fabrication methods for devices based on graphene and other 2D materials represent a very important part of this thesis work so they are also reported in detail. The transfer methods and the fabrication processes (EBL, dry etching, annealing, evaporation) for the realization of "side contacts"have a special role for the fabrication of high quality devices. We described different fabrication processes for devices with different 2D materials (graphene with or without encapsulation in h-BN, epitaxial graphene, CVD graphene, $MoTe_2$, $MoSe_2$). More complex devices, multi-(>4)-layers heterostructures

for vertical transport [162], the realization of a controlled angle between two flakes of graphene with well defined orientation [163], as well devices with different TMDs heterostructures [164] can be achieved in Salamanca in the next future.

Regarding the study of the QHE at room temperature, the difference between encapsulated and no-encapsulated graphene are evident, but we need a more detailed analysis of all the very large data set. In particular it could be necessary a more systematic study on nature on the zero-Landau level, since the behaviour of the zero-level is very different at high magnetic field [165] and high temperatures. In future a larger number of samples of graphene with different substrate could be done for a more quantitative understanding of localization in QHE on graphene at high temperature.

For the GNC, we showed how the new cryo-etching method used in [111] reduces the roughness for the definition of the constriction, achieving quantization and real ballistic transport very close to the ideal one. It will be interesting to study different geometry configuration of nanoconstrictions [110], multiconstrictions transport in ballistic regime as well graphene nanoconstrictions of few nanometers [86] not still achieved into the ballistic regime. For this last aim new test with the Orion NanoFab Helium Ion Microscope can be a possible (even if not easier) solution. The high control on the charge carrier thanks to a well defined channel, makes GNC also an ideal candidates for Terahertz detection [166]. Fabrication and characterization of Terahertz detector based on encapsulated GNC is a purpose for the next future.

The last chapter on InAs/GaSb quantum wells was in reality my first work as PhD student. The comparison between the topological phases in InAs/GaSb quantum wells and graphene nanostructures was one of the intriguing initial aim of this thesis. Even if this purpose did not fulfill for the lack of good InAs/GaSb samples, especially with the hybrid gap, we were able to study samples in different band configuration, observing different

magneto-transport properties and measuring a possible exotic excitonic insulator phase in the critical sample. We are still working on TIs, actually in my group there is another PhD student that is researching on topological phases of different materials ($Pb_{0.77}Sn_{0.23}Se$). For the future we will also continue to study graphene devices and nanostructures with the same purpose, since helical states were theoretically predicted [167][168] and QSHE [169] and magnetic edge states [170] were recently observed in graphene devices.

Appendix A

Resumen

La tesis empieza con una descripción de la Sala blanca de Salamanca y de su equipamiento, instalado durante los primeros años de mi doctorado. Sigue una detallada explicación de los procesos de fabricación de dispositivos en grafeno y otros materiales bidimensionales. En particular el sistema de trasferencia y la realización de contactos de borde tienen un rol fundamental en la realización de dispositivos de alta calidad. En nuestros dispositivos de grafeno encapsulado en nitruro de boro hexagonal hemos observado efecto Hall cuántico (QHE) a temperatura ambiente bajo la aplicación de altos campos magnéticos. El QHE en nuestros dispositivos de alta movilidad tiene características diferentes del QHE en dispositivos de grafeno de baja movilidad. Hemos también estudiado el transporte balístico y casi balístico en constricciones de grafeno con media y alta movilidad. En particular en las constricciones de mayor movilidad hemos introducido un método de definición de la constricción a bajas temperaturas, por la primera vez aplicado a dispositivos de grafeno y que nos han permitido obtener bordes con muy baja rugosidad. Esto ha permitido obtener un comportamiento balístico cerca del ideal y la observación de cuantización de la conductancia. En la última parte de la tesis reportamos medidas de transporte en pozos cuánticos de InAs/GaSb con diferente configuración de bandas (aislante, invertida y crítica). En la muestra crítica hemos encontrado una resistencia longitudinal anormal que

hemos justificado con la posible formación de un excitón en bajas temperaturas.

Appendix B

Conclusiones y Perspectivas

Una descripción detallada del equipamiento de la Sala Blanca de Nanotecnología de la Universidad de Salamanca se presenta al comienzo de la tesis. La instalación y el desarrollo del equipamiento de la Sala Blanca ha ocupado larga parte del tiempo en los primeros dos años de mi doctorado. En el estado actual en la Sala Blanca es posible fabricar diferentes tipo de dispositivos, aunque la sala fue construida con una especial predisposición en la realización de dispositivos bidimensionales. Para el futuro, la instalación de algún equipo para deposición de dieléctricos (deposición de capa atómica (ALD), pulverización catódica o deposición química de vapor (CVD)) podría aumentar mucho las posibilidades de fabricación.

La fabricación de dispositivos basados en grafeno y otros materiales 2D representa un importante parte de mi trabajo doctoral. La trasferencia de los materiales 2D y el resto de proceso de fabricación (litografía electrónica, ataque físico, recocido y evaporación) tienen un rol muy importante para la realización de dispositivos de alta calidad. En la tesis hemos describito diferentes procesos de fabricación para los diferentes materiales 2D usados (grafeno con y sin nitruro de boro hexagonal, grafeno epitaxial, grafeno de diselenurio de molibdeno y ditelurio de molibdeno). Para el futuro pensamos realizar dispositivos con heteroestructuras con más de cuatro capas para el trasporte vertical, dispositivos con dos capas de grafeno con cierta orientación fijada así como dispositivos basados en heteroestructuras con otros

materiales 2D.

En el Capitulo 4 hemos estudiado el efecto Hall cuático (QHE) a altas temperaturas y altos campos magnéticos sobre dispositivos de grafeno encapsulado y no encapsulado en nitruro de boro hexagonal. Las diferencias en las medidas son evidentes en particular en la naturaleza del cero nivel de Landau. Para el futuro un numero de dispositivos mas grande y variado podría ser útil a completar el trabajo realizado y así tener una comprensión más cuantitativa de la localización en el QHE en grafeno a altas temperaturas.

En el capitulo 5 hemos estudiado constricciones de grafeno balísticas y quasi balísticas y hemos describito una nueva técnica de ataque en frio para definir las constricciones sobre grafeno encapsulado en nitruro de boro hexagonal con muy baja rugosidad. La definición es tan buena que comportamiento balístico de dichas constricciones está cerca del ideal. Sería interesante estudiar para el futuro constricciones con diferentes geometrías, trasporte en multiconstricciones o en constricciones de pocos nanómetros, donde todavía no se ha conseguido un comportamiento balístico. Para esta última finalidad la utilización del Orion Nanofab que usa átomos de helio para definir con resolución muy alta las nanoconstricciones de grafeno, sería la solución más congenial. Constricciones de grafeno encontrarían también una aplicación como detectores para el terahercios y este es otro nuestros ojetivos del próximo futuro.

En el último capítulo hemos estudiado sistemas de InAs/GaSb pozos cuánticos que han sido en realidad mi primer trabajo como estudiante de doctorado. La comparación de la fase topológica en estos sistemas y nanoestructuras de grafeno ha sido el propósito inicial de esta tesis. La falta de dispositivos de InAs/GaSb, especialmente en la fase hibrida, ha limitado mucho las intenciones iniciales, pero hemos sido capaz de observar diferentes propriedades de magnetotransporte en estos sistemas con diferentes

configuraciones, así como observar un posible nuevo estado exótico excitonico en la muestra crítica.

Appendix C

List of publications

- J. A. Delgado Notario, **V. Clericò**, E. Diez, J. E. Velazquez, T. Taniguchi, K. Watanabe, T. Otsuji and Y. M. Meziani "Asymmetric Dual Grating Gates GrapheneFET for Detection of Terahertz Radiations" *subm. to NanoLett.*

- **V. Clericò**, J. A. Delgado Notario, M. Saiz-Bretín, A. V. Malyshev, Y. Meziani, P. Hildago, M. Bianchi, M. Amado, F. Domínguez-Adame and E. Diez "Quantum nanoconstrictions fabricated by cryo-etching in encapsulated graphene" *Sci. Rep.* **9**, 13572, 2019.

- J. A. Delgado Notario, **V. Clericò**, K. Fobelets, J. E. Velázquez-Pérez, Y. M. Meziani "Room-Temperature Terahertz Detection and Imaging by Using Strained-Silicon MODFETs" *Design, Simulation and Construction of Field Effect Transistors*, IntechOpen, 2018.

- W. Yu, **V. Clericò**, C. Hernández Fuentevilla, X. Shi, Y. Jiang, D. Saha, W. K. Lou, K. Chang, D. H. Huang, G. Gumbs, D. Smirnov, C. J. Stanton, Z. Jiang, V. Bellani, Y. Meziani, E. Diez, W. Pan, S. D. Hawkins and J. F. Klem "Anomalously large resistance at the charge neutrality point in a zero-gap InAs/GaSb bilayer" *New J. Phys.* **20**, 053062, 2018.

- **V. Clericò**, J. A. Delgado Notario, M. Saiz-Bretín, C. Hernández Fuentevilla, A. V. Malyshev, J. D. Lejarreta, E. Diez and Domínguez-Adame, F. "Quantized Electron Transport Through Graphene Nanoconstrictions" *Phys. Stat. Solidi A* **215**, 1701065, 2018.

Appendix D

Conference Proceedings and Oral Contribution

- J. A. Delgado Notario, E. Javadi, **V. Clericò**, K. Fobelets, T. Otsuji, E. Diez, J. E. Velazquez and Y. M. Meziani "Experimental and theoretical studies of Sub-THz detection using strained-Si FETs" *Journal of Physics: Conference Series* **906(1)**, 012003, 2016.

- **V. Clericò**, J. A. Delgado Notario, N. Campos, D. Gómez, E. Diez, J. E. Velazquez and Y. M. Meziani "Terahertz spectroscopy of a multilayers flake of graphene" *Journal of Physics: Conference Series* **647(1)**, 012040, 2015.

- *Quantum nanoconstrictions fabricated by cryo-etching in encapsulated graphene*, **Edison21 (The 21st International Conference on Electron Dynamics in Semiconductors, Optoelectronics and Nanostructures)**, 14-19/07/2019, Nara (Japan).

- *Conductance quantization in ballistic graphene nanoconstrictions*, **CDE 2018 (12th Spanish Conference on Electron Devices)**, 14-16/11/2018, Salamanca (Spain).

- *Coherent electron transport through graphene nanoconstrictions and nanoribbons*, **Graphene 2018**, 26-29/06/2018, Dresden (Germany).

- *Fabrication and characterization of Graphene and Graphene Oxide/hBN heterostructures*, **Nanolito2017 (Nanodevices based on graphene and 2D materials)**, 25-26/01/2017 Salamanca (Spain).

- *Transport properties of degenerate InAs/GaSb quantum wells* (Best Poster Awards), **Edison19 (The 19th International Conference on Electron Dynamics in Semiconductors)**, 29/06/15-02/07/15, Salamanca (Spain).

Appendix E

Funding received

I wish to acknowledge Junta Castilla y León for the first contract as technician (técnico de apoyo a la investigación, 2013) to install the Clean room facilities and for the fellowship as PhD Student (contractos predoctorales de la Junta Castilla y León, 2015-2019).

The PhD has also financially supported by the following research grants:

- Tecnologías basadas en materiales híbridos avanzados:grafeno, materiales 2D y aislantes topológicos, Junta Castilla y Leon (SA256P18), 2019-2021
- TRANSNANO: Fabricación y estudio de las propiedades de transporte de nanodispositivos basados en grafeno y materiales híbridos avanzados, Mineco (MAT2016-75955-C2-2-R), 2016-2019
- Nuevas tecnología basadas en grafeno y nanoestructuras semiconductoras Junta Castilla y Leon, (SA045U16), 2016-2018
- Diseño, fabricación y caracterización de nanodispositivos electrónicos bidimensionales Mineco (MAT2013-46308-C2-1R), 2014-2017
- Nanoestructuras electrónicas en grafeno y otros materiales y sus aplicaciones en la tecnología de terahercios, Junta Castilla y Leon, (SA226U13), 2013-2016

Bibliography

[1] T.O. Wehling, A.M. Black-Schaffer, and A.V. Balatsky. "Dirac materials". In: *Advances in Physics* 63 (2014), p. 1. DOI: 10.1080/00018732.2014.927109 (cit. on pp. 1, 2).

[2] J. Cayssol. "Introduction to Dirac materials and topological insulators". In: *C.R. Physique* 14 (2013), p. 760. DOI: 10.1016/j.crhy.2013.09.012 (cit. on p. 1).

[3] A. Díaz-Fernández et al. "Tuning the Fermi velocity in Dirac materials with an electric field". In: *Sci. Rep.* 7 (2017), p. 8058. DOI: 10.1038/s41598-017-08188-3 (cit. on p. 2).

[4] K. S. Novoselov et al. "Room-Temperature Quantum Hall Effect in Graphene". In: *Science* 315 (2007), p. 1379. DOI: 10.1126/science.1137201 (cit. on pp. 2, 3, 80, 86–88, 93).

[5] C. R. Dean et al. "Multicomponent fractional quantum Hall effect in graphene". In: *Nat. Phys.* 7 (2011), p. 693. DOI: 10.1038/nphys2007 (cit. on pp. 2, 93).

[6] N. Tombros et al. "Quantized conductance of a suspended graphene nanoconstriction". In: *Nat.Phys.* 7 (2011), p. 697. DOI: 10.1038/NPHYS2009 (cit. on pp. 2, 95, 101).

[7] L. Vicarelli et al. "Graphene field-effect transistors as room-temperature terahertz detectors". In: *Nat. Mater.* 11 (2012), p. 865. DOI: 10.1038/NMAT3417 (cit. on pp. 2, 66).

[8] W. Han et al. “Graphene spintronics”. In: *Nature Nanotech.* 9 (2014), p. 794. DOI: 10.1038/nnano.2014.214 (cit. on p. 2).

[9] Y. Cao et al. “Unconventional superconductivity in magic-angle graphene superlattices”. In: *Nature* 556 (2018), p. 43. DOI: 10.1038/nature26160 (cit. on p. 2).

[10] M. König et al. “Quantum Spin Hall Insulator State in HgTe Quantum Wells”. In: *Science* 218 (2007), p. 766. DOI: 10.1126/science.1148047 (cit. on pp. 2, 132).

[11] G.E. Moore. “Cramming more components onto integrated circuits”. In: *Electronics* 38 (1965), p. 114 (cit. on p. 2).

[12] B. J. van Wees et al. “Quantized conductance of point contacts in a two-dimensional electron gas”. In: *Phys. Rev. Lett.* 60 (1988), p. 848. DOI: 10.1103/PhysRevLett.60.848 (cit. on p. 3).

[13] H. van Houten and C.W.J. Beenakker. “Quantum point contacts”. In: *Physics Today* 49 (1996), p. 22. DOI: 10.1063/1.881503 (cit. on p. 3).

[14] D. A. Wharam et al. “One-dimensional transport and the quantization of the ballistic resistance”. In: *J. Phys. C.* 21 (1988), p. L209. DOI: 10.1088/0022-3719/21/8/002 (cit. on p. 3).

[15] C.C.Dean and M. Pepper. “The transition from two- to one-dimensional electronic transport in narrow silicon accumulation layers”. In: *J. Phys. C.* 15 (1986), p. L1287. DOI: 10.1088/0022-3719/15/36/005 (cit. on p. 3).

[16] L. Du et al. “Gate-tuned spontaneous exciton insulator in double-quantum wells”. In: *Nat. Comm.* 8 (2017), p. 1971. DOI: 10.1038/s41467-017-01988-1 (cit. on pp. 3, 135).

[17] K.J. Franke and F. von Oppen. "Topological states engineered in narrow strips of graphene". In: *Nature* 175 (2018), p. 660. DOI: 10.1038/d41586-018-05851-1 (cit. on p. 3).

[18] A. Alymani and O. M. Lemine. "FE-SEM Characterization of Some Nanomaterial". In: *Scanning Electron Microscope* (2012) (cit. on p. 10).

[19] Vermeulen J.P. "12 years Zeiss Gemini FESEM technology". In: *ImagingMicroscopy* 4 (2004) (cit. on p. 10).

[20] P. Rai-Choudhury. *Handbook of Microlithography, Micromachining, and Microfabrication. Volume 1: Microlithography*. SPIE, 1997. DOI: 10.1117/3.2265070 (cit. on p. 14).

[21] C. J. Docherty and M. B. Johnston. "Terahertz Properties of Graphene". In: *J Infrared Milli Terahz Waves* 33 (2012), p. 797. DOI: 10.1007/s10762-012-9913-y (cit. on p. 39).

[22] V. Clericò et al. "Terahertz spectroscopy of a multilayers flake of graphene". In: *Journal of Physics: Conference Series* 647 (2015), p. 012040. DOI: 10.1088/1742-6596/647/1/012040 (cit. on p. 39).

[23] J.L. Tomaino et al. "Terahertz imaging and spectroscopy of large-area single-layer graphene". In: *Optics Express* 19 (2011), p. 141. DOI: 10.1364/OE.19.000141 (cit. on p. 39).

[24] M.Yin and Z. Shen. "A review on mechanical exfoliation for the scalable production of graphene". In: *Journal of Materials Chemistry A* 3 (2015), p. 11700. DOI: 10.1039/C5TA00252D (cit. on p. 46).

[25] K. S. Novoselov et al. "Electric Field Effect in Atomically Thin Carbon Films". In: *Science* 306 (2004), p. 666. DOI: 10.1126/science.1102896 (cit. on p. 46).

[26] C. R. Dean et al. “Boron nitride substrates for high-quality graphene electronics”. In: *Nat. Nanotechnol.* 5 (2010), p. 722. DOI: 10.1038/nnano.2010.172 (cit. on pp. 46, 93).

[27] P. J. Zomer et al. “Fast pick up technique for high quality heterostructures of bilayer graphene and hexagonal boron nitride”. In: *Appl. Phys. Lett.* 105 (2014), p. 013101. DOI: 10.1063/1.4886096 (cit. on pp. 46, 53).

[28] S. S. Varghese et al. “Recent advances ingraphene based gas sensors”. In: *Sensors and Actuators B: Chemical* 218 (2015), p. 160. DOI: 10.1016/j.snb.2015.04.062 (cit. on p. 47).

[29] F. Pizzocchero et al. “The hot pick-up technique for batch assembly of van der Waals heterostructures”. In: *Nat. Comm.* 7 (2016), p. 11894. DOI: 10.1038/ncomms11894 (cit. on pp. 47, 57, 62).

[30] J. M. Caridad et al. “Effects of particle contamination and substrate interaction on the Ramanresponse of unintentionally doped graphene”. In: *J. Appl. Phys.* 108 (2010), p. 084321. DOI: 10.1063/1.3500295 (cit. on p. 48).

[31] M. Lafkioti et al. “Graphene on a Hydrophobic Substrate:Doping Reduction and Hysteresis Suppression under Ambient Conditions”. In: *Nano Lett* 10 (2010), p. 1149. DOI: 10.1021/nl903162a (cit. on pp. 48, 98).

[32] Sk. F. Chowdhury et al. “Improvement of graphene field-effect transistors by hexamethyldisilazane surface treatment”. In: *Appl. Phys. Lett.* 105 (2014), p. 033177. DOI: 10.1063/1.4891364 (cit. on pp. 48, 98).

[33] I. Jung et al. “Simple Approach for High-Contrast Optical Imaging and Characterization of Graphene-Based Sheets”. In: *Nano.Lett* 7 (2007), p. 3569. DOI: 10.1021/nl0714177 (cit. on p. 48).

[34] A. Das et al. "Monitoring dopants by Raman scattering in an electrochemically top-gated graphene transistor". In: *Nat.Nanotech.* 3 (2008), p. 210. DOI: 10.1038/nnano.2008.67 (cit. on p. 49).

[35] B.K. Min et al. "AC-Impedance Spectroscopic Analysis on the Charge Transport in CVD-Grown Graphene Devices with Chemically Modified Substrates". In: *ACS Appl. Mater. Interfaces* 8 (2016), p. 27421. DOI: 10.1021/acsami.6b03705 (cit. on p. 49).

[36] D. G. Purdie et al. "Cleaning interfaces in layered materials heterostructures". In: *Nat. Comm.* 9 (2018), p. 5387. DOI: 10.1038/s41467-018-07558-3 (cit. on p. 53).

[37] H. Overweg et al. "Electrostatically Induced Quantum Point Contacts in Bilayer Graphene". In: *Nano Lett.* 18 (2018), p. 553. DOI: 10.1021/acs.nanolett.7b04666 (cit. on pp. 56, 96, 110).

[38] L. Britnell et al. "Electron Tunneling through Ultrathin Boron Nitride Crystalline Barriers". In: *Nano. Lett.* 3 (2012), p. 1707. DOI: 10.1021/nl3002205 (cit. on p. 57).

[39] A. C. Ferrari et al. "Raman Spectrum of Graphene and Graphene Layers". In: *Phys.Rev.Lett.* 97 (2006), p. 187401. DOI: 10.1103/PhysRevLett.97.187401 (cit. on p. 61).

[40] S. Berciaud et al. "Probing the Intrinsic Properties of Exfoliated Graphene: Raman Spectroscopy of Free-Standing Monolayers". In: *Nano Lett.* 9 (2009), p. 346. DOI: 10.1021/nl8031444 (cit. on p. 61).

[41] C. Neumann et al. "Raman spectroscopy as probe of nanometre-scale strain variations in graphene". In: *Nat. Comm.* 6 (2015), p. 8429. DOI: 10.1038/ncomms9429 (cit. on p. 62).

[42] A. C. Ferrari. "Raman spectroscopy of graphene and graphite: Disorder, electron–phonon coupling, doping and nonadiabatic effects". In:

Solid State Communications 143 (2007), p. 47. DOI: 10.1016/j.ssc.2007.03.052 (cit. on p. 62).

[43] R. Frisenda et al. "Recent progress in the assembly of nanodevices and van der Waals heterostructures by deterministic placement of 2D materials". In: *Chem. Soc. Rev.* 47 (2018), p. 53. DOI: 10.1039/C7CS00556C (cit. on p. 63).

[44] D. Yadav et al. "Terahertz wave generation and detection in double-graphene layered van der Waals heterostructures". In: *2D Mater.* 3 (2016), p. 045009. DOI: 10.1088/2053-1583/3/4/045009 (cit. on p. 66).

[45] T. Watanabe et al. "Ultrahigh sensitive plasmonic terahertz detector based on an asymmetric dual-grating gate HEMT structure". In: *Solid State Electronics* 78 (2012), p. 109. DOI: 10.1016/j.sse.2012.05.047 (cit. on p. 67).

[46] R. Degl'Innocenti et al. "Fast Room-Temperature Detection of Terahertz Quantum Cascade Lasers with Graphene-Loaded Bow-Tie Plasmonic Antenna Arrays". In: *ACS Photonics* 3 (2016), p. 1747. DOI: 10.1021/acsphotonics.6b00405 (cit. on p. 67).

[47] P. Sutter. "How silicon leaves the scene". In: *Nat. Mater.* 8 (2009), p. 171. DOI: 10.1038/NMAT3417 (cit. on pp. 67, 68).

[48] L. Banszerus et al. "Ultrahigh-mobility graphene devices from chemical vapor deposition on reusable copper". In: *Sci. Adv.* 1 (2015), e1500222. DOI: 10.1126/sciadv.1500222 (cit. on p. 67).

[49] D. Waldmann et al. "Bottom-gated epitaxial graphene". In: *Nat. Mater.* 10 (2011), p. 357. DOI: 10.1038/NMAT2988 (cit. on p. 70).

[50] B. Jouault et al. "Quantum Hall effect in bottom-gated epitaxial graphene grown on the C-face of SiC". In: *Appl. Phys. Lett.* 100 (2012), p. 052102. DOI: 10.1063/1.3680564 (cit. on p. 70).

[51] C. P. Puls et al. "Top-gate dielectric induced doping and scattering of charge carriers in epitaxial graphene". In: *Appl. Phys. Lett.* 99 (2011), p. 013103. DOI: 10.1063/1.3607284 (cit. on p. 70).

[52] P. Wehrfritz et al. "Quasi-freestanding epitaxial graphene transistor with silicon nitride top gate". In: *J. Phys. D: Appl. Phys.* 47 (2014), p. 305103. DOI: 10.1088/0022-3727/47/30/305103 (cit. on p. 70).

[53] A. T. Neal et al. "Electronic Transport Properties in Top-gated Epitaxial Graphene on Silicon Carbide with ALD Al2O3 High-k Dielectric". In: *Micro/Nano Symposium (UGIM), 2010 18th Biennial University/ Government/Industry; IEEE: New York, 2010* (). DOI: 10.1109/UGIM.2010.5508904 (cit. on p. 70).

[54] H. Sediri et al. "Atomically Sharp Interface in an h-BN-epitaxial graphene van der Waals Heterostructure". In: *Sci. Rep.* 5 (2015), p. 16465. DOI: 10.1038/srep16465 (cit. on p. 70).

[55] A. Reina et al. "Large Area, Few-Layer Graphene Films on Arbitrary Substrates by Chemical Vapor Deposition". In: *Nano. Lett.* 9 (2009), p. 30. DOI: 10.1021/nl801827v (cit. on p. 72).

[56] Z.Y. Juang et al. "Graphene synthesis by chemical vapor deposition and transfer by a roll-to-roll process". In: *Carbon* 30 (2010), p. 3169. DOI: 10.1016/j.carbon.2010.05.001 (cit. on p. 72).

[57] J. W. Suk et al. "Transfer of CVD-Grown Monolayer Graphene onto Arbitrary Substrates". In: *ACS nano* 5 (2011), p. 6916. DOI: 10.1021/nn201207c (cit. on p. 72).

[58] R. Parthiban D. J. Carbaugh J. T. Wright and F. Rahman. "Photolithography with polymethyl methacrylate (PMMA)". In: *Semicond. Sci. Technol.* 31 (2016), p. 025010. DOI: 10.1088/0268-1242/31/2/025010 (cit. on p. 72).

[59] K. S. Novoselov et al. "Two-dimensional atomic crystals". In: *PNAS* 30 (2005), p. 102. DOI: 10.1073pnas.0502848102 (cit. on p. 73).

[60] S. Manzeli et al. "2D transition metal dichalcogenides". In: *Nature Reviews Materials* 2 (2017), p. 17033. DOI: 10.1038/natrevmats.2017.33 (cit. on p. 74).

[61] A. Roy et al. "Structural and Electrical Properties of MoTe2 and MoSe2 Grown by Molecular Beam Epitaxy". In: *ACS Appl. Mater. Interfaces* 2 (2016), p. 7396. DOI: 10.1021/acsami.6b00961 (cit. on pp. 74, 137).

[62] L. D. N. Mouafo et al. "Tuning contact transport mechanisms in bilayer MoSe2 transistors up to Fowler–Nordheim regime". In: *2D Materials* 4 (2017), p. 015037. DOI: 10.1088/2053-1583/aa50d0 (cit. on p. 75).

[63] P. Tonndorf et al. "Photoluminescence emission and Raman response of monolayer MoS2, MoSe2, and WSe2". In: *Optics Express* 21 (2013), p. 4908. DOI: 10.1364/OE.21.004908 (cit. on p. 75).

[64] H Huang et al. "Highly sensitive visible to infrared MoTe2 photodetectors enhanced by the photogating effect". In: *Nanotechnology* 27 (2016), p. 445201. DOI: 10.1088/0957-4484/27/44/445201 (cit. on p. 76).

[65] Y.-F. Lin et al. "Ambipolar MoTe 2 Transistors and Their Applications in Logic Circuits". In: *Adv. Mater.* 26 (2014), p. 3263. DOI: 10.1002/adma.201305845 (cit. on p. 77).

[66] K. v. Klitzing, G. Dorda, and M. Pepper. "New Method for High-Accuracy Determination of the Fine-Structure Constant Based on Quantized Hall Resistance". In: *Phys. Rev. Lett.* 45 (1980), p. 494. DOI: 10.1103/PhysRevLett.45.494 (cit. on p. 79).

[67] K. S. Novoselov et al. “Two-dimensional gas of massless Dirac fermions in graphene”. In: *Nature* 438 (2005), p. 197. DOI: 10.1038/nature04233 (cit. on pp. 79, 91).

[68] T. Khouri et al. “High-temperature quantum Hall effect in finite gapped HgTe quantum wells”. In: *Phys. Rev. B* 93 (2016), p. 125308. DOI: 10.1103/PhysRevB.93.125308 (cit. on p. 80).

[69] K. I. Bolotin et al. “Temperature-Dependent Transport in Suspended Graphene”. In: *Phys. Rev. Lett.* 101 (2008), p. 096802. DOI: 10.1103/PhysRevLett.101.096802 (cit. on pp. 82, 91).

[70] E. H. Hwang and S. Das Sarma. “Acoustic phonon scattering limited carrier mobility in two-dimensional extrinsic graphene”. In: *Phys. Rev. B* 77 (2008), p. 115449. DOI: 10.1103/PhysRevB.77.115449 (cit. on p. 82).

[71] F. Amet et al. “Composite fermions and broken symmetries in graphene”. In: *Nat.Comm.* 6 (2015), p. 5838. DOI: 10.1038/ncomms6838 (cit. on p. 82).

[72] N. J. G. Couto et al. “Random Strain Fluctuations as Dominant Disorder Source for High-Quality On-Substrate Graphene Devices”. In: *Phys. Rev. X* 4 (2014), p. 041019. DOI: 10.1103/PhysRevX.4.041019 (cit. on pp. 83–85).

[73] S. Kim et al. “Realization of a high mobility dual-gated graphene field-effect transistor with dielectric”. In: *Appl.Phys.Lett.* 94 (2009), p. 062107. DOI: 10.1063/1.3077021 (cit. on pp. 83, 100).

[74] L.Gammelgaard et al. “Graphene transport properties upon exposure to PMMA processing and heat treatments”. In: *2D Materials* 1 (2014), p. 035005. DOI: 10.1088/2053-1583/1/3/035005 (cit. on pp. 83, 100).

[75] A. H. Castro Neto et al. “The electronic properties of graphene”. In: *Rev. Mod. Phys.* 81 (2009), p. 109. DOI: 10.1103/RevModPhys.81.109 (cit. on p. 84).

[76] F. D. M. Haldane. “Model for a Quantum Hall Effect without Landau Levels: Condensed-Matter Realization of the "Parity Anomaly"”. In: *Phys. Rev. Lett* 61 (1988), p. 2015. DOI: 10.1103/PhysRevLett.61.2015 (cit. on pp. 90, 115).

[77] A. J. M. Giesbers et al. “Quantum-Hall Activation Gaps in Graphene”. In: *Phys. Rev. Lett* 99 (2007), p. 206803. DOI: 10.1103/PhysRevLett.99.206803 (cit. on pp. 90, 94).

[78] B. Huckestein. “Scaling theory of the integer quantum Hall effec”. In: *Rev. Mod. Phys.* 67 (1995), p. 357. DOI: 10.1103/RevModPhys.67.35 (cit. on p. 91).

[79] A. J. M. Giesbers et al. “Scaling of the quantum Hall plateau-plateau transition in graphene”. In: *Phys. Rev. B* 80 (2009), 241411(R). DOI: 10.1103/PhysRevB.80.241411 (cit. on pp. 91, 94).

[80] D. C. Tsui, H. L. Stormer, and A. C. Gossard. “Two-Dimensional Magnetotransport in the Extreme Quantum Limit”. In: *Phys. Rev. Lett.* 48 (1982), p. 1559. DOI: 10.1103/PhysRevLett.48.1559 (cit. on p. 91).

[81] A. Kou et al. “Electron-hole asymmetric integer and fractional quantum Hall effect in bilayer graphene”. In: *Science* 345 (2013), p. 6192. DOI: 10.1126/science.1250270 (cit. on p. 93).

[82] D. Bischoff et al. “Characterizing wave functions in graphene nanodevices: Electronic transport through ultrashort graphene constrictions on a boron nitride substrate”. In: *Phys.Rev.B* 90 (2014), p. 155405. DOI: 10.1103/PhysRevB.90.115405 (cit. on pp. 95, 103).

[83] A. Celis et al. "Graphene nanoribbons: fabrication, properties and devices". In: *J. Phys. D: Appl. Phys.* 49 (2016), p. 143001. DOI: 10.1088/0022-3727/49/14/143001 (cit. on p. 95).

[84] W. J. Yu and X. Duan. "Tunable transport gap in narrow bilayer graphene nanoribbons". In: *Scientific Reports* 3 (2013), p. 1248. DOI: 10.1038/srep01248 (cit. on p. 95).

[85] K. Nakada et al. "Edge state in graphene ribbons: Nanometer size effect and edge shape dependence". In: *Phys.Rev.B* 54 (1996), p. 17954. DOI: doi.org/10.1103/PhysRevB.54.17954 (cit. on p. 95).

[86] P. Gehring et al. "Quantum Interference in Graphene Nanoconstrictions". In: *Nano Lett.* 16 (2016), p. 4210. DOI: 10.1021/acs.nanolett.6b01104 (cit. on pp. 95, 99, 138).

[87] D. J. Rizzo et al. "Topological band engineering of graphene nanoribbons". In: *Nature* 560 (2018), p. 204. DOI: 10.1038/s41586-018-0376-8 (cit. on p. 95).

[88] B. Terrés et al. "Size quantization of Dirac fermions in graphene constrictions". In: *Nat. Commun.* 7 (2016), p. 11528. DOI: 10.1038/ncomms11528 (cit. on pp. 95, 96, 99, 100, 103, 107, 108).

[89] M. Kim et al. "Valley-symmetry-preserved transport in ballistic graphene with gate-defined carrier guiding". In: *Nat. Phys.* 12 (2016), p. 1022. DOI: 10.1038/NPHYS2009 (cit. on pp. 95, 96, 110).

[90] H. Lee et al. "Edge-Limited Valley-Preserved Transport in Quasi-1D Constriction of Bilayer Graphene". In: *Nano Lett.* 18 (2018), p. 5961. DOI: 10.1021/acs.nanolett.8b02750 (cit. on pp. 96, 110, 111).

[91] P. R. Wallace. "The Band Theory of Graphite". In: *Phys. Rev.* 71 (1947), p. 622. DOI: 10.1103/PhysRev.71.622 (cit. on p. 97).

[92] A. H. Castro Neto et al. "The electronic properties of graphene". In: *Rev. Mod. Phys.* 81 (2009), p. 109. DOI: 10.1103/RevModPhys.81.109 (cit. on p. 97).

[93] S. Reich, Maultzsch, and C. Thomsen. "Tight-binding description of graphene". In: *Physical Review B* 66 (2002), p. 035412. DOI: 10.1103/PhysRevB.66.035412 (cit. on p. 97).

[94] S. V. Morozov et al. "Giant Intrinsic Carrier Mobilities in Graphene and Its Bilayer". In: *Phys. Rev. Lett.* 100 (2008), p. 016602. DOI: 10.1103/PhysRevLett.100.016602 (cit. on p. 97).

[95] I. Milosević et al. "Electron-phonon coupling in graphene". In: *Int. J. Mod. Phys. B* 24 (2010), p. 655. DOI: 10.1142/S0217979210064265 (cit. on p. 97).

[96] X. Li et al. "Influence of electron-electron scattering on transport characteristics in monolayer graphene". In: *Appl. Phys. Lett.* 97 (2010), p. 082101. DOI: 10.1063/1.3483612 (cit. on p. 97).

[97] C. S. Lent and D. J. Kirkner. "The quantum transmitting boundary method". In: *J. Appl. Phys.* 67 (1990), p. 6353. DOI: 10.1063/1.345156 (cit. on p. 97).

[98] J. Munárriz. *Modelling of plasmonic and graphene nanodevices*. Berlin: Springer, 2014 (cit. on p. 97).

[99] S. Datta. *Electronic transport in mesoscopic systems*. Cambridge: Cambridge University Press, 1995 (cit. on p. 97).

[100] V. Clericò et al. "Quantized Electron Transport Through Graphene Nanoconstrictions". In: *Phys. Status Solidi A* 215 (2018), p. 1701065. DOI: 10.1002/pssa.201701065 (cit. on pp. 98, 103, 108).

[101] J. M. Caridad et al. "Conductance quantization suppression in the quantum Hall regime". In: *Nat. Commun.* 9 (2018), p. 659. DOI: 10.1038/s41467-018-03064-8 (cit. on pp. 98, 103, 106, 108).

[102] M. Han et al. "Electronic transport measurements in graphene nanoribbons". In: *phys. stat. sol. (b)* 244 (2007), p. 4134. DOI: 10.1002/pssb.200776197 (cit. on p. 99).

[103] B. Özyilmaz et al. "Electronic transport in locally gated graphene nanoconstrictions". In: *Appl.Phys.Lett.* 91 (2007), p. 192107. DOI: 10.1063/1.2803074 (cit. on p. 99).

[104] S. Hansel, M. Lafkioti, and V. Krstiç. "Suppression of short-range scattering via hydrophobic substrates and the fractional quantum Hall effect in graphene". In: *Phys. Status Solidi* 6 (2012), p. 376. DOI: 10.1002/pssr.201206297 (cit. on p. 100).

[105] S. Ihnatsenka and G. Kirczenow. "Conductance quantization in graphene nanoconstrictions with mesoscopically smooth butatomically stepped boundaries". In: *Phys. Rev.B* 85 (2012), p. 121407. DOI: 10.1103/PhysRevB.85.121407 (cit. on pp. 103, 110).

[106] S. Somanchi et al. "From diffusive to ballistic transport in etched graphene constrictions and nanoribbons". In: *Ann. Phys. (Berlin)* 529 (2017), p. 1700082. DOI: 10.1002/andp.201700082 (cit. on p. 103).

[107] T. Defforgea et al. "Scalloping removal on DRIE via using low concentrated alkaline solutions at low temperature". In: *Sens. Actuators A Phys.* 170 (2011), p. 114. DOI: 10.1016/j.sna.2011.05.028 (cit. on p. 104).

[108] V. J. Cadarso et al. "High-aspect-ratio nanoimprint process chains". In: *Microsyst. Nanoeng.* 3 (2017), p. 17017. DOI: 10.1038/micronano.2017.17 (cit. on p. 104).

[109] Z. Liu et al. “Super-selective cryogenic etching for sub-10 nm features”. In: *Nanotechnology* 24 (2013), p. 015305. DOI: 10.1088/0957-4484/24/1/015305 (cit. on p. 104).

[110] M. H. D. Guimarães et al. “From quantum confinement to quantum Hall effect in graphene nanostructures”. In: *Phys. Rev. B* 85 (2012), p. 075424. DOI: 10.1103/PhysRevB.85.07542 (cit. on pp. 110, 138).

[111] V. Clericò et al. “Quantum nanoconstrictions fabricated by cryo-etching in encapsulated graphene”. In: *Sci. Rep.* 9 (2019), p. 13572. DOI: 10.1038/s41598-019-50098-z (cit. on pp. 113, 138).

[112] C. L. Kane and E. J. Mele. “Quantum Spin Hall Effect in Graphene”. In: *Phys. Rev. Lett.* 95 (2005), p. 226081. DOI: 10.1103/PhysRevLett.95.226801 (cit. on p. 115).

[113] S. Pezzini et al. “Critical point for the canted antiferromagnetic to ferromagnetic phase transition at charge neutrality in bilayer graphene”. In: *Phys. Rev. B* 90 (2014), 121404(R). DOI: 10.1103/PhysRevB.90.121404 (cit. on p. 115).

[114] M. Z. Hasan and C. L. Kane. “Colloquium: Topological insulators”. In: *Rev. Mod. Phys.* 82 (2010), p. 3045. DOI: 10.1103/RevModPhys.82.3045 (cit. on pp. 115, 130).

[115] X.-L. Qi and S.-C. Zhang. “Topological insulators and superconductors”. In: *Rev. Mod. Phys.* 83 (2011), p. 1057. DOI: 10.1103/RevModPhys.83.1057 (cit. on p. 115).

[116] H. Sakaki et al. “$In_{1-x}Ga_xAs$-$GaSb_{1y}As_y$ heterojunctions by molecular beam epitaxy”. In: *Appl. Phys. Lett.* 31 (1977), p. 211. DOI: 10.1063/1.89609 (cit. on p. 116).

[117] S. K. Lyo and W. Pan. "Excitons in coupled type-II double quantum wells under electric and magnetic fields: InAs/AlSb/GaSb." In: *J. Appl. Phys.* 118 (2015), p. 195705. DOI: 10.1063/1.4935546 (cit. on p. 116).

[118] K. Suzuki et al. "Edge channel transport in the InAs/GaSb topological insulating phase." In: *Phys. Rev. B* 87 (2013), p. 235311. DOI: 10.1103/PhysRevB.87.235311 (cit. on pp. 116, 120, 124, 132).

[119] C. Liu et al. "Quantum spin hall effect in inverted type-II semiconductors." In: *Phys. Rev. Lett.* 100 (2008), p. 236301. DOI: 10.1103/PhysRevLett.100.236601 (cit. on p. 116).

[120] M. Karalic et al. "Experimental signatures of the inverted phase in InAs/GaSb coupled quantum wells". In: *Phys. Rev. B* 94 (2016), 241402(R). DOI: 10.1103/PhysRevB.94.241402 (cit. on pp. 116, 130, 131, 133).

[121] F. Nichele et al. "Giant Spin-Orbit Splitting in Inverted InAs/GaSb Double Quantum Wells". In: *Phys. Rev. Lett.* 118 (2017), p. 016801. DOI: 10.1103/PhysRevLett.118.016801 (cit. on pp. 116, 130).

[122] F. Nichele et al. "Edge transport of trivial phase os InAs/GaSb". In: *New J. Phys.* 18 (2016), p. 083005. DOI: 10.1088/1367-2630/18/8/083005 (cit. on pp. 116, 132).

[123] N. F. Mott. "The transition to the metallic state". In: *Phil. Mag* 6 (1961), p. 287. DOI: 10.1080/14786436108243318 (cit. on pp. 116, 133).

[124] R.S. Knox. "Theory of Excitons". In: *Phil. Mag* (1963) (cit. on p. 116).

[125] D. Jérome, T. M. Rice, and W. Kohn. "Excitonic insulator". In: *Phis. Rev.* 158 (1967), p. 462. DOI: 10.1103/PhysRev.158.462 (cit. on p. 117).

[126] J. Zittartz. "Anisotropy Effects in the Excitonic Insulator". In: *Phys. Rev.* 162 (1967), p. 752. DOI: 10.1103/PhysRev.162.752 (cit. on p. 117).

[127] W.Kohn. "Excitonic Phases". In: *Phys. Rev. Lett.* 19 (1967), p. 439. DOI: 10.1103/PhysRevLett.19.439 (cit. on p. 117).

[128] Y.E. Lozovik and V.I. Yudson. “Feasibility of superfluidity of paired spatially separated electrons and holes; a new superconductivity mechanism”. In: *Jept. Lett.* 22 (1975), p. 274 (cit. on p. 117).

[129] B. Bucher, P. Steiner, and P. Wachter. “Excitonic insulator phase in TmSe0.45Te0.55”. In: *Phys Rev Lett.* 67 (1991), p. 2717. DOI: 10.1103/PhysRevLett.67.2717 (cit. on p. 117).

[130] X. Zhu et al. “Exciton Condensate in Semiconductor Quantum Well Structures”. In: *Phys. Rev. Lett.* 74 (1995), p. 1633. DOI: 10.1103/PhysRevLett.74.1633 (cit. on p. 117).

[131] D. S. Chemla L. V. Butov A. C. Gossard. “Macroscopically ordered state in an exciton system”. In: *Nature* 418 (2002), p. 751. DOI: 10.1038/nature00943 (cit. on p. 117).

[132] D. W. Snoke. “Spontaneous Bose Coherence of Excitons and Polaritons”. In: *Science* 298 (2002), p. 1368. DOI: 10.1126/science.1078082 (cit. on p. 117).

[133] J. P. Eisenstein and A.H. MacDonald. “Bose–Einstein condensation of excitons in bilayer electron systems”. In: *Nature* 432 (2004), p. 691. DOI: 10.1038/nature03081 (cit. on p. 117).

[134] M. Rontani and L. J. Sham. “Coherent Transport in a Homojunction between an Excitonic Insulator and Semimetal”. In: *Phys. Rev. Lett* 94 (2005), p. 186404. DOI: 10.1103/PhysRevLett.94.1864043 (cit. on p. 117).

[135] H. Cercellier et al. “Evidence for an Excitonic Insulator Phase in 1T$TiSe_2$”. In: *Phys. Rev. Lett* 99 (2007), p. 145403. DOI: 10.1103/PhysRevLett.99.146403 (cit. on p. 117).

[136] B. Laikhtman Y. Naveh. “Excitonic Instability and Electric-Field-Induced Phase Transition Towards a Two-Dimensional Exciton Condensate”.

In: *Phys. Rev. Lett* 77 (1996), p. 900. DOI: 10.1103/PhysRevLett.77.900 (cit. on pp. 117, 134).

[137] B.D. Kono et al. “Cyclotron-resonance oscillations in a two-dimensional electron-hole system”. In: *Phys. Rev. B* 50 (1994), 12242(R). DOI: 10.1103/PhysRevB.50.12242 (cit. on p. 117).

[138] T. P. Marlow et al. “Ground State of a Two-Dimensional Coupled Electron-Hole Gas in InAs/GaSb Narrow Gap Heterostructures”. In: *Phys. Rev. Lett.* 82 (1999), p. 2362. DOI: 10.1103/PhysRevLett.82.2362 (cit. on p. 117).

[139] L.-C. Tung et al. “Magneto-infrared modes in InAs-AlSb-GaSb coupled quantum wells”. In: *Phys. Rev. B* 82 (2010), p. 115305. DOI: 10.1103/PhysRevB.82.115305 (cit. on p. 117).

[140] D. I. Pikulin and T. Hyart. “Interplay of Exciton Condensation and the Quantum Spin Hall Effect in InAs/GaSb Bilayers”. In: *Phys. Rev. Lett.* 112 (2014), p. 176403. DOI: 10.1103/PhysRevLett.112.1764035 (cit. on p. 117).

[141] J. Li, W. Yang, and K. Chang. “Spin states in InAs/AlSb/GaSb semiconductor quantum wells”. In: *Phys. Rev. B* 80 (2009), p. 035303. DOI: 10.1103/PhysRevB.80.035303 (cit. on pp. 117, 119).

[142] M.G. Burt. “The justification for applying the effective-mass approximation to microstructures.” In: *Journal of Physics: Condensed Matter* 4 (1992), p. 6651. DOI: 10.1088/0953-8984/4/32/003 (cit. on pp. 118, 119).

[143] E. G. Novik et al. “Band structure of semimagnetic Hg1-yMnyTe quantum wells.” In: *Phys. Rev. B* 72 (2005), p. 035321. DOI: 10.1103/PhysRevB.72.035321 (cit. on pp. 118, 119).

[144] I. Vurgaftman, J.R. Meyer, and L.R. Ram-Mohan. “Band parameters for III–V compound semiconductors and their alloys”. In: *J. Appl. Phys.* 89 (2001), p. 5812. DOI: 10.1063/1.1368156 (cit. on p. 119).

[145] Y. Jiang et al. “Probing the semiconductor to semimetal transition in InAs/GaSb double quantum wells by magneto-infrared spectroscopy.” In: *Phys. Rev. B* 95 (2017), p. 045116. DOI: 10.1103/PhysRevB.95.045116 (cit. on p. 120).

[146] F. Amet et al. “Insulating Behavior at the Neutrality Point in Single-Layer Graphene”. In: *Phys. Rev. Lett.* 110 (2013), p. 216601. DOI: 10.1103/PhysRevLett.110.216601 (cit. on p. 124).

[147] W. Pan et al. “Chaotic quantum transport near the charge neutrality point in inverted type-II InAs/GaSb field-effect transistors”. In: *Appl. Phys. Lett.* 102 (2013), p. 033504. DOI: 10.1063/1.4789555 (cit. on p. 124).

[148] L. J. Cooper et al. “Resistance resonance induced by electron–hole hybridization in a strongly coupled InAs/GaSb/AlSb heterostructure”. In: *Phys. Rev. B* 57 (1998), p. 11915. DOI: 10.1103/PhysRevB.57.11915 (cit. on p. 124).

[149] R. R. Du Ivan Knez and Gerard Sullivan. “Finite conductivity in mesoscopic Hall bars of inverted InAs/GaSb quantum wells”. In: *Phys. Rev. B* 81 (2010), 201301(R). DOI: 10.1103/PhysRevB.81.201301 (cit. on p. 124).

[150] K. Suzuki et al. “Gate-controlled semimetal-topological insulator transitionin an InAs/GaSb heterostructure”. In: *Phys. Rev. B* 91 (2015), p. 245309. DOI: 10.1103/PhysRevB.91.245309 (cit. on p. 124).

[151] M. J. Yang et al. “Evidence of a Hybridization Gap in Semimetallic InAs/GaSb Systems”. In: *Phys. Rev. Lett.* 78 (1997), p. 4613. DOI: 10.1103/PhysRevLett.78.4613 (cit. on p. 126).

[152] B. Büttner et al. "Single valley Dirac fermions in zero-gap HgTe quantum wells". In: *Nat. Phys.* 7 (2011), p. 418. DOI: 10.1038/nphys1914 (cit. on pp. 126, 128, 134).

[153] F. Nichele et al. "Insulating state and giant nonlocal response in an InAs/GaSb quantum well in the quantum Hall regime". In: *Phys. Rev. Lett.* 112 (2014), p. 036802. DOI: 10.1103/PhysRevLett.112.036802 (cit. on pp. 128, 130).

[154] F. Qu et al. "Electric and Magnetic Tuning Between the Trivial and Topological Phases in InAs/GaSb Double Quantum Wells". In: *Phys. Rev. Lett.* 115 (2015), p. 036803. DOI: 10.1103/PhysRevLett.115.036803 (cit. on pp. 130, 135).

[155] A. Roth et al. "Nonlocal Transport in the Quantum Spin Hall State". In: *Science* 325 (2009), p. 294. DOI: 10.1126/science.1174736 (cit. on p. 132).

[156] X. Zhu, J. J. Quinn, and G. Gumbs. "Excitonic insulator transition in a GaSb-AlSb-InAs quantum-well structure". In: *Solid State Commun.* 75 (1990), p. 595. DOI: 10.1016/0038-1098(90)90425-B (cit. on p. 134).

[157] L.-H. Hu et al. "Topological charge-density and spin-density waves in InAs/GaSb quantum wells under an in-plane magnetic field". In: *Phys. Rev. B* 96 (2017), p. 075130. DOI: 10.1103/PhysRevB.96.075130 (cit. on p. 134).

[158] M. Knap et al. "Transport in Two-Dimensional Disordered Semimetals". In: *Phys. Rev. Lett.* 113 (2014), p. 186801. DOI: 10.1103/PhysRevLett.113.186801 (cit. on p. 134).

[159] E. B. Olshanetskya et al. "Metal-insulator transition in a HgTe quantum well under hydrostatic pressure". In: *JETP Lett.* 98 (2013), p. 843. DOI: 10.1134/S0021364013250176 (cit. on p. 134).

[160] B. Shojaei et al. “Materials considerations for forming the topological insulator phase in InAs/GaSb heterostructures”. In: *Phys. Rev. Materials 2* 2 (2018), p. 064603. DOI: 10.1103/PhysRevMaterials.2.064603 (cit. on p. 135).

[161] W.S. Hwanga and K. Tahy. “Fabrication of top-gated epitaxial graphene nanoribbon FETs usinghydrogen-silsesquioxane”. In: *Journal of Vacuum Science Technology B* 30 (2012), p. 03D104. DOI: 10.1116/1.3693593 (cit. on p. 137).

[162] V. Ryzhii et al. “Vertical electron transport in van der Waals heterostructures with graphene layers”. In: *Journal of Applied Physics* 117 (2015), p. 154504. DOI: 10.1063/1.4918313 (cit. on p. 138).

[163] H. Yoo et al. “Atomic and electronic reconstruction at the van der Waals interface in twisted bilayer graphene”. In: *Nat. Mater.* 18 (2019), p. 448. DOI: 10.1038/s41563-019-0346-z (cit. on p. 138).

[164] K.Ren et al. “Electronic and optical properties of van der Waals vertical heterostructures based on two-dimensional transition metal dichalcogenides: First-principles calculations”. In: *Physics Letters A* 383 (2019), p. 1487. DOI: 10.1016/j.physleta.2019.01.060 (cit. on p. 138).

[165] J. G. Checkelsky, L. Li, and N. P. Ong. “The zero-energy state in graphene in a high magnetic field”. In: *Phys. Rev. Lett.* 100 (2008), p. 206801. DOI: 10.1103/PhysRevLett.100.206801 (cit. on p. 138).

[166] I.A. Gayduchenko et al. “Manifestation of plasmonic response in the detection of sub-terahertz radiation by graphene-based devices”. In: *Nanotechnology* 29 (2018), p. 245204. DOI: 10.1088/1361-6528/aab7a5 (cit. on p. 138).

[167] Z.-F. Liu et al. “Helical edge states and edge-state transport in strained armchair graphene nanoribbons”. In: *Sci. Rep.* 7 (2017), p. 8854. DOI: 10.1038/s41598-017-08954-3 (cit. on p. 139).

[168] T. Kariyado et al. "Counterpropagating topological interface states in graphene patchwork structures with regular arrays of nanoholes". In: *Phys. Rev. B* 98 (2018), p. 195416. DOI: 10.1103/PhysRevB.98.195416 (cit. on p. 139).

[169] K. Hatsuda et al. "Evidence for a quantum spin Hall phase in graphene decorated with Bi2Te3 nanoparticles". In: *Sci. Adv.* 4 (2018), eaau6915. DOI: 10.1126/sciadv.aau6915 (cit. on p. 139).

[170] M. Slota et al. "Magnetic edge states and coherent manipulation of graphene nanoribbons". In: *Nature* 557 (2018), p. 691. DOI: 10.1038/s41586-018-0297-6. (cit. on p. 139).

List of Figures

2.1 (a) Clean room drawing. In pink the Clean room area, the green line delimits the technical area (grey area). 6

2.2 (a) Photo of the "Evaporation"room without equipment in September 2014 (b) Photo of the "Lithography"room in the same period. 8

2.3 Clean room Facilities : (a) "lithography room"(b) "evaporation room" 8

2.4 (a) Photo of the FE-SEM and the Raith nanolithography system. (b) Schematic views of FE-SEM, (c) electron beam path. (d) field emission gun, (e) position of InLens and SE detector respect the specimen and the column. All the schematic views are taken from the SmartSEM 5.6 software. 11

2.5 (a) Schematic representation of an electron beam lithography process (b) The same CAD designed with ELPHY software in which we selected two different writing field (WF): 1000 μm (left) and 500 μm (right). 15

2.6 (a) Typical plasma etching process. (b) Etching of silicon with fluorine and chlorine gases (c)(images from Oxford Instrument). (d) working principle of RIE process. (e) Working principle of ICP-RIE process. 17

2.7 (a) ICP-RIE load lock and PC controller inside the clean room. (b) Rest of the equipment installation in the technical room. . . 19

2.8 (a) Working principle of optical lithography. (b) Optical mask lithography. (c) Front and (d) side views of the MJB4 mask aligner. 21
2.9 (a) E-beam evaporator designed by Tecnovac, with Telemark e-beam gun. (b) E-beam source model 244. (c) Crucible pocket and (d) detailed Cr-crucible. (e) Photo during an evaporation (view from an external window thanks to an internal periscope). 23
2.10 (a) RTP As-One100. (b) Internal chamber with the lamp furnace. 25
2.11 (a)Leica DM8000 Optical Microscope and DektakXT Bruker Profilometer (b) Harrick Plasma cleaner. 26
2.12 Transfer setup: Optical microscope, X-Y-Z- micrometer and tilt stages, Camera (and screen), Heating plate and current power supply, PDMS stamp. 29
2.13 (a) Rayleigh, Stokes and Anti-Stokes processes. (b) LabRam HR Evolution MicroRaman. (c) Front view of the equipment. . 31
2.14 (a) 4-probes Cascade Summit 1100B Station. (b) TPT BH10 Wire Bonder. 33
2.15 Optistat AC-V12 (3K) cryostat. 36
2.16 Triton system (left) and superconducting magnet (right). . . . 37
2.17 (a) HFML Facilities. (b) Magnet. (c) Setup for Measurements. (d) Homemade column with sample holder. 38
2.18 Photo of TDS setup. In the inset the schematic setup. 39
2.19 (a) Schematic view of a typical setup for the transport measurements with the lock in technique. (b) Lock-in amplifier SR830 (up) and Keithley sourcemeter 2612A (down). (c) 20-LCC pin holder in which we bounded one of our graphene Hall Bar. In the inset the Optical image of the same Hall bar of encapsulated graphene. 42

3.1 (a) Optical image of mono-bi-tri layer graphene flake. (b) Optical image of graphite with different thickness. (c) Normalized Raman spectra of two flakes of graphene. The black line shows the Raman spectra of a monolayer graphene on Si/SiO_2 substrate and the red line corresponds to a monolayer graphene on Si/SiO_2 substrate with HMDS treatment. (d) Optical image of mono-layer graphene on SiO_2 with Hall Bar configuration. 50

3.2 (a) Left: Profilometer measurement of h-BN flakes with different thickness (Optical Image with the scanning line in the inset). Right: Optical image of a flake of hBN that was etched with ICP-RIE in various steps. The contrast (colour) of the flake changes with the thickness (b) Preparation of the Polycarbonate film. (c) Preparation of PC film on a Magic tape windows and PDMS stamp. (d) Three different possible situations of the contact area during the transfer process. (e) Typical Hall bar of graphene on hBN. In the inset the Hall bar definition of graphene on h-BN before the deposition of the ohmic contacts. 52

3.3 (a) Transfer step processes for graphite/hBN heterostructure. (b) Optical images of bottom hBN (top left) graphite (bottom left) and their correspondent heterostructure. 59

3.4 (a) Transfer step processes for hBN/graphene heterostructure. (b) Optical images of top hBN (top left) graphene (bottom left) and their correspondent heterostructure. 60

3.5 (a) Transfer last steps for graphite/h-BN/graphene/hBN heterostructure. (b) Optical images of graphene/top hBN (top left) graphite/bottom hBN (bottom left) and the whole heterostructure (right). 61

3.6 (a) Raman spectra of the hBN/graphene/hBN heterostructure (b) Raman spectra of the graphite/hBN/graphene/hBN heterostructure (c) MicroRaman Map of the whole heterostructure graphite/hBN/graphene/hBN heterostructure. 62

3.7 (a) From the top to the bottom: definition of the Hall Bar through EBL, etching of the Hall Bar through ICP-RIE process, definition of the contacts (and contact for the graphite bottom gate) with a second EBL. (b) Final devices after evaporation of Cr/Au and lift-off process. 63

3.8 (a) SEM image of a NC etched by our cryo-etching process. Three bubbles appear in the image, they are blister of air trapped into the original heterostructures and in this case they are transferred to the substrate after the etching process (so they do not affect the device). (b) SEM image of a NC on hBN etched with a standard ICP-RIE procedure. The upper panel of each column shows the original SEM images in grey scale and the lower panels display the coloured ones. (c) Tilted SEM image of typical devices with NCs in encapsulated graphene 65

3.9 Fabrication process of FETs in encapsulated graphene can be divided in three different steps; Bar definition, fabrication of the external contacts and top gates. 67

3.10 Fabrication process of Hall Bar on epitaxial graphene. (a) Optical image of the Bar definition and removal of graphene under pads and contacts. (b) Optical image contacts definition. (c) SEM image of the device after contacts and Pads deposition. . 68

3.11 (a) Optical image of the Hall Bar on epitaxial graphene. (b) Transfer of a hBN flake on the epitaxial Hall Bar. (c) Optical image of the final device, top-gated Hall Bar with hBN as dielectric film. (d) Longitudinal resistance (black line) and quasi longitudinal resistance (red line) in function of top gate voltage (V_g) at room temperature. (e) Transversal resistance versus magnetic field (B) at room temperature 71

3.12 (a) Optical image of the Pad after developing. (b) Optical image of the Pad after evaporation and lift off. (c) All the Pads on CVD graphene transferred on quartz. (d) Comparison between the Raman spectra of exfoliated graphene (green line) and CVD graphene (blue line). 73

3.13 (a) Profilometer of the blue colour flake. It had a thickness around 5 nm. Inset: Optical image a flake of $MoSe_2$. (b) Raman spectra of the flake (c) Transfer of the flake on a prepatterned device (d) Another device with a $MoSe_2$ flake of 4 nm (e) Drain current as a function of gate voltage with fixed drain voltage (2V) (f) Photoluminescence PL measurement of the monolayer flake with MicroRaman. Inset: Optical image of monolayer $MoSe_2$ device. 75

3.14 (a) Optical image a flake of $MoTe_2$ (inset of Figure 3.14a) transferred on prepatterned contacts (Figure 3.14a). (b) Raman spectra of a 5L-$MoTe_2$ (c) device with a 5L-$MoTe_2$ flake (f) Drain current as a function of gate voltage with fixed drain voltage (18V) of 5L-$MoTe_2$. 76

4.1 (a) Optical Image of encapsulated graphene Hall Bar. (b) Longitudinal resistivity versus normalized gate voltage for different temperatures. (c) Longitudinal Resistivity temperature dependence for different valued of gate voltage. (d) Longitudinal conductance temperature dependence for gate voltage values close the CNP. (e) Longitudinal conductance temperature dependence for gate voltage values far from the CNP. 81

4.2 (a) Resistance (R) versus carrier density n and fit with the field effect formula for hole (blue line) and electron side (red line). (c) Conductivity σ in function of carrier density n in double-logarithmic scale for the extraction of the value n*. 83

4.3 (a) Mobility (μ) versus the extrapolated value of n^* for different devices. (b) $\frac{1}{\mu}$ versus n^*. In the inset we consider only the higher mobility devices. (c) σ^*, estimated by the carrier density fluctuation, versus σ_{min}, both are in e^2/h unit. 85

4.4 (a) Longitudinal and transversal resistivity in h/e^2 unit versus normalized gate voltage at room temperature and 30T. In the inset the zoomed longitudinal resistance of the hole side (top-left) and electron side (bottom-right). Zoomed transversal resistance at different temperatures around the filling factor 2 for hole (b) and electron (c) side. 86

4.5 (a) Longitudinal resistance and transversal resistivity in h/e^2 unit versus normalized gate voltage at room temperature and 30T for low mobility ($1700 cm^2 V^{-1} s^{-1}$ at room temperature) graphene device (graphene on SiO_2). (b) Transversal resistance at different temperatures versus normalized gate voltage. Room temperature measurement is highlighted with a thicker black line. 87

4.6 Longitudinal resistance at different temperatures as function of the gate voltage around the filling factor 2 for hole (a) and electron side (b). (c) Estimation of the activation gap from the resistivity versus the inverse of the temperature for HBUN15 (holes). (d) Dependence of the activation gap for different magnetic fields in comparison with the theoretically expected energy gaps for sharp Landau levels. 89

4.7 (a) Derivative of the longitudinal (black line) and transversal conductivity (red line) respect the filling factor ν, measured at room temperature and 30T. (b) Width $\Delta\nu$ and $d\sigma_{xy}^{max}/d\nu$ estimated for the zero Landau level at high magnetic fields (20 T, 25 T and 30 T) and high range of temperatures. 91

4.8 (a) Longitudinal (multiplied by a factor of 10) and transverse conductance in function of normalized gate voltage at 25T and 1.4K. (b) Transverse conductance for different magnetic field values (15T, 17.5T, 20T, 22.5T, 25T) at 1.4K. 92

5.1 (a) SEM image of a bar of graphene (1μm*2μm) with HMDS treatment. (b) 2-probes resistance (R) versus carrier density carrier (n). In the insert the original resistance versus backgate voltage (V_{bg}) 99

5.2 (a) SEM image of a GNC with HMDS treatment ($W = 85nm$) with HMDS treatment. (b) Conductance (G) of the GNC in $2e^2/h$ unit versus normalized backgate voltage (V_{bg}). 101

5.3 (a) Conductance (G) as function of the Fermi wavenumber k_F with (black line) and without (red line) the effect of HMDS.b) Conductance (G) (black line) and transconductance ($\frac{dG}{dWk_F}$) (blue line) of the GNC in e^2/h unit versus Wk_F. 102

5.4 (a) Tilted SEM micrograph of an encapsulated graphene NC with lateral width $W \simeq 206\,\text{nm}$ and length $L \simeq 200\,\text{nm}$ including an schematic view of the electronic setup. The inset shows an enlarged view where the hBN/graphene/hBN heterostructure is colored in sky blue, the SiO_2 substrate (partially etched) in violet and the contacts in yellow gold. (b) Conductance as a function of the normalized voltage $\Delta V_g = V_g - V_g^*$ for the same NC measured at $T = 3.1\,\text{K}$. 105

5.5 (a) AFM image of the graphene NC with $W = 206\,\text{nm}$. (b) Contour plot taken from the square highlighted in panel (a), at 15 nm from the top of the nanostructure. (c) Enlarged view of the contour plot, where the dashed lines indicate the values used to estimate the edge roughness. 106

5.6 (a) Conductance in units of e^2/h versus the Fermi wavenumber k_F for forward and backward currents at the hole side, showing well-defined plateaus of the conductance. The transmission parameter t is obtained from the linear fitting of the conductance (in units of e^2/h) as a function of Wk_F for the (b) hole side ($t = 0.865$) and (c) electron side ($t = 0.863$). The width of the constriction is $W = 206\,\text{nm}$. 107

5.7 (a) Comparison of simulated and experimental conductance of a GNC of width $W = 206$ nm. (b) Conductance (red line) and transconductance (blue line) as a function Wk_F measured at $T = 3.1$ K. Solid black arrows show the position of the plateaus of conductance separated by $2e^2/h$ and matching integer values from $G = 10e^2/h$ onwards. (c) Evolution of G as a function of Wk_F at different temperatures. The curves have been horizontally shifted by a factor $2.5Wk_F$ for clarity. (d) Temperature dependence of the transconductance as a function of Wk_F. Black solid arrows represent the value of the plateaus of conductance in units of e^2/h at $T = 3.1$ K, matching the position of the minima in $dG/d(Wk_F)$. 109

5.8 Sem images of : (a)(b) Nanoconstrictions in encapsulated graphene of $\approx$30 nm and $\approx$ 60 nm, (c)(d) Nanoribbon and nanocostriction of $\approx$ of 85 nm in graphene on SiO_2 with HMDS treatment. 112

6.1 (a) Schematic structure of the InAs/GaSb DQW samples. (b) Evolution of the electron and hole subbands as a function of the InAs thickness d, calculated using the 8-band $\mathbf{k} \cdot \mathbf{p}$ method. The critical thickness d_c, corresponding to the boundary between the normal and inverted band structures, is found to be $d_c = 10.03nm$. 118

6.2 (a) Band structures of the InAs/GaSb DQWs calculated using the 8-band $\mathbf{k} \cdot \mathbf{p}$ method (see previous section) for three typical configurations: (left, sample A) d = 9 nm, (middle, sample B) d = 10 nm, and (right, sample C) d =13 nm. (b) shows schematic band profiles for samples A-C, respectively. E_0 is the lowest electron subband in the conduction band and H_0 the highest hole subband in the valence band. E_F is the Fermi level, at the charge neutrality point. The shaded inset in the middle panel shows the opening of the energy gap (Δ) due to the formation of an excitonic insulator phase. (c) displays 4-terminal resistance as function of gate voltage, measured at T = 500 mK, in samples A-C, respectively. The gate voltage is normalized so that the gate voltage at the CNP is zero ($V_g^* = V_g - V_g^{CNP}$). Hall Bar configuration of the measured samples in the inset of the bottom figure, in which $W = L_1 = 250\mu$m, $L_2 = 500\mu$m . 121

6.3 (a) Longitudinal resistance R_{xx} as a function of gate voltage Vg for different temperatures (40mK-20K) at $B = 0T$, measured in sample B. (b) maximum of R_{xx} in the CNR as a function of $1/T$. The red line is a fit to $R_{xx}^{CNP} \sim e^{\frac{\Delta}{2k_BT}}$, obtained for the data at $T > 7K$, which provides the estimation of the energy gap Δ reported in the text. The inset shows the temperature dependent data of R_{xx}^{CNP} at various magnetic fields. 123

6.4 (Temperature dependence (a) and Arrhenius fit (b) for sample A. The data for sample C are shown in (c) and (d), respectively. 125

6.5 Longitudinal resistance versus gate voltages at 0.3K from 0 to 3 T perpendicular magnetic field for the normal insulator sample InAs(9nm)/GaSb(5nm) (a), the critical sample 10/5 nm (b) and an inverted sample 13/5 (c). Notice the decrease of the CNP resistance at low magnetic fields up to 2 T for the critical sample whereas in the other two there is always a systematic increase. 126

6.6 Longitudinal resistance in parallel magnetic field. Normalized magnetoresistance $\frac{(R_{xx}(B\|)-R_{xx}(0))}{Rxx(0)}$ versus gate voltages in the presence of different parallel magnetic fields for the NI sample (a), critical (b), and two inverted samples (c) and (d). While the NI sample InAs(9 nm)/GaSb(5 nm) and critical sample (10/5 nm) shows almost no parallel magnetic field dependence in the CNP, samples (11/5) nm and (13/5 nm) show a strong field dependence, characteristic of inverted band configurations. . . 127

6.7 Hall conductivity (σ_{xy}) at 300 mK at different perpendicular magnetic fields. The blue and red lines, defined by the boundaries of the plateau in the CNR in sample cross at $B_c < 0T$ revealing a normal insulator regime for sample (9/5 nm) (a); in sample (10/5 nm) cross at $B_c \approx 0T$ revealing a zero gap sample (b); finally in sample (13/5 nm) cross at $B_c > 0T$, indicating an inverted regime. 128

6.8 (a) Longitudinal (σ_{xx}) and Hall (σ_{xy}) conductivities as a function of Vg, measured at B = 7 T. (b) Two-dimensional charge density for electrons n and holes p as a function of Vg. (c) Normalized magnetoresistance ($R_{xx}(B)$) 129

6.9 (a) Logarithmic longitudinal resistance ($\log(\rho_{xx})$) versus the gate voltage. (b) Temperature dependence of the logarithmic longitudinal resistance. (c) Local (black line) and no local (red line) measurements (on the right the schematic configuration). 131

6.10 (a)(b) Trasversal resistance as function of the magnetic field for different value of the gate voltage in the electron (a) and hole (b) region. (c) Trasversal conductance versus gate voltage at different value of magnetic field (d) Colour map of the longitudinal resistivity as function of magnetic field and gate voltage. 132

List of Tables

2.1 ISO class conditions from class ISO 1 to class ISO 9 for maximum concentration limits (particles/m^3 of air) 7

6.1 Table with the summary of the band parameters 120